# PANDORA: Population Archive of Neuroimaging Data Organized for Rapid Analysis

Aslan Abivardi[1,2], Matthew Webster[1], Paul McCarthy[1], Fidel Alfaro-Almagro[1], Lav Radosavljevic[3], Karla L. Miller[1], Saad Jbabdi[1], Mark W. Woolrich[4], Weikang Gong[5], Christian F. Beckmann[6], Lloyd T. Elliott[7], Thomas E. Nichols[3,1], Stephen M. Smith[1]

1. FMRIB, OxCIN, NDCN, Oxford University, UK
2. Department of Psychiatry, Psychotherapy and Psychosomatics, University of Zurich, Switzerland
3. Big Data Institute, Oxford University, UK
4. OHBA, OxCIN, Psychiatry, Oxford University, UK
5. School of Data Science, Fudan University, China
6. Donders Institute for Brain, Cognition and Behaviour, Radboud University, Nijmegen, Netherlands
7. Department of Statistics and Actuarial Science, Simon Fraser University, Burnaby, Canada

## Abstract:

We present PANDORA (Population Archive of Neuroimaging Data Organized for Rapid Analysis), a huge brain imaging data archive and analysis resource for UK Biobank neuroimaging data. PANDORA UKBv1 contains 81,939 subjects' voxel-level images, created by the core UKB brain image processing pipeline. PANDORA also includes highly efficient supervoxel versions of the data – much smaller and faster to work with than the full voxelwise representation while losing virtually no signal or spatial detail and providing denoising. For each of 98 sub-modalities (outputs from processing functional, structural, and diffusion modalities, e.g., fractional anisotropy from dMRI), images are collated into one massive subjectsXvoxels matrix, stored as a single convenient HDF5 file**,** alongside the compact subjectsXsupervoxels representations (1K and 10K)**.** Also included are robust preprocessing, a curated set of imaging confounds, and a tool for easy voxelwise cross-subject regression against variables such as genetics or lifestyle factors. The regression tool performs model estimation in the encoded supervoxel space while computing mass-univariate statistics in full-resolution space via supervoxel-to-voxel mappings. PANDORA is easy and quick to use on the UK Biobank RAP (Research Analysis Platform). Downloading a local copy of a single sub-modality from the central data store takes a few minutes, and then running a regression across 80K subjects and around 1M voxels takes between a few seconds and an hour, depending on the modality, the number of subjects, and the size of the regression design matrix. Validation shows that 10K-supervoxels closely match full-resolution spatial maps, whereas 1K-supervoxels are extremely compute-efficient and boost power for less localized effects. Benchmarks indicate substantive speed and memory gains. Across five experiments (common substance use, cumulative trauma, anxiety vs. depression, early- vs. late-diagnosis autism polygenic scores, and an *EPHA3* SNP), results reproduce known patterns and reveal new associations.

## 1. Introduction

Collecting multimodal MRI for 100,000 participants, the UK Biobank (UKB) brain initiative has transformed the field of population neuroimaging and challenged it to adapt to data on a massive scale (Miller et al., 2016). With increasing statistical power and dataset size, however, come major computational and storage challenges. Furthermore, noisy phenotypes and behaviors have proven to be less reliably detectable from brain images and more data-hungry than hoped (Schulz et al., 2020), warranting optimal data processing and analysis pipelines.

The Population Archive of Neuroimaging Data Organized for Rapid Analysis (PANDORA), a new resource designed to allow efficient computational analysis at the voxel level, provides a framework to confront these issues, with access to pre-processed imaging data for 98 sub-modalities in fast HDF5 data format, and critically providing new compressed supervoxels (via a linear embedding using very high-dimensional independent component analysis), accompanied by a novel method for voxelwise general linear model estimation directly in the encoded subspace.

Previously, to carry out voxel-level image analysis with UKB data, users had to access one ZIP file per modality per subject (e.g., at least 80,000 ZIP files for just one modality), unpack each file to extract the image of relevance, and then combine these across all subjects before analysis could begin. By bringing all of these images together across subjects into a single HDF5 file for each sub-modality, and curating those carefully (e.g., normalizing and handling outliers), PANDORA removes a major initial barrier to analyzing voxel-level UKB brain imaging data. A PANDORA data file (voxel or supervoxel) can, for example, be fed directly into multi-subject regression against a genetic variable or into deep neural network training.

In this paper, we first describe the PANDORA UKBv1 resource, including advanced general and modality-specific pre-processing steps with variance-based masking, data standardization, multi-stage outlier removal, and subsequent data-adaptive compression into supervoxels. We then validate the supervoxel representations by quantifying information retention as full-resolution variance explained and comparing this with variance explained by multimodal image-derived phenotypes (IDPs), across all 98 sub-modalities. Building on this, we introduce a new supervoxel-based GLM framework, in which model estimation is performed in the encoded supervoxel space, while voxel- and grayordinate-level statistics are recovered via supervoxel-to-voxel mappings. The mathematical details are given in the Methods, and we summarize its implementation in an expanded *fsl_glm* software tool, benchmarking its statistical power, runtime and memory use against a conventional full-resolution mass-univariate GLM.

Finally, we conduct five multimodal imaging experiments designed to showcase the utility of PANDORA across distinct scientific settings: (1) cumulative lifetime trauma, as an environmental exposure with widespread multimodal effects; (2) dissociable effects of anxiety and depressive symptom dimensions, probing sensitivity to overlapping but distinct affective phenotypes; (3) common substance use (smoking, alcohol and coffee), illustrating large-scale mapping of prevalent neuromodulatory exposures across modalities; (4) a single-nucleotide polymorphism (SNP) in the *EPHA3* gene, providing a case study of high-resolution voxelwise characterization of a specific developmental axon-guidance-related variant; and (5) separate polygenic scores for early- versus late-diagnosis autism, derived from age-of-diagnosis-stratified GWAS with distinct developmental and psychiatric correlation profiles, testing whether these partly divergent genetic architectures have dissociable whole-brain signatures in UKB.

Taken together, these advances position PANDORA as a next-generation resource for fast, voxelwise discovery across environmental, symptomatic and genetic dimensions of brain variation.

## 2. Materials and Methods

### 2.1 Dataset

PANDORA UKBv1 encompasses data for N=81,939 UKB subjects (53.2% female; mean age ± SD at study baseline: 55.0 ± 7.5 y, range: 40.1 – 70.4 y; mean age ± SD at first imaging session: 66.6 ± 7.9 y, range: 44.6 – 87.1 y), with 98 "sub-modalities" (distinct analysis output types) derived from 6 imaging modalities across structural, diffusion and functional MRI (Table 1). Functional MRI images use the HCP CIFTI representation (Glasser et al., 2016) as grayordinates (cortical surface vertices and subcortical voxels), and all other modalities use voxel representation, in MNI152 standard space.

For each sub-modality, full-resolution data are collated into a large subject x voxels/grayordinates 2D matrix, with the voxels/grayordinates from a single subject unwrapped into a single row in the matrix. Additionally, for every modality we provide two compressed versions, i.e., subject x supervoxel matrices for 1K- and 10K-supervoxels. The supervoxel matrices come each with supervoxel to voxel (/grayordinates) mappings.

To ensure high compatibility (Python, MATLAB, C/C++) and fast disk-access for analyses, all data files use the Hierarchical Data Format (HDF5) format (Folk et al., 2011), which among other things allows for contiguous disk space allocation. Furthermore, full-resolution matrices and supervoxel-to-voxel mappings are oriented such that the larger voxel dimension lies along the faster-varying (stride-1) dimension, which makes streaming them during analysis a viable option.

As our data processing pipeline already removes most redundant datapoints (e.g., voxels outside of the brain), standard file compression of the full-resolution data matrix did not add a large benefit in storage reduction (<15%), and we thus opted to prioritize simplicity and data access speed, and not add file compression (while achieving disk space reduction using the supervoxel approach).

| ***Sub-modality*** | **N available subjects** | **Modality** | **Full-resolution size (GB)** | **1K-supervoxels size (GB)** | **10K-supervoxels size (GB)** |
|---|---|---|---|---|---|
| *warpfield_jacobian* | 81,884 | T1 | 764.2 | 9.7 (A: 0.3; maps: 9.3) | 96.4 (A: 3.1; maps: 93.3) |
| *SWI_T2star* | 73,454 | SWI | 625.1 | 8.8 (A: 0.3; maps: 8.5) | 87.9 (A: 2.7; maps: 85.1) |
| *T1* | 81,871 | T1 | 597.7 | 7.6 (A: 0.3; maps: 7.3) | 76.1 (A: 3.1; maps: 73.0) |
| *T2_FLAIR* | 77,325 | T2_FLAIR | 564.5 | 7.6 (A: 0.3; maps: 7.3) | 75.9 (A: 2.9; maps: 73.0) |
| *SWI_QSM* | 73,288 | SWI | 525.1 | 7.5 (A: 0.3; maps: 7.2) | 74.4 (A: 2.7; maps: 71.7) |
| *T2_FLAIR_lesions* | 77,120 | T2_FLAIR | 238.1 | 3.4 (A: 0.3; maps: 3.1) | 33.8 (A: 2.9; maps: 30.9) |
| *DTI_MD* | 79,178 | dMRI | 177.3 | 2.5 (A: 0.3; maps: 2.2) | 25.3 (A: 3.0; maps: 22.4) |
| *DTI_L1* | 79,190 | dMRI | 177.3 | 2.5 (A: 0.3; maps: 2.2) | 25.3 (A: 3.0; maps: 22.4) |
| *DTI_L2* | 79,169 | dMRI | 177.3 | 2.5 (A: 0.3; maps: 2.2) | 25.3 (A: 3.0; maps: 22.4) |
| *DTI_L3* | 79,164 | dMRI | 177.3 | 2.5 (A: 0.3; maps: 2.2) | 25.3 (A: 3.0; maps: 22.4) |
| *NODDI_ICVF* | 79,168 | dMRI | 177.3 | 2.5 (A: 0.3; maps: 2.2) | 25.3 (A: 3.0; maps: 22.4) |
| *NODDI_OD* | 79,164 | dMRI | 177.3 | 2.5 (A: 0.3; maps: 2.2) | 25.3 (A: 3.0; maps: 22.4) |
| *NODDI_ISOVF* | 79,168 | dMRI | 177.2 | 2.5 (A: 0.3; maps: 2.2) | 25.3 (A: 3.0; maps: 22.4) |
| *DTI_MO* | 79,148 | dMRI | 177.1 | 2.5 (A: 0.3; maps: 2.2) | 25.3 (A: 3.0; maps: 22.4) |
| *DTI_FA* | 79,159 | dMRI | 174.8 | 2.5 (A: 0.3; maps: 2.2) | 25.0 (A: 3.0; maps: 22.1) |
| *dMRI_tracts* | 76,035 | dMRI | 140.8 | 2.1 (A: 0.3; maps: 1.9) | 21.4 (A: 2.8; maps: 18.5) |
| *T1_VBM* | 81,892 | T1 | 65.8 | 1.1 (A: 0.3; maps: 0.8) | 11.1 (A: 3.1; maps: 8.0) |
| *RSN_d50 (1-50)* | 76,762.4 ± 199.5 | rfMRI | 26.1 ± 0.2 | 0.6 ± 0.0 (A: 0.3; maps: 0.3) | 6.3 ± 0.0 (A: 2.9; maps: 3.4) |
| *RSN_d25 (1-25)* | 76,499.5 ± 548.9 | rfMRI | 26.0 ± 0.1 | 0.6 ± 0.0 (A: 0.3; maps: 0.3) | 6.3 ± 0.0 (A: 2.9; maps: 3.4) |
| *tfMRI_zstat1* | 63,674 | tfMRI | 21.7 | 0.6 (A: 0.2; maps: 0.3) | 5.8 (A: 2.4; maps: 3.4) |
| *tfMRI_zstat2* | 63,736 | tfMRI | 21.7 | 0.6 (A: 0.2; maps: 0.3) | 5.8 (A: 2.4; maps: 3.4) |
| *tfMRI_zstat5* | 63,810 | tfMRI | 21.7 | 0.6 (A: 0.2; maps: 0.3) | 5.8 (A: 2.4; maps: 3.4) |
| *tfMRI_cope1* | 63,602 | tfMRI | 21.6 | 0.6 (A: 0.2; maps: 0.3) | 5.8 (A: 2.4; maps: 3.4) |
| *tfMRI_cope5* | 63,539 | tfMRI | 21.6 | 0.6 (A: 0.2; maps: 0.3) | 5.8 (A: 2.4; maps: 3.4) |
| *tfMRI_cope2* | 63,355 | tfMRI | 21.5 | 0.6 (A: 0.2; maps: 0.3) | 5.8 (A: 2.4; maps: 3.4) |

***Table 1.*** *98 PANDORA sub-modalities with comparison of disk space utilization for full-resolution vs. supervoxel data. Supervoxels are divided in subject-specific loadings (A matrix) and spatial maps.*

## 2.2 Data processing

To create the full-resolution voxel-level datasets, pre-processed UKB NIfTI / CIFTI images as described in Alfaro-Almagro et al. (2018), were first loaded into a subject x voxel (/ grayordinates) matrix; 3D NIfTI images (in standard MNI space) were either masked using a mean fractional anisotropy image-derived white matter mask for dMRI-based maps or using a liberal T1-derived whole-brain mask. The much smaller surface-based CIFTI images were loaded in completely.

To remove low-variance voxels, we computed (across-subject) standard deviations for each voxel, and discarded those with values < 5% of the $90^{th}$ percentile (robust maximum) across voxels. This variance-derived mask, a subset of the loading mask, is available for every PANDORA modality.

Next, outlier participants (with respect to mean image intensity and/or number of outlier voxels) were fully removed from the matrix, after which individual outlier voxels were imputed in the remaining subjects using the column median value. This process is described in further detail below.

Finally, the columns of the remaining modality matrix are first demeaned, and then the whole matrix is divided by its global standard deviation. Crucially, we do not standardize individual columns, as this would remove signal variance differences that may be important. Both column- and row-mean are saved out as mean modality image and subject course in this step.

To ensure numerical stability of the randomized SVD for encoding (see below), image data required upcasting from single- to double-precision (i.e., float32 to float64; performed during loading). The final data matrices were saved as single-precision, however, to limit storage space.

Due to the large memory requirement of holding the entire full-resolution matrix in RAM as required for encoding, processing steps had to be ensured to work with in-place operations, exclusively necessitating careful selection of library functions (e.g., NumPy's median function copies its input, while nanmedian does not) and custom code for non-contiguous column/row removal.

All data processing was performed in python using the NumPy (Harris et al., 2020) and Scikit-learn (Pedregosa et al., 2011).

## 2.3 Modality-specific processing

T1, T2-FLAIR and voxel-based morphometry (VBM) maps required specific processing steps applied before loading images into the initial subject x voxel matrices.

Due to their non-quantitative nature, bias-field corrected T1 and T2-FLAIR images were normalized using the image median white matter image value. This normalization will not always be perfect, e.g., in cases where biological signal of interest may bleed into the normalization factor. For example, for T2-FLAIR images, the median may be shifted in subjects with very high lesion load. Future work will attempt to address this with more sophisticated normalization.

Standard processing was applied for VBM maps. Specifically, we applied a smoothing with a Gaussian kernel with sigma 2.1233 mm (≈ 5 mm full width at half maximum). Additionally, voxels with median gray matter probability < 5% were discarded after removal of low-variance voxels in the main pipeline (median probability per voxel was estimated using a random subset of 10,000 subjects).

## 2.4 Outlier removal

While the UKB data has undergone extensive quality control, the data still contains outlier samples, which were either biological outliers (large-scale anatomical/pathological anomalies) or caused by image artifacts. We developed a two-step outlier removal pipeline, primarily aimed at removing outliers of the latter kind with exception of very extreme cases (e.g., one participant with extensive postoperative tissue loss). This was followed by imputation of outlier voxels.

To find a good balance between removing subjects with image artifacts and not removing those with biological pathology, thresholds had to be manually determined for each modality. This was done by visual inspection of representative numbers of samples at different cut-off values, comparing average valued samples to cases with image artifacts as well as those showing plausible biological and pathological variation.

In step 1, we removed outliers with respect to mean image intensity (i.e., the row-wise mean of the full matrix). Similar to Alfaro-Almagro et al. (2021), we subtract the population median image intensity from the subject's mean image intensities and calculate the median absolute deviation (MAD) of these values (i.e., the median of the absolute value of the mean intensities). The demedianed mean intensities are then scaled by MAD. For most modalities a reasonable outlier threshold could be set on the absolute value of the MAD-scaled intensities, whereas for a few (notably T1 and FA), using different thresholds on negative and positive outliers gave a better demarcation of outliers with image artifacts. The thresholds for this first step ranged between 6-12 MAD.

Step 2 was aimed at removing outlier subjects with a large number of extreme-valued voxels or grayordinates. Here, differently to step 1, we performed MAD scaling on the columns of the full matrix rather than on the row-wise means. Specifically, we first subtracted the column-wise median from each entry of the matrix and then estimated column-wise MAD by taking, for each column, the median of the absolute values of the demedianed entries. The full matrix was then scaled using these column-wise MAD values. Because MAD can be zero, values below a numerical precision threshold were replaced by the corresponding column standard deviation divided by 1.4826 (using the approximation SD ≈ 1.4826 x MAD) before scaling. To reduce computational cost, column-wise medians and MADs were estimated on a random subset of 10,000 subjects.

Using this MAD-scaled matrix, we defined, for each participant, the number of extreme-valued voxels as the number of voxels exceeding a threshold (fixed at 6 for most sub-modalities). Having obtained these subject-level counts, we could then perform the same procedure on them as for the subject-level mean intensities, i.e., apply another round of MAD-scaling and set a second, sub-modality specific, threshold to these MAD-scaled counts, defining the outlier participants for step 2.

The first threshold of step 2 was set at a MAD-score of 6 for all sub-modalities except T1 and the Jacobian warp, where a higher initial threshold (MAD-score 20) resulted in a better separation of subjects with atrophy and subjects with warping errors. For the second threshold, optimal values per sub-modality varied more widely than for step 1, ranging from MAD-scores of 6 (e.g., for T2-FLAIR and SWI) up to 2000 for one of the task fMRI z-statistic maps.

In step 3, individual outlier voxels (or grayordinates) were imputed in the remaining subject matrix after outlier removal. That is, voxels above another sub-modality specific threshold in the previously demedianed and MAD-scaled matrix were set to 0, corresponding to median imputation. Manually determined thresholds for step 3 spanned a wide range, from MAD-scores of 8 (e.g., SWI T2*) up to 1000, with the overall aim of reducing noise- or artifact-related outliers without removing normal or pathological variation (e.g., large ventricles).

Step 1 was skipped for the Jacobian warp, where no satisfactory balance between sensitivity and specificity could be found. The outlier procedure was also not applied to the T2-FLAIR lesion map, as the binary source data rendered these steps unsuitable.

The manually determined thresholds are available within the PANDORA processing pipeline (https://git.fmrib.ox.ac.uk/PANDORA/pandora_proc).

## 2.5 Supervoxel encoding

All subject x voxel (or grayordinates) full-resolution matrices were separately encoded into a subject x 1K-supervoxel matrix and a second, more detailed, subject x 10K-supervoxel matrix, using independent component analysis (ICA). One supervoxel is one ICA component - a soft clustering of voxels which have highly similar subject variability to each other. We used the FastICA algorithm of Hyvärinen and Oja (2000), as implemented in scikit-learn (Pedregosa et al., 2011), with the scikit-learn randomized SVD function for whitening.

Briefly, for the full subject × voxels ($N \times V$) matrix $Y$, consider the SVD:

$$Y = U_{\mathrm{SVD}} \Sigma_{\mathrm{SVD}} V_{\mathrm{SVD}}^{\top}$$

where $U_{\mathrm{SVD}}$ are the $N$-dimensional subject eigenvectors, $V_{\mathrm{SVD}}$ are the $V$-dimensional spatial eigenvectors, and $\Sigma_{\mathrm{SVD}}$ is a diagonal matrix containing the non-negative singular values.

ICA is applied to the first $K < \min(N, V)$ of the spatial eigenvectors, finding a $K \times K$ mixing matrix $A_{\mathrm{ICA}}$ and $K$ statistically independent components in a $K \times V$ matrix $S$ such that

$$V_{\mathrm{SVD}(K)}^{\top} \approx A_{\mathrm{ICA}}\, S,$$

where the $(K)$ subscript denotes selecting first $K$ dimensions. These decompositions are combined into our $K$-dimensional approximation of the data

$$Y \approx U_{\mathrm{SVD}(K)} \Sigma_{\mathrm{SVD}(K)} A_{\mathrm{ICA}}\, S = A\, S$$

Where the $N \times K$ matrix $A = U_{\mathrm{SVD}(K)} \Sigma_{\mathrm{SVD}(K)} A_{\mathrm{ICA}}$ translates the $K$ ICA spatial components back into the original data domain.

Hence $A$ is the matrix of subject weights for the supervoxels and can generally be used instead of the full voxel data $Y$, for (e.g.) regressing imaging against other variables – i.e., it is the main variable in PANDORA used for new analyses. $S$ contains the spatial maps of the supervoxels, one map per supervoxel (ICA component). It can be used to interpret between-subject analyses carried out using $A$, or (as below) utilized in efficient ways *within* analyses in order that they may become equivalent to voxelwise analyses, but without the high-memory requirements of working with the full data (and with denoising, controlled by *K*).

Note that the subject weights $A$ can be connected back to the original data with the definition of $U$,

$$A = Y\, V_{\mathrm{SVD}(K)}\, A_{\mathrm{ICA}}.$$

This shows that the subject weights are just a linear combination of the voxelwise data, and thus if the columns of $Y$ are regarded as row-wise independent, the columns of $A$ can likewise be treated as independent.

## 2.6. Supervoxel GLM

In order to efficiently analyze the supervoxels and importantly bypass the reconstruction of a costly (huge) full-resolution matrix, we develop an adjusted general linear model (GLM) regression approach.

### 2.6.1 Setup

In addition to data $Y$, subject weights $A$, and supervoxel maps $S$, we have an $N \times P$ design matrix $X$, and some contrast, a row vector ($1 \times P$ matrix) $c$ or an $M \times P$ contrast matrix $C$. $X$ can include variables of interest as well as confounds (PANDORA is supplied with a pre-estimated set of imaging confounds, and the user can optionally add others, such as genetic principal components). This is a challenging setting because there are up to millions of voxels ($V$) and 82K subjects ($N$).

While the original, full data mass univariate model is

$$Y = X\beta^* + \epsilon^*$$

we are instead interested in a mass univariate model of the SVD-denoised data,

$$AS = X\beta + \epsilon. \tag{1}$$

The core assumption of the mass univariate linear model is independent errors (across subjects) for each voxel $i$. As noted above, the traditional assumption of independent subjects in $Y$ likewise justifies the independence, over rows, for each column of data of $A$, and this independence is maintained after spatial projection by $S$. This justifies an assumption of independent errors $\epsilon$.

### 2.6.2 Retaining the mean in the denoised model

Most statistical analyses treat the overall mean or intercept as a nuisance, and it is also the case that the ICA decomposition is performed on centered data. However, the mean subject-course can be a feature of interest, and thus we need to retain this information. We retain the "mean subject-course" (*Y* averaged across voxels) with the following approach. While the ICA approximation is based on the demeaned data

$$AS \approx Y - \bar{\mu}\mathbf{1}_V^\top,$$

where $\bar{\mu} = Y\mathbf{1}_V^\top / V$, we integrate $\bar{\mu}$ into the decomposition by defining this

$$A' = [\, A \quad \bar{\mu} \,] \text{ and } S' = \begin{bmatrix} S \\ \mathbf{1}_V^\top \end{bmatrix}$$

and building our approximation as

$$Y \approx A'S' = AS + \bar{\mu}\mathbf{1}_V^\top.$$

For simplicity, we will suppress the prime superscript going forward, and $AS$ is treated as including the mean subject-course. Note that the mean *image* has also been subtracted from the data (at an even earlier processing step), but that does not need to reappear for the purposes of the SVD, ICA or regression. The mean image however is included in the PANDORA distribution, because it can be useful for later visualizations. For example, for visualizing the average image of a subset of subjects $A_{subset}\, S$, the mean image should be added on.

### 2.6.3 Model estimation

We estimate as Equation (1) with ordinary least squares

$$\hat{\beta} = X^{+}AS = \hat{\beta}_A S$$

where $\hat{\beta}_A = X^{+}A$ combines the regression and subject weights, and $X^{+}$ denotes the Moore-Penrose pseudoinverse, equal to $(X^{\top}X)^{-1}X^{\top}$ when $X$ is full rank.

An essential insight is that while $\hat{\beta}$ is a large $P \times V$ matrix, a sufficient statistic for the regression is $\hat{\beta}_A$, a much smaller $K \times V$ matrix. However, we do not want to make inference on the $K$-dimensional regression coefficients $\hat{\beta}_A$, but in voxel space. Writing the $i$th voxel estimate as $\hat{\beta}_i = \hat{\beta}_A S_i$, where $S_i$ is the $i$th column of $S$, we now develop inference procedures in the voxel domain using $\hat{\beta}_A$.

### 2.6.4 Sample variance of estimates

As mentioned above, the traditional assumption of independent subjects justifies the row-wise independence of each $\epsilon_i$. Thus, the sampling variance for the estimate at the $i$th voxel is

$$\mathrm{Var}(\hat{\beta}_i) = \mathrm{Var}(X^{+}AS_i) = \mathrm{Var}\big(X^{+}(X\beta_i + \epsilon_i)\big) = X^{+}(X^{+})^{\top}\sigma_i^2$$

where $\sigma_i^2$ is the denoised model residual variance at voxel $i$.

### 2.6.5 Contrast inference

For a (row) contrast vector $c$, we wish to test the null hypothesis $H_0: c\beta_i = 0$ for each voxel $i$. For this we have estimate $c\hat{\beta}_i$ and sampling variance

$$\mathrm{Var}(c\hat{\beta}_i) = cX^{+}(X^{+})^{\top}c^{\top}\sigma_i^2.$$

For a contrast matrix $C$ we likewise test $H_0: C\beta_i = \mathbf{0}$, for which we need the sampling covariance of $C\hat{\beta}_i$

$$\mathrm{Var}(C\hat{\beta}_i) = CX^{+}(X^{+})^{\top}C^{\top}\sigma_i^2.$$

### 2.6.6 F-Test

The F-test at voxel $i$, noting that $C\hat{\beta}_i = C\hat{\beta}_A S_i$, is

$$F_i = \frac{S_i^{\top}(C\hat{\beta}_A)^{\top}(CX^{+}(X^{+})^{\top}C^{\top})^{-1}C\,\hat{\beta}_A S_i/M}{\sigma_i^2}.$$

To compute this for all voxels simultaneously, consider the computation in two steps, first whitening (technically, overwhitening) the $M \times V$ matrix of contrast estimates

$$\tilde{F} = (CX^{+}(X^{+})^{\top}C^{\top})^{-1}C\hat{\beta}_A S\,\mathrm{diag}\left\{\left(M\sigma_i^2\right)^{-1}\right\}$$

where postmultiplication by $\mathrm{diag}\{\cdot\}$ specifies a column-wise scaling, and then the final $1 \times V$ F-statistic image is the column-wise sum of the Hadamard product

$$\left(C\hat{\beta}_A S\right) \odot \tilde{F}.$$

Of course, in practice, one can do this all together, generating the F-image as

$$F = \mathbf{1}_M^\top \left( \left( C\hat{\beta}_A S \right) \odot \left( (CX^+(X^+)^\top C^\top)^{-1} C\hat{\beta}_A S \right) \right) \ \mathrm{diag}\left\{ \left( M\sigma_i^2 \right)^{-1} \right\}.$$

### 2.6.7 Residual error calculation

For the voxel $i$, its residual error is

$$\hat{\epsilon}_i = AS_i - X\hat{\beta}_A S_i = \left( A - X\hat{\beta}_A \right) S_i.$$

Naïve calculation of the sum of squared errors, $\hat{\epsilon}_i^\top \hat{\epsilon}_i$ does not exploit the low-dimensional structure, nor is easy to vectorize. Instead, consider the singular value-decomposition (SVD) of the $N \times K$ matrix of reduced-dimension residuals

$$A - X\hat{\beta}_A \ = U_e \Sigma_e V_e^\top$$

and write the residual error as

$$\hat{\epsilon}_i = U_e (\Sigma_e V_e^\top S_i) = U_e P_{e,i}.$$

where $U_e$ are the right eigenvectors of the reduced dimension and $P_{e,i}$ is a $K \times 1$ vector. Because $U_e$ is orthonormal, the sums of squares are

$$\hat{\epsilon}_i^\top \hat{\epsilon}_i = \left( U_e P_{e,i} \right)^\top U_e P_{e,i} = P_{e,i}^\top U_e^\top U_e P_{e,i} = P_{e,i}^\top P_{e,i},$$

i.e., just the sums of squares of $P_{e,i}$. Thus, for voxel $i$ the residual variance is

$$\hat{\sigma}_i^2 \ = P_{e,i}^\top P_{e,i} \ / \ (N - P),$$

and the residual variance can be computed for all voxels simultaneously as the column-wise sum of squares of $\Sigma_e V_e^\top S$ scaled by $(N - P)^{-1}$.

## 2.7 *fsl_glm* PANDORA expansion

The new supervoxel GLM method for PANDORA data is accessible via an expansion of the *fsl_glm* tool, which is part of the MELODIC toolbox in FSL (Jenkinson et al., 2012). The software, written in C++, has been adapted to process HDF5 data in separate voxel (/grayordinates) and supervoxel pipelines, given a PANDORA sub-modality folder. Both pipelines can be run in single- or multithreaded mode. The pipelines have been optimized for memory efficiency and speed. In particular, the full-resolution pipeline reads data from disk in chunks along the (stride-1) voxel axis, while the supervoxel pipeline does the same for the component-to-voxel mappings. All of the supervoxel GLM operations described above are implemented in this chunked, streaming fashion on the spatial maps, which keeps memory usage effectively constant with respect to the number of voxels/components. Supervoxel analyses are currently available for 1K and 10K components. Using the modality mask from the processing stage, the final statistical maps are output as images (NIFTI or CIFTI, and hence more convenient for display than HDF5). Because of the high-N setting, we output p-values as $-\log_{10}(p)$.

The expanded *fsl_glm* also provides new processing capability for CIFTI data. Moreover, the user can select one of two sets of pre-processed imaging confounds to include in the model.

Subsets of interest are handled simply by including only the relevant subjects in the *fsl_glm* design matrix and supplying a corresponding subject ID list. This allows for sex-specific analyses, discovery/replication splits, or cross-validation without modifying the pipeline. The supervoxel (ICA) decomposition is pre-computed once per modality on the full cohort and then held fixed for all such analyses; the GLM stage (including confound modeling and normalization) is then estimated on the chosen subset. Because the ICA step is fully unsupervised and independent of outcomes or group labels, reusing this basis does not compromise cross-validation.

We benchmarked runtimes (along with diskspace use) for small, medium and large modalities using the voxel vs supervoxel pipeline.

## 2.8 Confound processing

PANDORA comes with two sets of preprocessed imaging confounds (confounds_all and confounds_small) available for the full sample. The full set ("all") is over 200 confounds reflecting many technical and subject variabilities such as head motion and head size, and the reduced set just covers the 15 most important confounds (sex, head size, etc.). The confounds were processed using a new pipeline described in detail in an upcoming pre-print and following Alfaro-Almagro et al. (2021), which retains confounds that pass statistical tests of being relevant to the imaging data.

The small set of most important imaging confounds can be more appropriate when running analyses on a smaller subset of UKB subjects. This was achieved by keeping confounds for which the maximum absolute correlation across all IDPs was greater than 0.5, or where the median was greater than 0.04.

## 2.9. Encoding quality

To quantify the information content retained by the 1K/10K-supervoxel encoding, and, in comparison, by the multimodal IDPs, we estimated percent of variance explained for each modality by the respective encoding. Concretely, this is the amount of variance in the full data captured by the subspace spanned by its encoded representation.

Let $A \in \mathbb{R}^{m \times n}$ denote the full-resolution matrix and $B \in \mathbb{R}^{m \times r}$ the encoded basis (supervoxels or IDPs). $A$ is projected onto the column space of $B$ via its pseudoinverse:

$$\hat{A} = BB^{+}A, \;\; B^{+} = (B^{\top}B)^{-1}B^{\top}$$

We then compute the proportion of variance explained as the ratio of the squared Frobenius norms:

$$R^2 = \frac{\| \hat{A} \|_F^2}{\| A \|_F^2} = \frac{tr(A^{\top}P_B A)}{tr(A^{\top}A)}, P_B = BB^{+}$$

We report $100 \times R^2$ as % variance explained.

To investigate the overlap between supervoxels and IDPs, we further computed $R^2_{shared}$ as the variance explained of $A$ projected onto the subspace spanned by IDPs by $A$ projected onto the span of the supervoxels times the full-resolution variance captured by the IDPs:

$$R^2_{shared} = \frac{\| \hat{A}_{SV} \|_F^2}{\| \hat{A}_{IDPs} \|_F^2} \times R^2_{IDPs}$$

## 2.10. Applications of PANDORA

To assess the analytic potential of PANDORA and the supervoxel analysis pipeline, we performed a series of experiments of varying complexity, constructing regression design matrices from UKB variables and regressing against single- and multimodal data. All analyses were run with our expanded *fsl_glm*, which directly takes a PANDORA sub-modality folder together with simple text files specifying subject list, simple or complex design matrix and contrasts as input, and can straightforwardly switch between full-resolution and supervoxel analyses. Pre-computed imaging confounds are by default automatically concatenated with the input design within *fsl_glm*.

For single-variable designs, we supplied a text file containing the variable of interest and a matching subject list; *fsl_glm* then constructed the full design matrix internally by appending the selected imaging confounds and applying column-wise demeaning. Rows with missing values in any design column are automatically removed. Contrasts for positive and negative main effects were specified as simple two-row text files. More complex designs (e.g., multiple behavioral or genetic regressors and subtractive terms) were handled in exactly the same way by passing multi-column design and contrast matrices; from the user's perspective, the interface is identical for voxel and supervoxel analyses.

All main analyses used the full set of imaging confounds (confounds_all; see above) and demeaned designs. We first ran simple single-variable experiments (neuroticism score, Alzheimer's disease polygenic risk score (AD PRS), and effect of smoking) to verify the behavior of the pipeline and to compare 1K/10K-supervoxel with full-resolution regression in a straightforward setting. The core results reported in this paper are based on five more complex experiments (I–V), each designed to address a distinct scientific question: the impact of cumulative trauma, differential anxiety–depression effects, multimodal signatures of common substances, a specific *EPHA3* variant, and early- versus late-diagnosis autism polygenic scores. Table 2 summarizes experimental characteristics, used confounds and number of performed tests.

| ***Experiment*** | **N subjects** | **Sex (% f.)** | **Age (mean ± SD)** | **Confounds** | **N sub-modalities / contrasts** |
|---|---|---|---|---|---|
| *I: Cumulative Lifetime Trauma* | 60,345 | 54.7 | 66.5 ± 7.8 | Townsend deprivation index, confounds_all | 13 / 2 |
| *II: Anxiety vs. Depressive Symptom Load* | 67,009 | 54.2 | 66.4 ± 7.8 | Townsend deprivation, confounds_all | 12 / 8 |
| *III: Alcohol, Coffee and Smoking* | 78,277 | 53.4 | 66.4 ± 7.9 | Townsend deprivation index, ranked education, confounds_all | 13 / 14 |
| *IV: EPHA3 (rs987748)* | 67,131 | 52.5 | 66.8 ± 7.9 | 40 genetic PCs, confounds_all | 16 / 2 |
| *V: Early- vs. late-autism polygenic scores* | 67,131 | 52.5 | 66.8 ± 7.9 | 40 genetic PCs, confounds_all | 10 / 8 |

***Table 2.*** *Experimental characteristics for the five main analyses.*

Regressors of interest for the five experiments were constructed as follows:

Cumulative lifetime trauma score was calculated as the mean (after mapping to common scale) of the following semi-quantitative items from the adverse life events section of the mental well-being online follow-up: Experienced a life-threatening injury or illness (ID: 29087), experienced a violent or sexual assault (ID: 29086), experienced the death of a close friend of family member due to suicide (ID: 29090), experienced the death of a spouse or partner (ID: 29089), felt hated by family member as a child (ID: 29078), physical violence by partner or ex-partner as an adult (ID: 29083), physically abused by family as a child (ID: 29088), sexual intercourse by partner or ex-partner without consent as an adult (ID: 29085), sexual interference by partner or ex-partner without consent as an adult (ID: 29084), sexually molested as a child (ID: 29084), and

stopped from seeing friends or family by partner or ex-partner as an adult (ID: 29081). Townsend deprivation index (ID: 22189) was added as confound to the design.

Anxiety and depressive symptom load were estimated as the first principal component of anxiety and depressive symptoms reported (and nan-averaged) across two online follow up questionnaires.

Items for anxiety comprised, in descending order of loading on the first principal component: recent worrying too much about different things (loading = 0.46; IDs: 20520, 29060), recent trouble relaxing (loading = 0.44; IDs: 20515, 29061), recent inability to stop or control worrying (loading = 0.43; IDs: 20509, 29059), recent feelings of nervousness or anxiety (loading = 0.41; IDs: 20506, 29058), recent feelings of foreboding (loading = 0.32; IDs: 20512, 29064), recent easy annoyance or irritability (loading = 0.31; IDs: 20505, 29063), and recent restlessness (loading = 0.21; IDs: 20516, 29062).

Items for depression comprised, in descending order of loading: recent feelings of tiredness or low energy (loading = 0.56; IDs: 20519, 29005), recent lack of interest or pleasure in doing things (loading = 0.38; IDs: 20519, 29005), recent feelings of depression (loading = 0.37; IDs: 20510, 29003), recent feelings of inadequacy (loading = 0.36; IDs: 20507, 29007), recent poor appetite or overeating (loading = 0.36; IDs: 20511, 29006), recent trouble concentrating on things (loading = 0.34; IDs: 20508, 29008), recent changes in speed/amount of moving or speaking (loading = 0.12; IDs: 20518, 29009), and recent thoughts of suicide or self-harm (loading = 0.11; IDs: 20513, 29010).

The first principal component explained 70.0% and 58.3% of answers to anxiety and depression questions, respectively. Townsend deprivation index (ID: 22189) was added as a confound.

For smoking, coffee and alcohol we used items from the lifestyle and environment questionnaire, i.e., past tobacco smoking (ID: 1249, semi-quantitative: never smoked, tried once or twice, smoked occasionally and smoked on most or all days), coffee intake (ID: 1498, quantitative: cups per day), and alcohol intake frequency (ID: 1558, semi-quantitative: never, special occasions only, one to three times a month, once or twice a week, three or four times a week, daily or almost daily). As for all analyses, the design matrix was demeaned and standardized within *fsl_glm*. Maximum level of education obtained from the qualifications item (ID: 6138) in the sociodemographics touchscreen questionnaire together with Townsend deprivation index (ID: 22189) were added as confounds.

For the *EPHA3* experiment, the regressor of interest was the additive dosage of SNP rs987748, coded as the expected minor-allele count per subject. Dosages were extracted from the UK Biobank imputed genotype data (BGEN format) in the discovery and replication subsets and then merged by subject ID into a single dosage vector. 40 genetic principal components (ID: 22009) were added as confounds to the design matrix. As in all analyses, the design was demeaned within *fsl_glm*, and subjects with missing genotype or genetic principal component values were excluded.

A recent age-of-diagnosis–stratified autism GWAS (Zhang et al., 2025) reported two partially separable common-variant components corresponding to earlier vs later autism diagnosis. Using the public summary statistics for these components, we constructed two polygenic scores (Choi et al., 2020) in UK Biobank by harmonizing alleles, performing linkage disequilibrium (LD) based clumping with PLINK ($p_1$ = 0.001, $r^2$=0.5, 250 kb; Purcell et al., 2007) using the UK Biobank imputed genotype panel as the LD reference**;** and summing dosage x β across clumped SNPs. The clumped SNP sets for the two scores did not overlap, and the resulting scores were (as expected) uncorrelated. Unlike typical polygenic risk score workflows, we did not tune clumping parameters or the p-value threshold, since our goal was to compare the general effects of predefined early vs. late factors rather than optimize prediction. The two scores were standardized and used as regressors of interest along with 40 genetic principal components (ID: 22009) as confounds.

Before applying clumping, the set of SNPs was restricted to those with minor allele frequency greater than 0.001, and Hardy-Weinberg equilibrium p-value less than 1E-7. Imputed SNPs with INFO score < 0.3 were excluded, leading to 20,329,180 SNPs retained. The 67,131 participants included in this experiment represent a maximal unrelated subset of all UK Biobank participants with scans available in Summer 2025, with recent white British ancestry (as determined by the UK Biobank variable *in.white.British.ancestry.subset*), with euploidy, and with no missing confounds. A random two-thirds subset was used for clumping; associations were assessed in the full sample (N = 67,131).

## 2.11 Regression experiment statistics

As in Gillis et al. (2025), we corrected for multiple comparisons using the hierarchical false-discovery rate (FDR) approach described by Benjamini and Bogomolov (2014).

While classical FDR correction (Benjamini & Hochberg, 1995) controls for the expected false discovery rate in a flat family of hypotheses, it does not account for data-driven selection across levels of a hierarchy.

We therefore used hierarchical FDR with two-layer selection (modalities and contrasts) and voxelwise testing within selected contrasts, following a bottom-up then top-down scheme:

**Bottom-up.** For each modality $k = 1, \dots, K$, for each contrast $l = 1, \dots, L$, we computed FDR-adjusted *p*-values for the underlying tests within the contrast (i.e., at every voxel/grayordinate). We summarized each contrast by the minimum adjusted *p*-value and submitted the resulting $L$ contrast summaries to a second FDR correction to obtain contrast-level adjusted *p*-values. We then summarized each modality by its minimum contrast-level value and submitted the resulting $K$ modality summaries to obtain modality-level FDR-adjusted *p*-values.

**Top-down.** We compared the $K$ modality-level FDR-adjusted *p*-values to $0.05$ and identified $K_{hit}$ significant modalities. Within each of these $K_{hit}$ modalities, we thresholded the $L_k$ FDR-adjusted summary *p*-values at $0.05 \times K_{hit} / K$, yielding $L_{k,hit}$ significant contrasts in modality $k$. The final step involves level-consistent thresholding of the underlying FDR-adjusted *p*-values across modalities and contrasts at $0.05 \times (K_{hit}/K)\left(\sum_k L_{k,hit}\right)/(K_{hit}L) = 0.05 \times \left(\sum_k L_{k,hit}\right)/(KL)$.

In the current preprint version, we apply the final threshold in a modality-specific manner (i.e., not pooling across modalities) at $(0.05 \times K_{hit} / K) \times (L_{k,hit} / L_k)$. We plan to revise this final step to the level-consistent cutoff above in a subsequent version of this paper (*for the results reported here, we expect only minimal changes, mainly slightly greater sensitivity for weaker modalities and slightly reduced sensitivity for the strongest ones*).

## 2.12. Ethics approval

The UK Biobank study was approved by the North West Multi-centre Research Ethics Committee (reference 11/NW/0382). The present project was authorized by UK Biobank under application ID 8107. All procedures were conducted in accordance with the principles of the Declaration of Helsinki.

## 3. Results

### 3.1 Variance explained

Figure 1 summarizes variance explained across modalities by 1K/10K supervoxels versus multimodal IDPs (~5K). On average, 10K-supervoxels captured 95.9% ± 6.2% (range 62.9 – 100.0) of full-resolution variance, 1K-supervoxels 58.3% ± 10.0% (range 32.5 – 95.0), and IDPs 19.1% ± 9.9% (range 7.6 – 54.3). Thus, both supervoxel encodings substantially outperform IDPs, with 10K closely approximating full-resolution data. Consistent with expectations, modalities with higher voxel counts and/or greater inherent noise (e.g., quantitative susceptibility mapping (QSM), diffusion tensor imaging (DTI)-derived mode of anisotropy (MO)) showed lower explained variance, whereas lower-resolution CIFTI data and smoother maps (VBM, warpfield Jacobian) exhibited higher variance. Analysis of shared explained full variance between IDPs and supervoxels showed that except for RSN_d50 (50 resting state network components), most variance explained by IDPs could also be explained by the supervoxels (higher ratios for 10K).

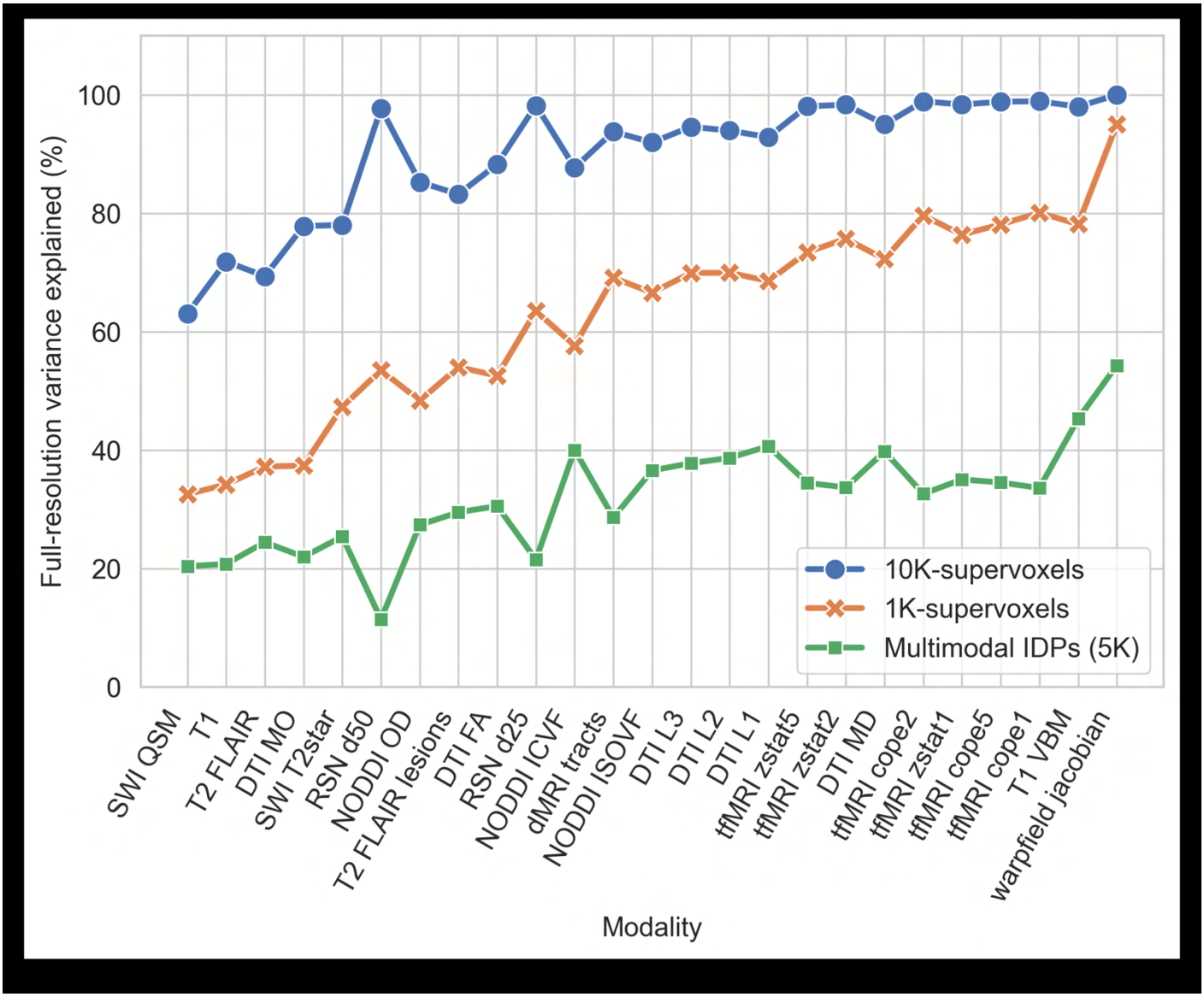


***Figure 1. Full-resolution variance explained by PANDORA supervoxels vs. multimodal IDPs.*** *For each of the 98 imaging sub-modalities, we show the percentage of voxel/grayordinate-level variance captured by 1K-supervoxel, 10K-supervoxel, and multimodal IDP encodings. Across modalities, both supervoxel encodings capture substantially more variance than IDPs, with 10K-supervoxels closely approximating full-resolution data and 1K-retaining a majority of the signal. Variance explained is modality-dependent, with inherently noisier sub-modalities (e.g., QSM, DTI MO) showing lower values and smoother or lower-resolution maps (e.g., VBM, warpfield Jacobian, CIFTI fMRI) showing the highest.*

## 3.2 Benchmarks

Runtime for a typical regression using 1K-supervoxels was orders of magnitude below 10K and full-resolution analyses across five tested modalities of different voxel/grayordinate count (Fig. 2AB) and increased only slightly with higher number of datapoints.

Because the SVD step used in the supervoxel analysis has a time complexity of $\Theta(n^2)$, going from 1K to 10K voxels results in a ~100x increase of runtime. In comparison with the full-resolution experiments this leads to a runtime disadvantage for low resolution modalities, i.e., the CIFTI data and T1 VBM images, while the gray matter masked diffusion modalities run at approximately the same speed, and there is a ~2x advantage for the 10K supervoxels for higher resolution modalities (susceptibility-weighted imaging (SWI) derived QSM and normalization warpfield Jacobian).

Figure 2C further illustrates highly reduced peak memory consumption for 1K-supervoxels in comparison to 10K-supervoxels and full-resolution image at default settings. We note that memory consumption is highly dependent on settings (specifically, number of parallel threads and chunking size).

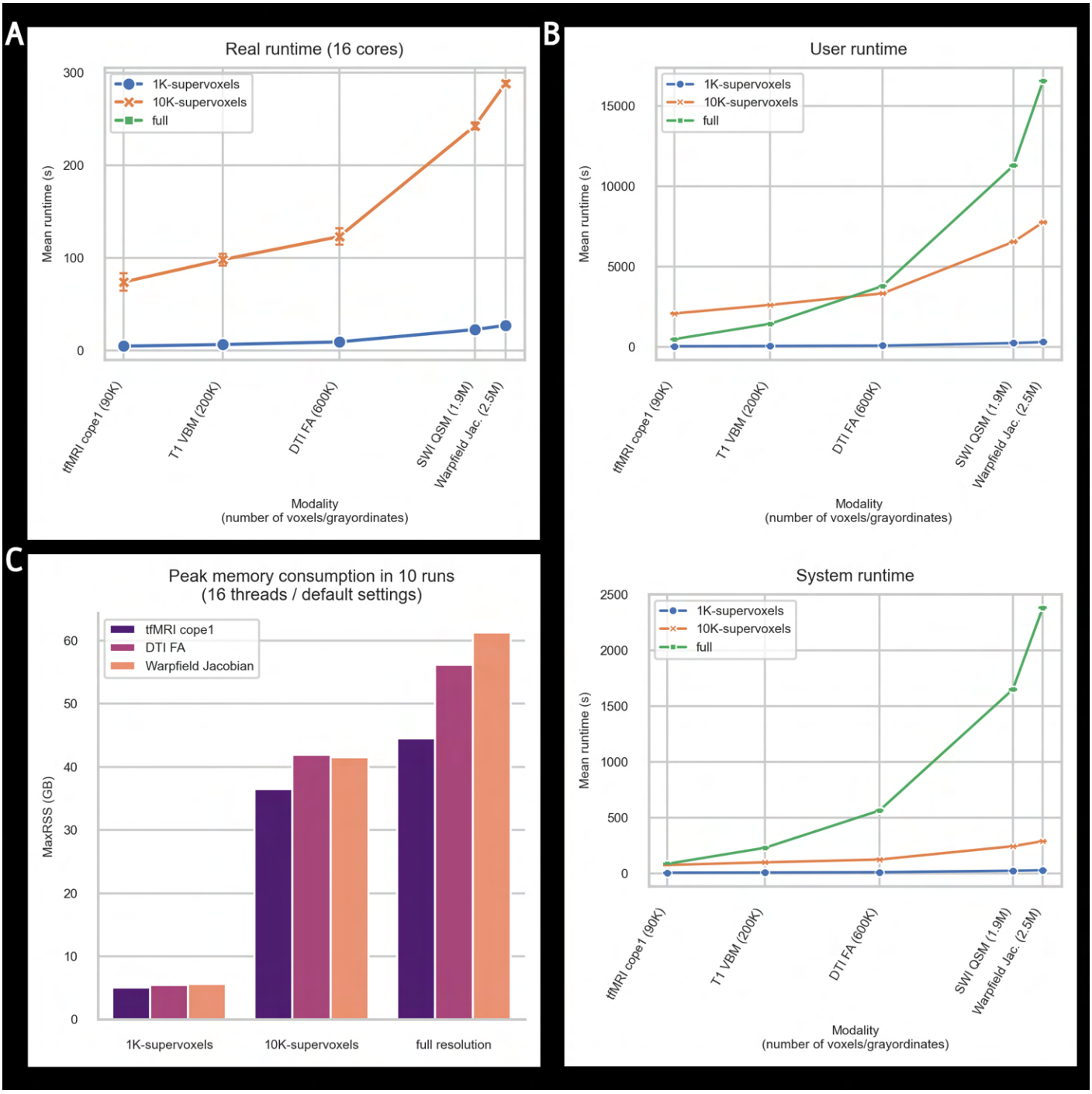


***Figure 2. fsl_glm benchmarks.*** *A: Comparison of real runtime using 16 cores. While the 1K-supervoxel analysis is clearly faster than the other options, 10K-supervoxels have the advantage over full voxels at higher voxel counts. B: Runtime portioned into single-threaded user- and system runtime. While compute is non-system dominated, system runtime reflects the massive overall reduction in I/O dependent processes. C: 1K-supervoxels require between 6 – 10x less peak RAM than 10K-supervoxels and full-resolution analyses across different size sub-modalities using default settings (note: RAM consumption is dependent on settings, e.g., chunk size).*

## 3.3 GLM experiments

### 3.3.1 Comparison between 1K, 10K and full-resolution analyses

Comparison between 1K-/10K-supervoxel and full-resolution GLM experiments revealed that the 10K-supervoxel analysis is a spatially highly accurate replacement of the full-resolution data with added benefit of denoising, while the 1K-supervoxels deliver increased power for the detection or ruling out of weaker, distributed effects, and in many cases retaining almost as much spatial detail as 10K..

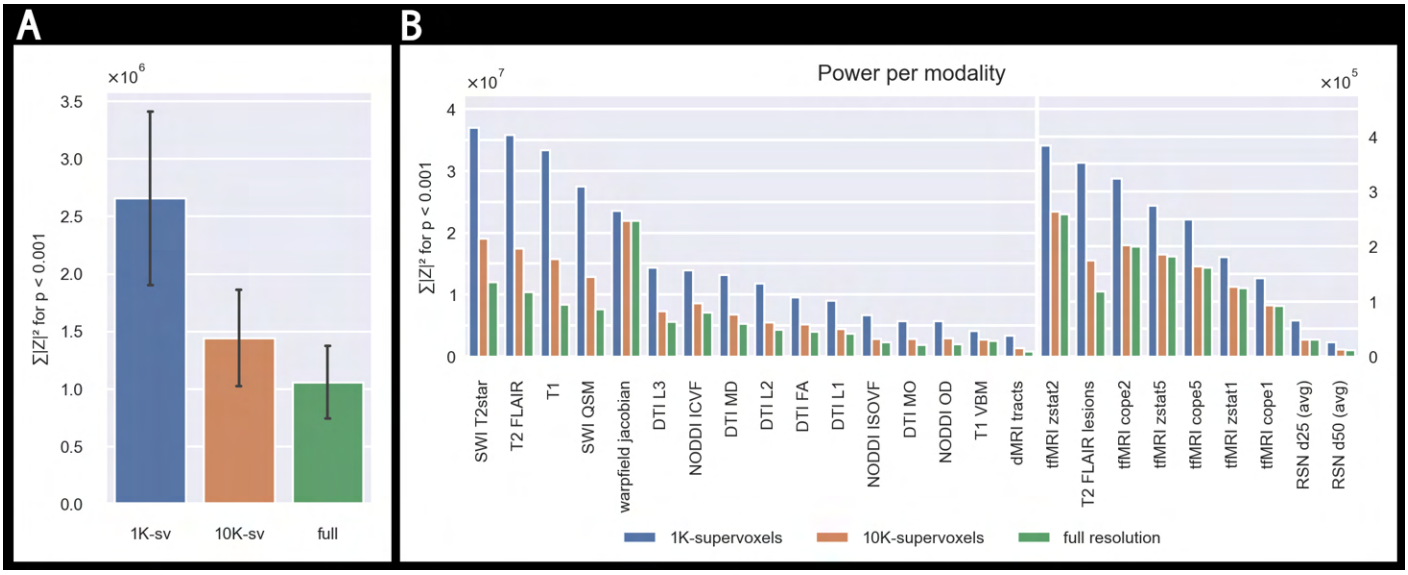


***Figure 3. Statistical power across 98 imaging modalities (effects of past tobacco use).*** *A. Power across modalities, as measured by the mean (± SEM) of squared z-statistic maps for voxels or grayordinates with uncorrected p < 0.001, was highest for 1K-supervoxels, followed by 10K supervoxels. B. Comparison within modalities, moreover, showed that this general pattern held true for all modalities, with the difference between 10K and full resolution being smaller for the lower resolution fMRI (CIFTI) data and spatially smoothed modalities (VBM / warpfield Jacobian).*

Figure 4 illustrates this difference in statistical significance for the strong effect of nicotine use (UKB ID 1249: past tobacco consumption) on VBM and QSM images, thresholded at three increasingly stringent hierarchical FDR corrected p-value levels ($p < 0.023$, $2.9 \times 10^{-7}$, and $7.6 \times 10^{-24}$; corresponding to one-sided Gaussian significance levels of 2σ, 5σ, and 10σ). While power increased from full-resolution to 10K- to 1K-supervoxels for both VBM- and QSM-analyses, the denoising aspect of the supervoxels can be particularly appreciated on the relatively noisy QSM images. Spatial accuracy for 1K-supervoxels (compared with full-resolution) is very good for these broader effects, while the overlap is near perfect between 10K-supervoxels and full-resolution. Figure 4A focuses on the benefits and slight downsides of the 1K-supervoxels, showing how a weak effect in anterior hippocampus iron deposition in subjects with high neuroticism score is only detected using this mode, while a spatially specific strong association in central amygdala, does not reach the level of significance seen in 10K- or full-resolution mode. Figure 4B illustrates the near-perfect spatial agreement between 10K-supervoxels and full-resolution images.

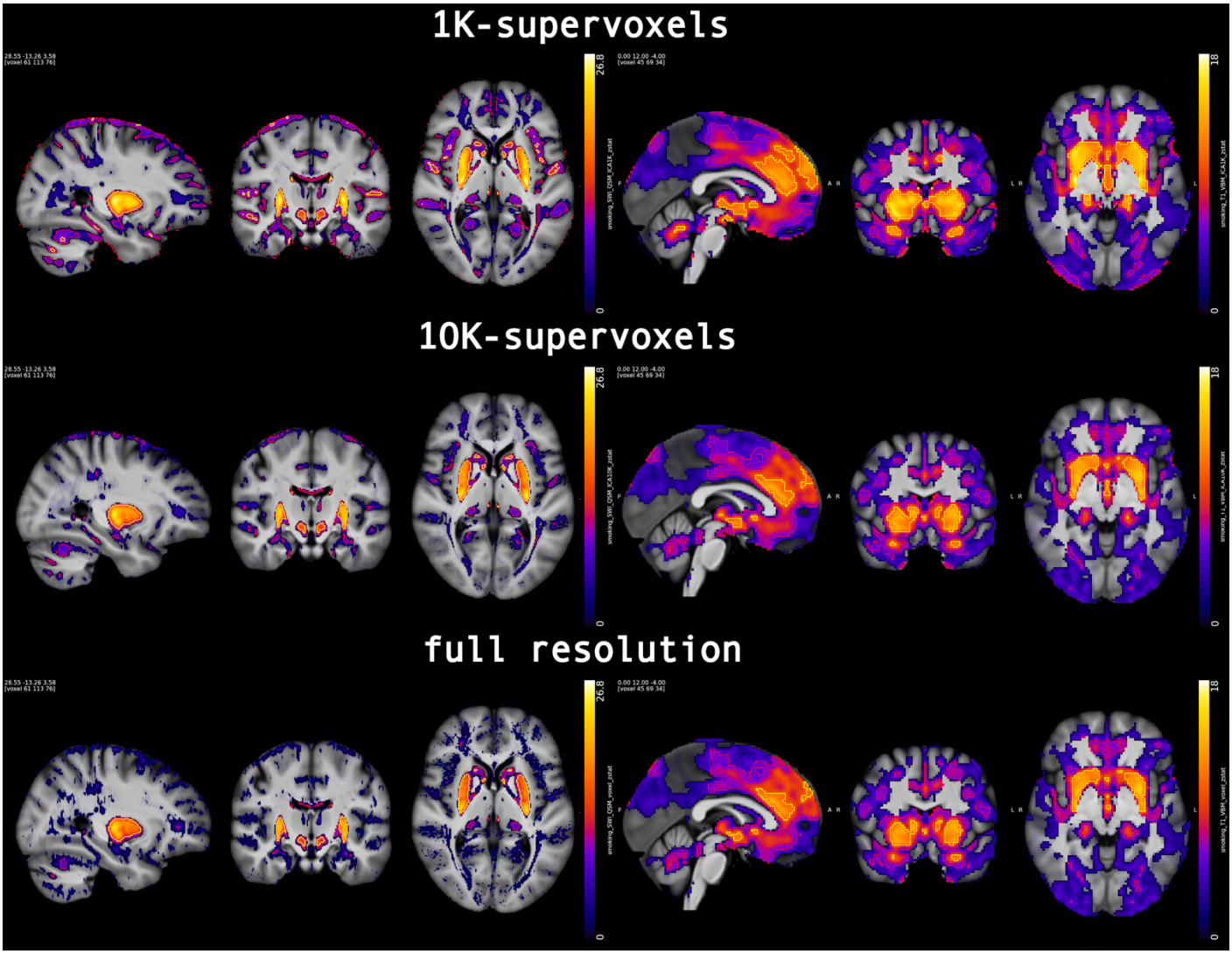


***Figure 4. Supervoxel vs. full resolution regression at 2, 5 and 10σ significance.*** *Statistical maps (-log$_{10}$P) of association of past tobacco smoking (UKB ID: 1249) with increased QSM (left) and decreased VBM signal (right), thresholded at hierarchical FDR levels below 0.023 (black), 2.9 x $10^{-7}$ (red) and 7.6 x $10^{-24}$ (yellow). While power increases from full-resolution to 10K- to 1K-supervoxels, the 10K-supervoxel maps shows high spatial convergence with the full data (see also fig. 5). The denoising aspect of the supervoxels can be seen particularly well in the sulcal spaces in QSM.*

*Peak z-values for the 1K-, 10K-supervoxels and full-resolution were at 26.298, 25.318 and 24.558 in left putamen for QSM. For comparison, z-value for the effect of smoking on the median QSM IDP for left putamen (UKB ID: 24471) was at 20.351. For VBM, peak z-values were at -17.603, -16.245 and -16.093 in left putamen, while z-statistic for the left putamen gray matter volume IDP (UKB ID: 25882) was at -11.715.*

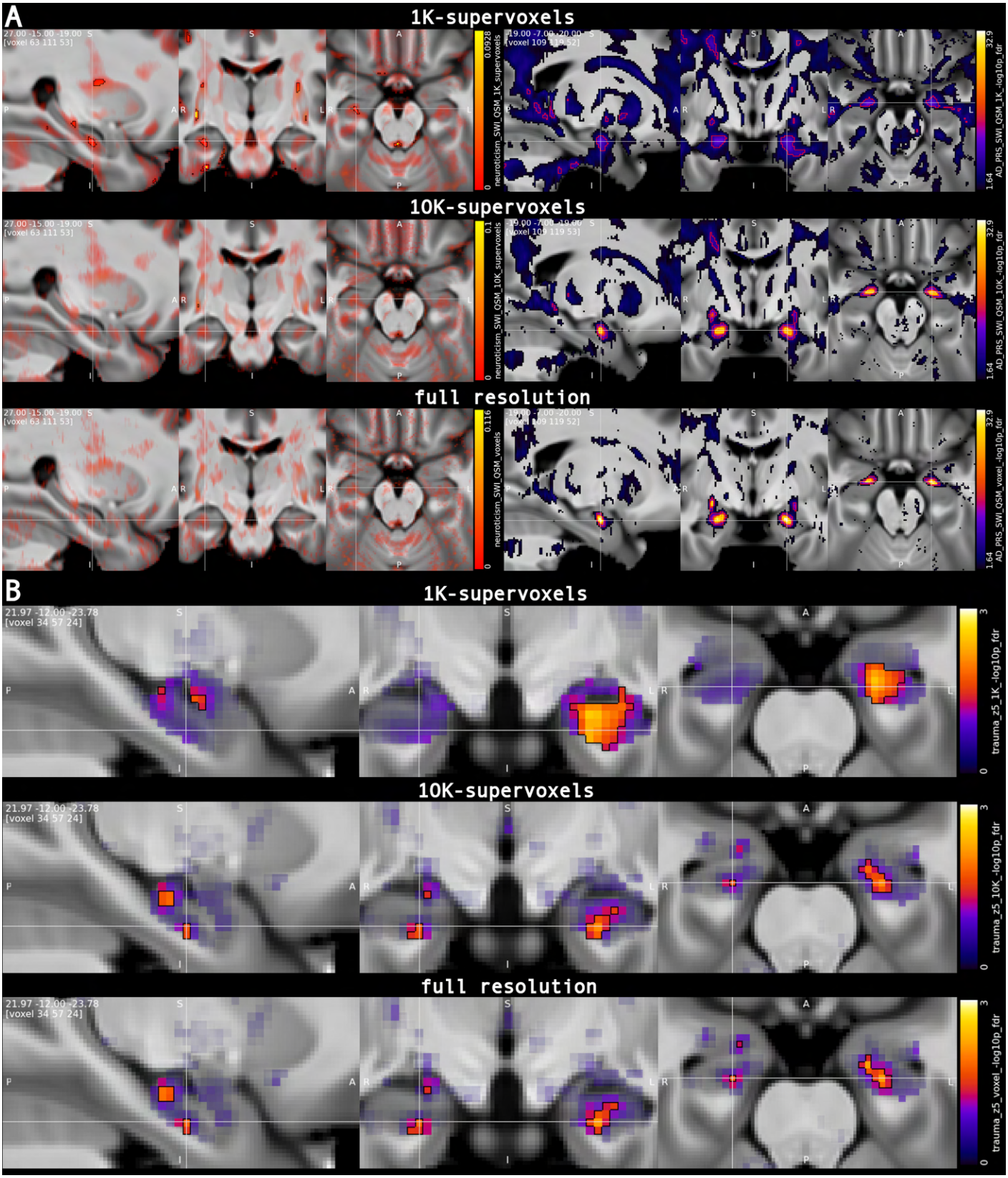


***Figure 5. 1K- or 10K-supervoxels: which to choose?*** *A. The higher statistical power of the 1K-supervoxels can detect subtle effects, which may otherwise not reach significance, as seen on the left for an increase in right anterior hippocampus QSM associated with neuroticism. Highly localized effects, however, may become less clear than when using 10K- and full resolution analyses (right: Alzheimer's disease polygenic risk score associated with QSM in amygdala). B. 10K-supervoxels exhibit high spatial accuracy in comparison with full-resolution analyses, as seen here for the effect of cumulative traumatic life-events on task fMRI (faces – shapes).*

### 3.3.1 **Experiment 1:** Effect of cumulative trauma on brain

Cumulative trauma scores corrected for deprivation score showed significant effects in twelve of thirteen tested structural and functional modalities (Figs. 6.1 and 6.2). Results are reported from the 10K-supervoxel analysis, except where otherwise denoted. We classify evidence as strong for associations surviving hierarchical FDR correction at *p_hFDR* < 0.001, and as moderate p_hFDR; the overall significance threshold is *p_hFDR* < 0.05. Peak statistics for all experiments are summarized in supplementary tables file.

Overall calibration and the relative sensitivity of the voxelwise, 10K- and 1K-supervoxel pipelines are summarized in Figure 7, which contrasts observed −log10(p) distributions against permutation-derived and uniform-null expectations across sub-modalities. Below we summarize the main spatial patterns of association for each modality.

Anatomical localization for all experiments was primarily performed using the fourth edition of *Atlas of the human brain* (Mai et al., 2015). Prefrontal cortex (PFC) definitions follow Carlén (2017), while thalamic subregions are reported with reference to a voxelized version of the Morel atlas (Jakab et al., 2012; Krauth et al., 2010; Morel, 2007). For white matter tracts, the XTRACT HCP Probabilistic Tract Atlas (Warrington et al., 2020) and the JHU White-Matter Atlas (Hua et al., 2008) were used for cross-checking.

**Voxel-based morphometry (VBM):** Trauma was positively correlated with increased gray matter in right visual cortex (V1) and left ventromedial prefrontal cortex (vmPFC) with strong evidence. Moderate evidence was found for left V1, right vm- and dorsolateral (dl)PFC, across orbitofrontal cortices, left posterior fusiform gyrus, and in right paracentral lobule.

Strong evidence for gray matter decrease was found for bilateral amygdalo-hippocampal complex (incl. left entorhinal cortex), right substantia innominata, nucleus accumbens and left thalamus (VLp/VLa), bilateral parietal operculum and bilateral calcarine sulcus.

**Susceptibility weighted imaging (SWI) – quantitative susceptibility mapping (QSM):** Increase in QSM was seen with strong evidence in bilateral substantia nigra, striatum, amygdalo-striatal transition area, left medial forebrain bundle and in the right entorhinal cortex. QSM was decreased with strong evidence in lateral geniculate nuclei (LGN) with adjacent white matter, left ventrolateral thalamus (VLpv), right lateral hypothalamic area / substantia innominata, internal and external capsule white matter (extending to frontal operculum), temporal cortices (entorhinal, inferior temporal gyrus), and cerebellum.

**SWI T2$^*$:** Cumulative trauma exhibited widespread, strong evidence, positive associations with cerebral white matter in the parieto-occipital lobe, cingulum and along bilateral dorsomedial (dm)PFC. Peak evidence was, however, found at the gray matter/white matter boundary of the left fusiform gyrus. Negative associations were strongly supported for right anterior insula, left superior temporal gyrus and bilateral cerebellum.

**Neurite orientation and density imaging (NODDI) – intracellular volume fraction (ICVF):** Neurite density related marker ICVF was positively associated in left putamen only (moderate evidence), while strong evidence for a negative shift in ICVF signal was seen across the entire supra- and infratentorial white matter with a robust peak in the right centrum semiovale ($-\log_{10}(p)$_mapFDR > 15).

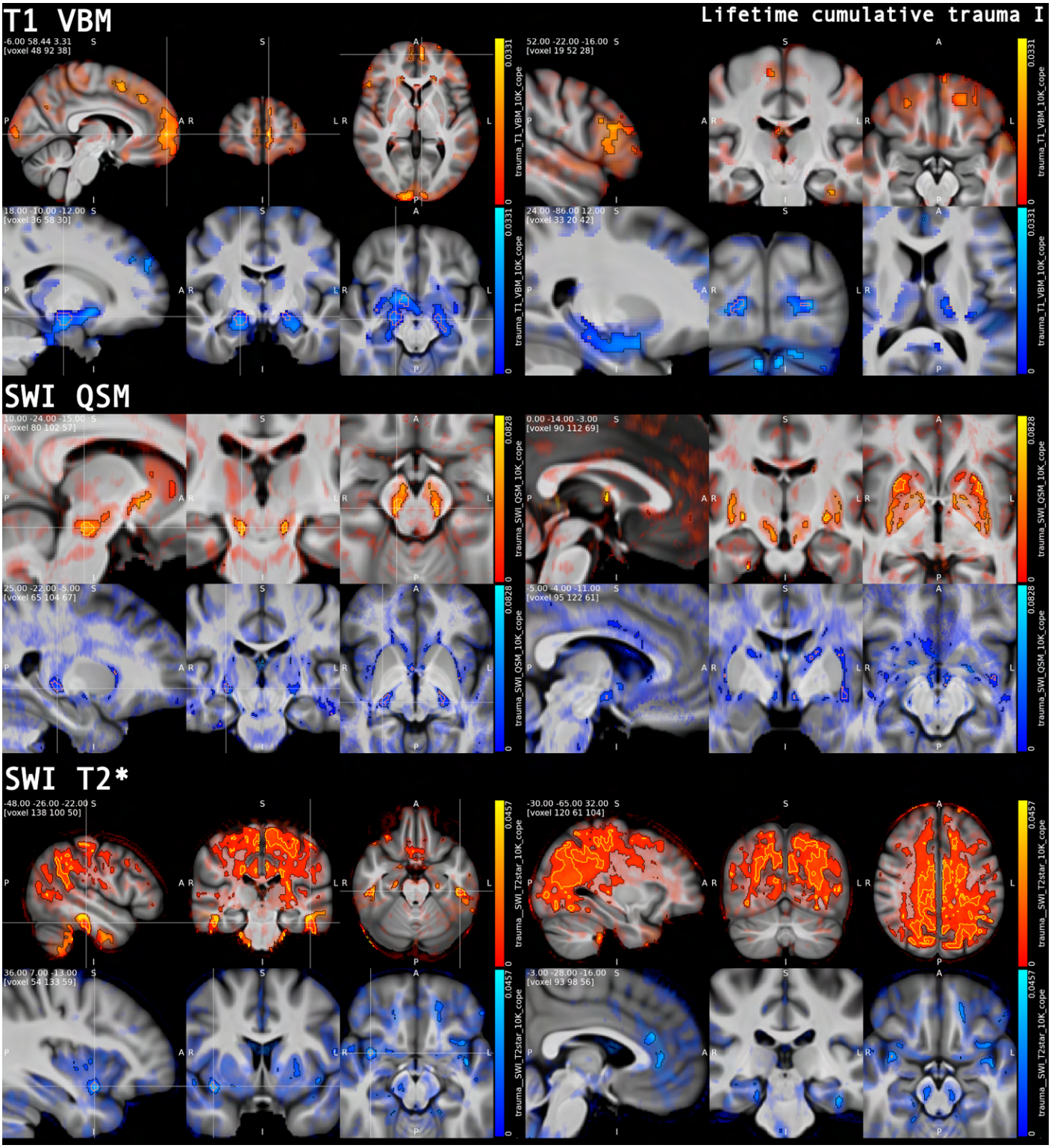


***Figure 6.1. Multimodal associations with cumulative trauma I: voxel-based morphometry (VBM) and susceptibility weighted imaging (SWI).*** *Life-time traumatic events showed distinct and distributed effects across modalities. Gray matter volumes (VBM) were increased in prefrontal and visual cortices and decreased in the amygdalo-hippocampal complex (peak in right dorsocaudal amygdala: Z = -7.110; right amygdala IDP (UKB ID: 25889) for comparison: Z = -4.171). Quantitative susceptibility mapping (QSM) exhibited signs of iron accumulation in dopaminergic circuitry, while T2* images revealed widespread alterations in parieto-occipital white matter and specifically, in bilateral fusiform cortices. Common visualization conventions (Figs. 6.1-6.2): β-maps thresholded at hierarchical FDR corrected p < 0.05 (black outline) overlaid on non-significant effects modulated by Z-statistic (transparency without modulation for surface views), over mean T1-weighted image. Positive associations in red with yellow outline demarcating p_hFDR < 0.001, negative associations in blue with orange outline for p_hFDR < 0.001.*

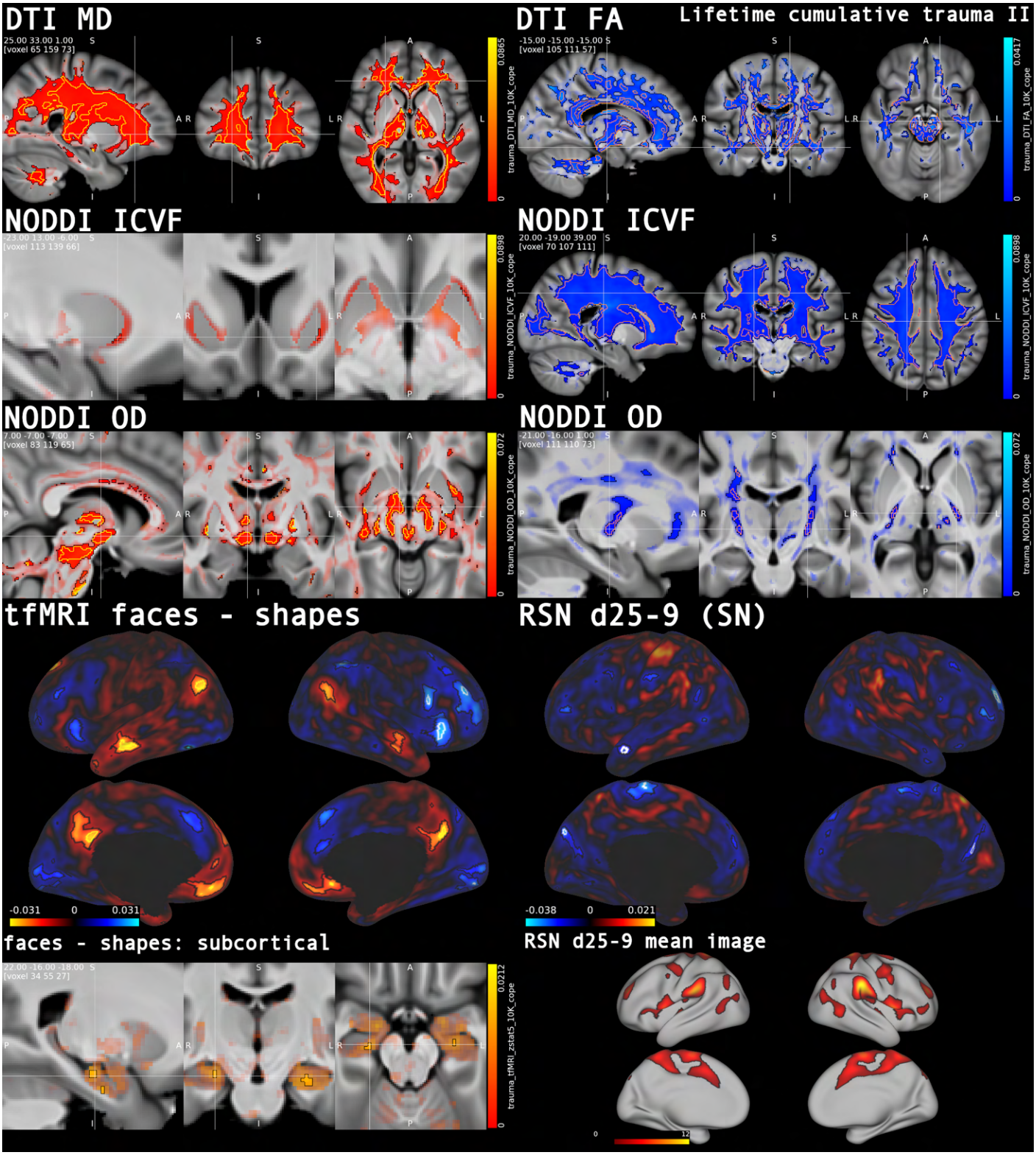


***Figure 6.2. Multimodal associations with cumulative trauma II: diffusion tensor imaging (DTI), neurite orientation dispersion and density imaging (NODDI) and functional MRI.*** *Global shifts in DTI- and NODDI-metrics (MD↑, FA/ICVF ↓) point towards reduced white matter integrity with higher loads of traumatic events. Intriguingly, peak positive association with orientation dispersion (OD) was found in hypothalamus (which also showed a decrease in QSM). Functionally, trauma was associated with increased activity of areas resembling the default mode network including anterior hippocampus during the emotional faces task of Hariri et al. (2002). (Common visualization conventions in Fig. 6.1).*

**NODDI orientation dispersion (OD):** We observed strongest support ($-\log_{10}(p)$_mapFDR > 10) for increased OD in right hypothalamus and white matter in between lateral substantia nigra and red nuclei. Further areas of strong evidence were right hypothalamus, bilateral thalamus, general substantia nigra area, and white-matter tracts along bilateral striatum and distinct cortical regions such as bilateral entorhinal and cingulate cortex.

Strongly supported negative associations were most prominent along bilateral corticospinal tract.

**DTI mean diffusivity (MD):** Evidence was strong for a global positive shift of MD, markedly, in fronto-parietal white matter with peak in the right anterior corona radiata. There were no negative associations with MD.

**DTI fractional anisotropy (FA):** FA was reduced throughout major supra- and infratentorial tracts with robust evidence for the left cerebral peduncle ($-\log_{10}(p)$_mapFDR > 15). There were no significant positive associations with FA.

**Task functional MRI (tfMRI) z-statistic (zstat) (effect of negative faces):** The main effect of negative faces from the emotion task showed moderate evidence for a positive association with right precuneus, and moderate evidence for a negative association with right supramarginal gyrus.

**tfMRI zstat (negative faces − neutral shapes):** For the faces − shapes contrast, we saw strong evidence for a positive association with left middle temporal gyrus, and the default mode network (specifically, bilateral precuneus, medial (m)PFC and left angular gyrus). Strong evidence for negative association was seen with right ventrolateral (vl)- and dlPFC, right anterior insula and angular gyrus.

**RSN d25-2 (DMN):** Trauma showed moderate evidence of a negative association with the default mode network (RSN d25-2) in the left precuneus. No significant positive association was seen.

**RSN d25-9 (SN):** Strong evidence was found for a negative association of trauma with the salience network-like RSN d25-9 component in left middle temporal gyrus, left paracentral lobule, bilateral cuneus and right dmPFC indicating reduced coupling in these regions.

**RSN d25-13 (SMN):** Moderate evidence was found for a negative association a somatomotor-like network in the left angular gyrus.

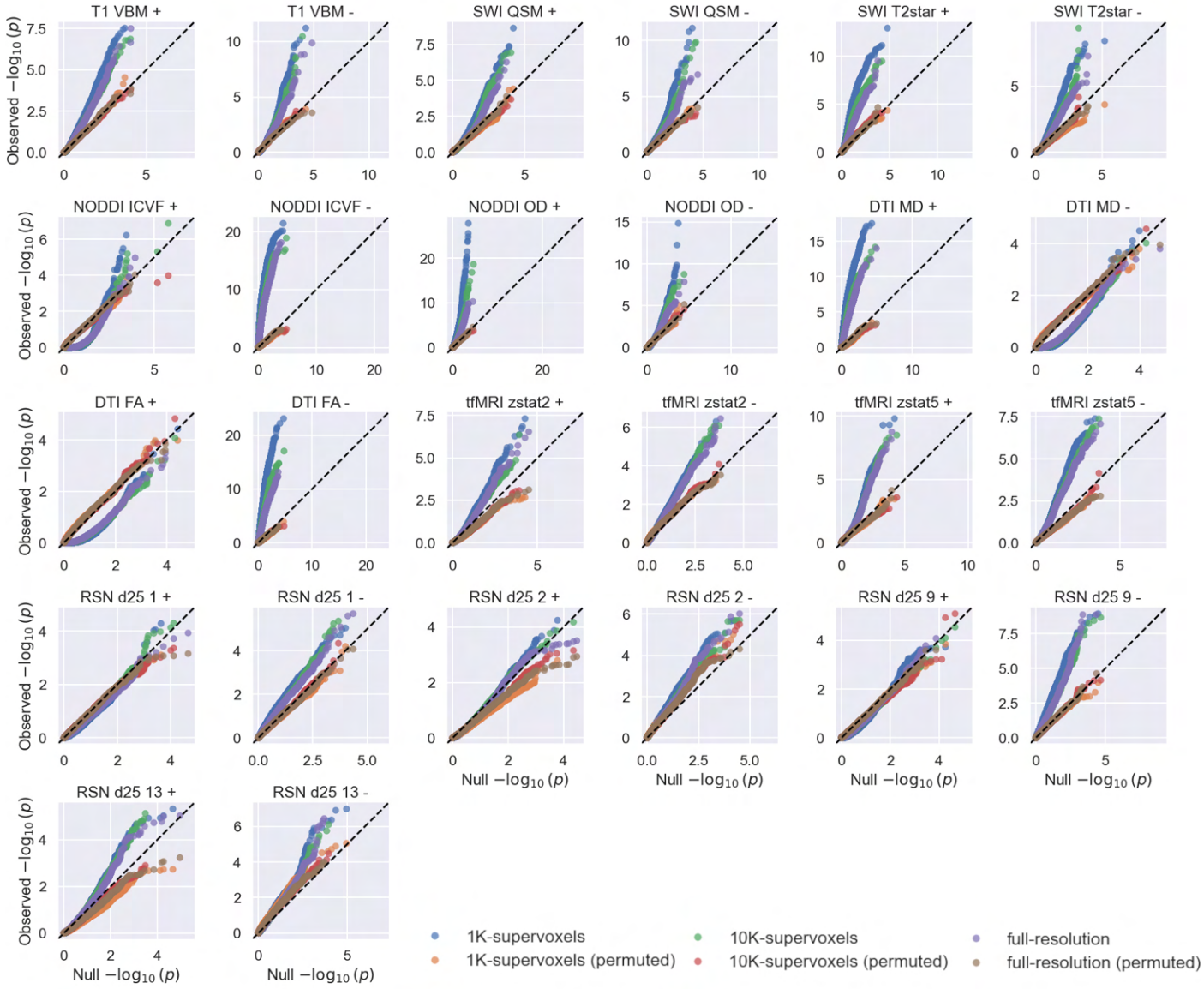


***Figure 7. Observed vs. permuted vs. expected -log$_{10}$(p) distributions for the lifetime cumulative trauma multimodal analysis.*** *For each sub-modality, contrast and pipeline (1K-, 10K-supervoxels and full-resolution), we compare the empirical voxel/grayordinate-wise association p-values (observed) to a null distribution generated by permutation of the trauma regressor (permuted), and to the uniform-null expectation (expected; black dashed line). Upward deviation of the observed curves from expected indicates excess signal beyond chance, while agreement between permuted and expected indicates good null calibration. Significant effects at p_hFDR < 0.05 were detected in each sub-modality except for RSN d25-1 (visual network).*

### **3.3.2 Experiment 2:** Disentangling anxiety and depressive symptoms in brain

Anxiety and depressive symptom principal components exhibited distinct effects across all 12 tested modalities (Figs. 8.1–8.6). In the following, we summarize the main associations and contrasts for these two symptom dimensions. We also revisited prior UK Biobank reports of absent Hariri-task amygdala associations (Tamm et al., 2022) by re-testing amygdala voxel-level reactivity using anxiety- and depression-specific symptom components, rather than using region-of-interest / IDP summaries (tfMRI zstat 1 – 5). Results are reported from the 10K-supervoxel analysis, except where otherwise denoted.

**VBM:** Moderate evidence was found for a positive correlation of anxiety with the right cerebellum (VIIb), while strong evidence was found for positive changes associated with depression in bilateral putamen, left dlPFC, right frontal operculum and anterior insula, optic chiasm/hypothalamic region, posterior fornix/corpus callosum, left anterior intra-parietal sulcus, left visual cortex (V1), and bilateral cerebellum.

Strong evidence for a negative association of anxiety with gray matter volume was found along vm-/dmPFC (midline) and bilateral cingulate sulcus. Strong evidence for widespread gray matter reduction was found for depression. This included bilateral amygdalo-hippocampal complex, bilateral straight gyrus, subgenual anterior cingulate cortex (ACC), posterior insula/parietal operculum, and bilateral pulvinar.

**SWI QSM:** QSM was not significantly associated with anxiety symptoms. Strong evidence was, however, found for increase in the right posterior insula and left cingulate sulcus for depression. QSM was negatively associated with the left bed nucleus of the stria terminalis (BNST)/anterior commissure.

**SWI T2$^*$:** Anxiety showed strong evidence for elevated T2$^*$ signal at gray matter/cerebrospinal fluid (CSF) boundary of bilateral dlPFC (peak in left hemisphere). No negative associations were found.

Depression associated with increased T2$^*$ in the subcallosal area, bilateral posterior inferior temporal gyrus and along right parieto-occipital white matter and cortex.

Decreased T2$^*$ was associated globally with cortex and external sulci with accentuation in prefrontal cortex and peak in the left dlPFC ($-\log_{10}(p)$_mapFDR > 10). Moreover, strong evidence for reduction was seen in anterior hippocampus.

We note that edge effects at brain/CSF boundaries should be interpreted with caution.

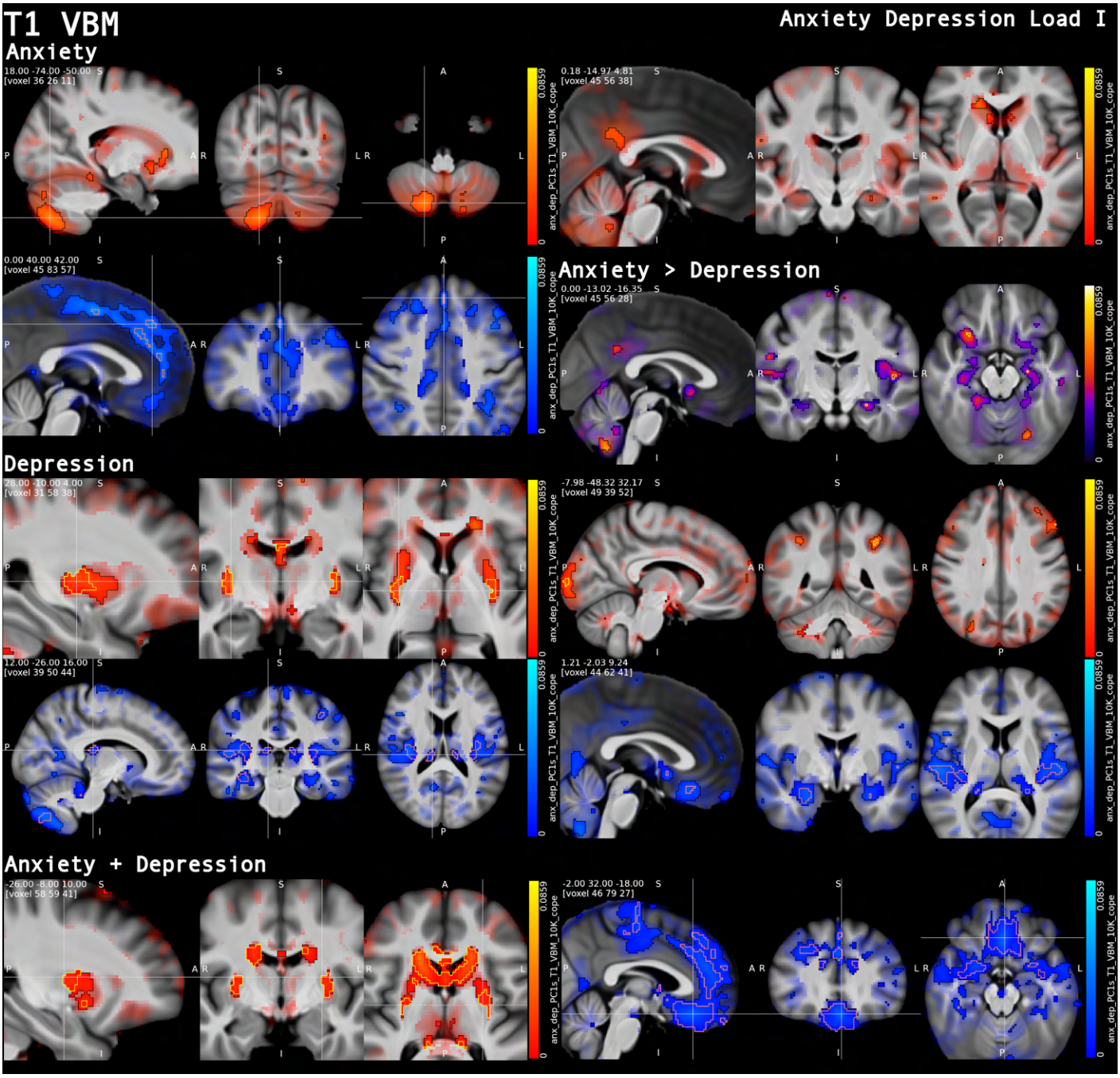


***Figure 8.1. Anxiety and depressive symptom load: voxel-based morphometry (VBM).*** *Anxiety and depression exhibited widespread volumetric brain changes such as volume loss across amygdala and hippocampus and increase in putamen for depression but volume increase in left anterior hippocampus and caudate for anxiety. Volume loss for anxiety was focused on medial prefrontal cortex, while an increase in the precuneus area was stronger for anxiety and decrease in subgenual anterior cingulate cortex (sgACC) and was stronger for depressive symptom load. Combined effects are displayed in the last row. Common visualization conventions (Figs. 8.1–8.6): β-maps thresholded at p_hFDR < 0.05 (black outline) overlaid on non-significant effects modulated by Z-statistic (surface views: non-significant effects shown by transparency, without Z-modulation), over the mean T1-weighted image. Positive associations are shown in red and negative associations in blue, contrast associations are displayed with a heatmap (NIH-fire); p_hFDR < 0.001 is outlined in yellow (positive and contrasts) or orange (negative), except on surface renderings, where p_hFDR < 0.001 is indicated in white. Group-mean resting-state network maps (Z-statistics) are thresholded at Z > 2.58 (approx. p < 0.01, two-tailed).*

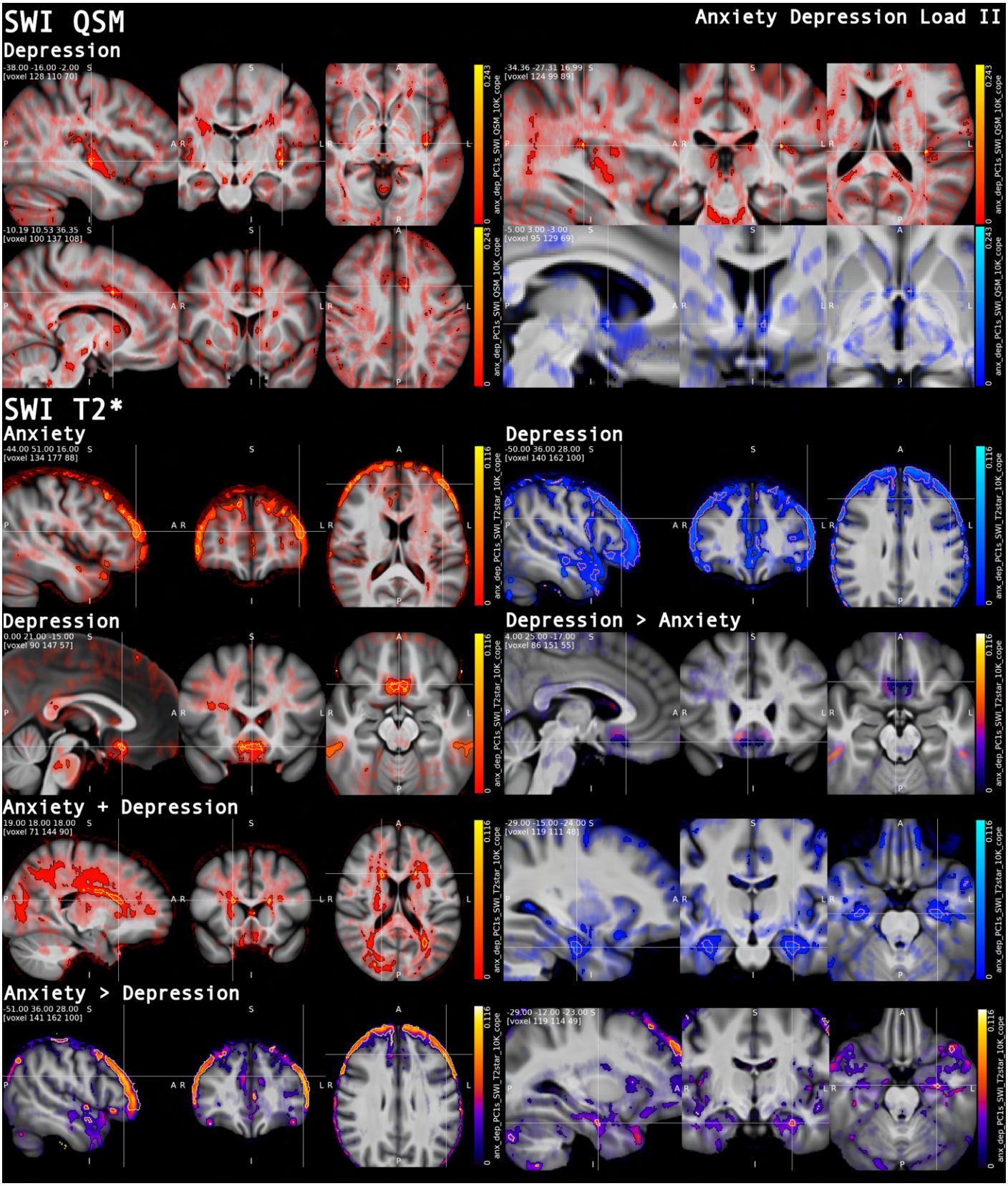


***Figure 8.2. Anxiety and depressive symptom load: SWI.*** *Depressive symptoms were associated (p_hFDR < 0.001) with higher QSM in posterior insula, left Heschl's gyrus and cingulate sulcus consistent with iron accumulation.T2* revealed a dissociated association with depression (↓) and anxiety (↑) surrounding and within frontal lobe cortex (peak: dlPFC). Decrease in depression, co-localized with QSM increase consistent with increased paramagnetic susceptibility (e.g., iron/venous effects). Surface-adjacent effects should, however, be interpreted with caution (e.g., partial volume or susceptibility artifacts). (See Fig. 8.1. for visualization conventions.)*

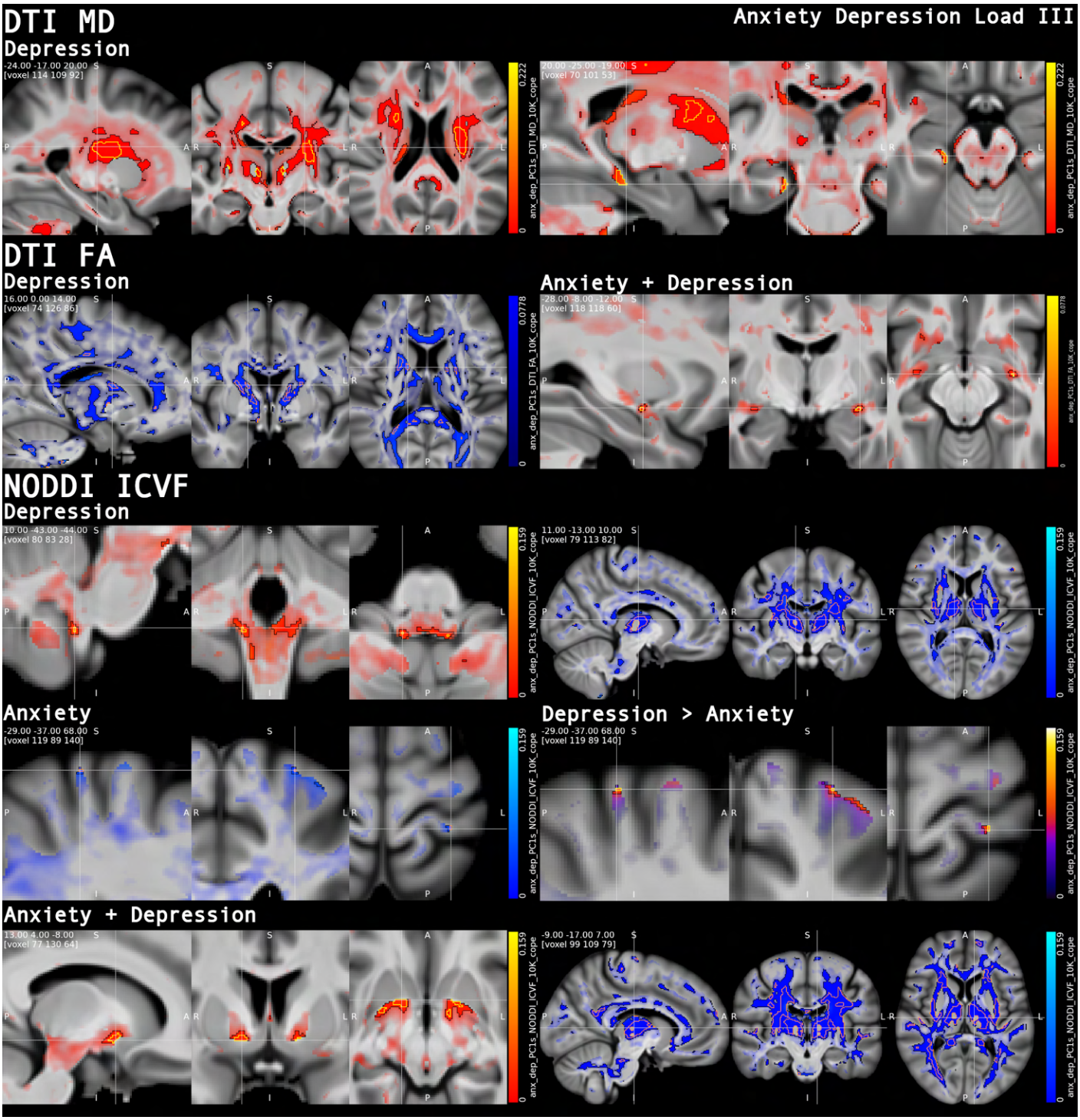


***Figure 8.3. Anxiety and depressive symptom load: MD, FA and ICVF.*** *Depressive symptoms were associated with a widespread pattern of increased mean diffusivity (MD) and decreased fractional anisotropy (FA) and neurite density (ICVF) across cortico-striatal, thalamic and fronto-parietal white matter, consistent with reduced microstructural integrity. In contrast, anxiety-related effects were more spatially circumscribed, including a focal decrease in ICVF at the WM/GM boundary of postcentral cortex, highlighting more localized microstructural alterations. Additive effects of anxiety and depressive symptoms were found in increased FA in anterior commissure adjacent to amygdala and increased ICVF in white matter superior to the substantia innominata. (See Fig. 8.1. for visualization conventions.)*

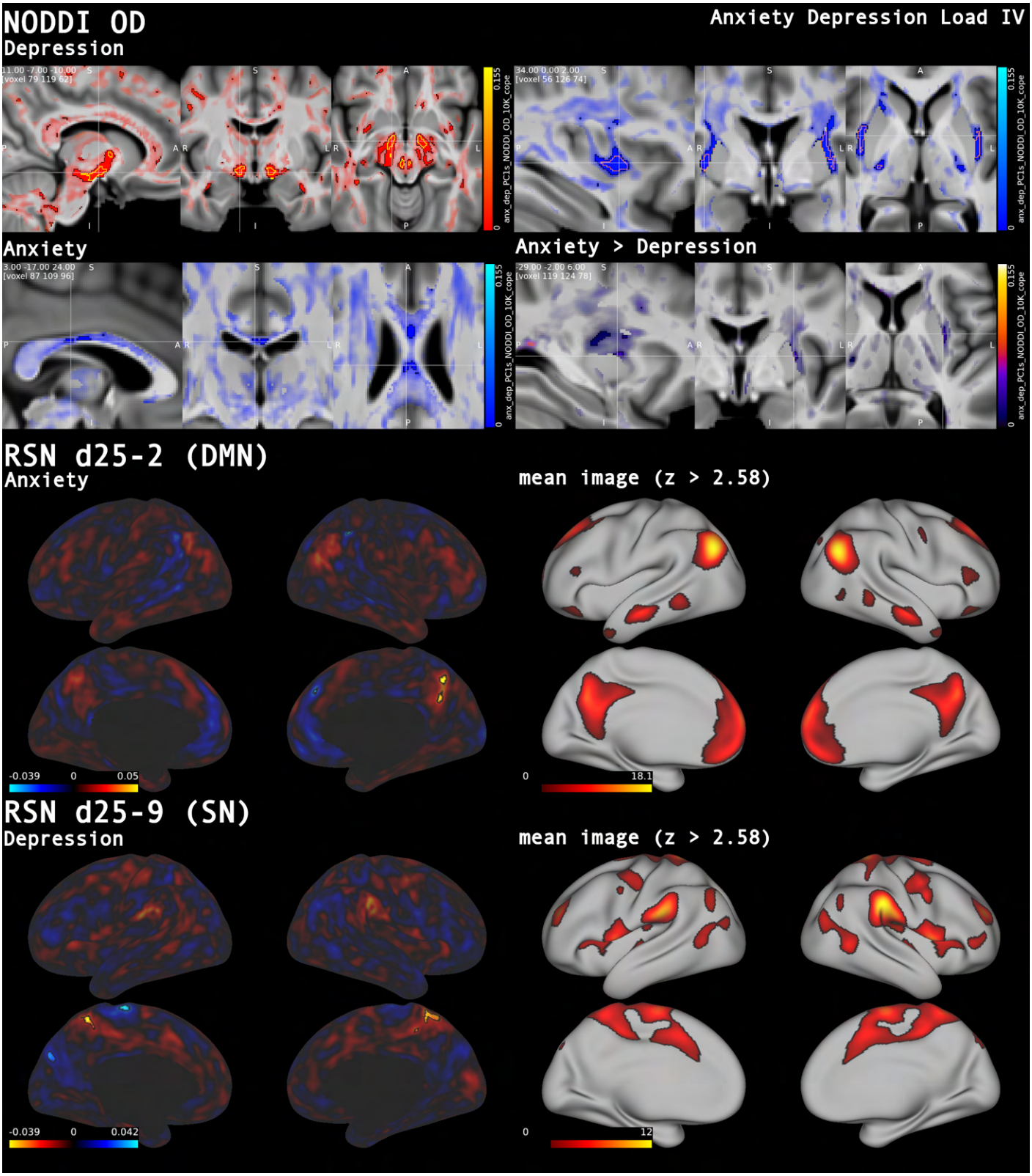


***Figure 8.4. Anxiety and depressive symptom load: OD and RSN.*** *Orientation dispersion (OD) was increased in bilateral hypothalamus for depressive symptoms, consistent with microstructural reorganization, and decreased in putaminal white matter, while anxiety showed additional OD reductions in callosal white matter. Resting-state analyses further revealed that anxiety symptom load was associated with reduced coupling of the default mode network (RSN d25-2) in posterior cingulate/precuneus, whereas depressive symptoms were linked to increased precuneus coupling and reduced coupling of the left paracentral lobule within a salience-like network (RSN d25-9)***.*** *(See Fig. 8.1. for visualization conventions.)*

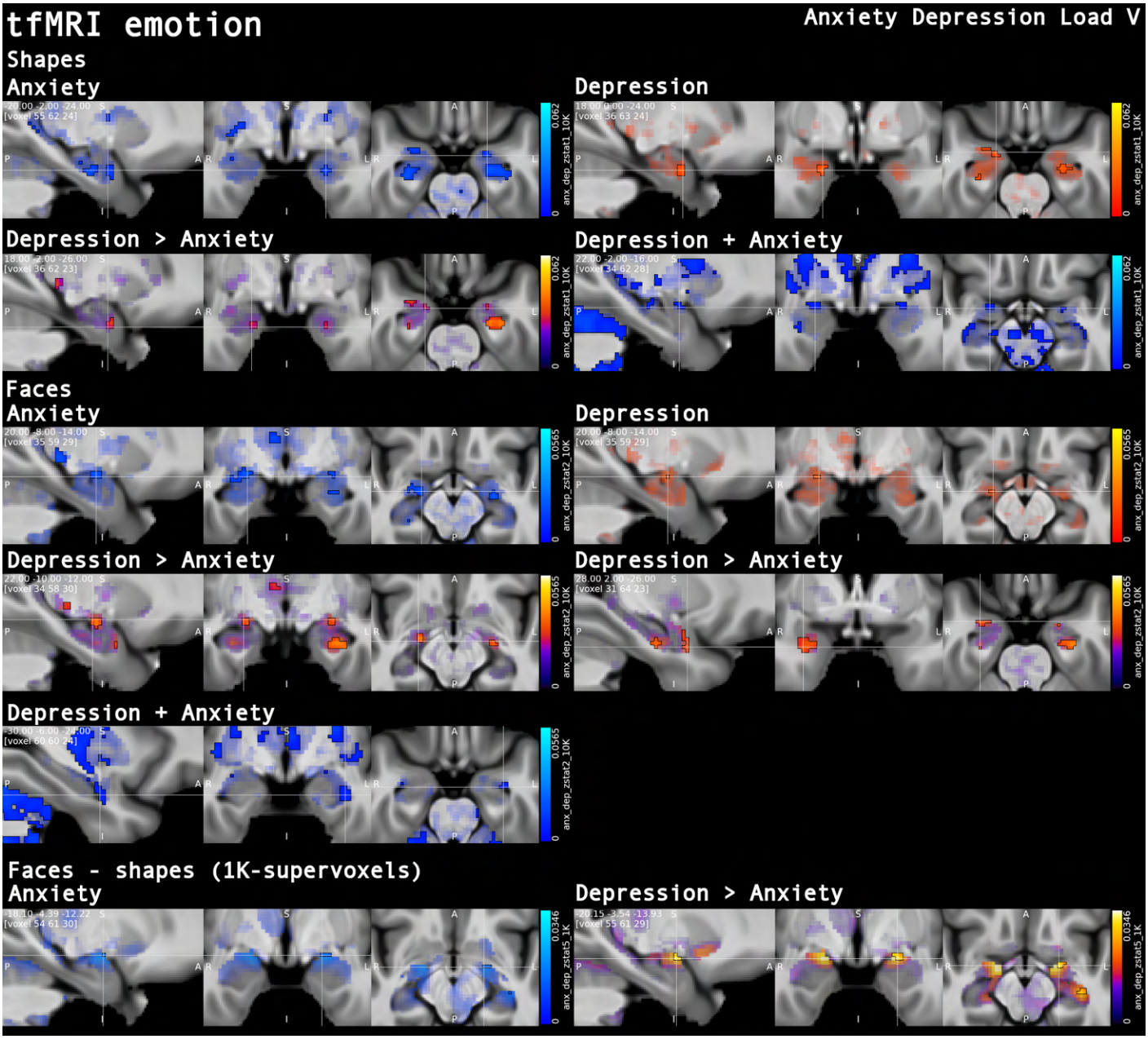


***Figure 8.5. Anxiety and depressive symptom load: Revisiting amygdala reactivity to negative faces.*** *Anxiety and depressive symptoms were associated to spatially and directionally distinct patterns of amygdala responses to neutral shapes and negative faces. While anxiety symptom load generally decreased amygdala reactivity, depressive symptoms exhibited an opposite relationship. Using the more sensitive 1K-supervoxels, a relation to faces above shapes for depression over anxiety was detected only when using the more sensitive 1K-supervoxels. (See Fig. 8.1. for visualization conventions.)*

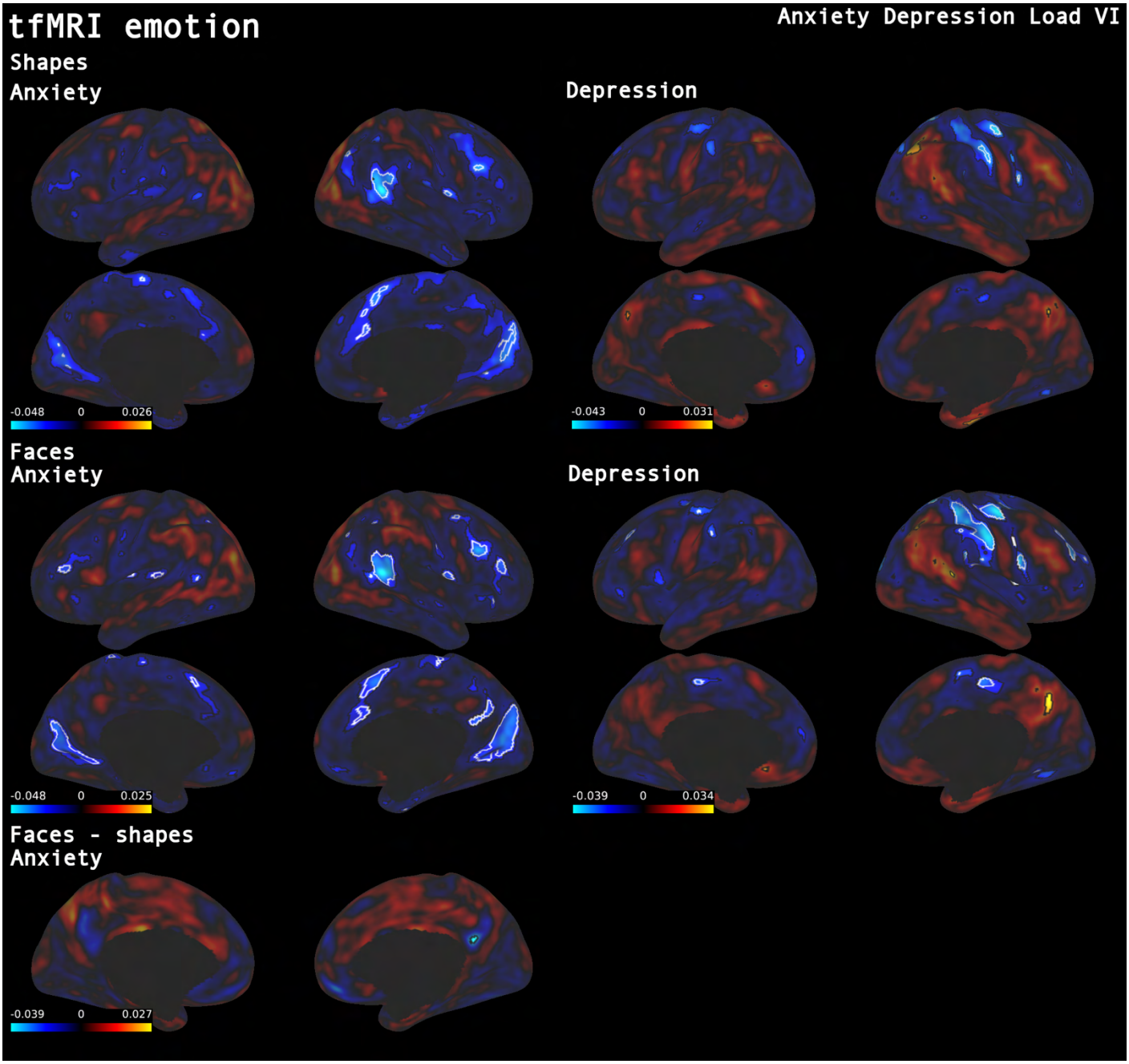


***Figure 8.6. Anxiety and depressive symptom load: Emotion task (surface).*** *Consistent with the decreased amygdala activation, anxiety symptoms related to decreased cortical activity in salience related regions as well as dlPFC. Depressive symptoms related to decreased somatomotor activation and increased activity in the precuneus. The faces – shapes contrast exhibited decreased activation of posterior ACC for anxiety symptoms only. Interestingly, pACC has been recently shown to encode face familiarity (Afzalian & Rajimehr, 2021). (See Fig. 8.1. for visualization conventions.)*

**NODDI ICVF:** Strong evidence was found for reduced ICVF for anxiety in a small cluster at the white matter (WM)/ gray matter (GM) boundary of postcentral gyrus. No positive association was found. For depression we found increased ICVF in the posterior medulla oblongata, and decreased signal in bilateral thalamus and fronto-parietal white matter.

**NODDI OD:** Anxiety showed moderate evidence of decreased orientation dispersion in the corpus callosum. There were no significant areas with positive association.

Depressive symptoms exhibited strong evidence of positive association with bilateral hypothalamus and distributed patches along subcortical and cortical WM/GM boundaries, as well as negative association with bilateral external and internal capsule.

**DTI MD:** Anxiety exhibited weak evidence for positive association in a small white matter cluster above the left calcarine sulcus, while depression showed strong evidence for positive association with increased MD in cortico-striatal and parietal white matter, and bilateral thalamus.

**DTI FA:** Moderate evidence for increased signal for anxiety was seen at the cortex/white matter boundary next to the left callosal sulcus. There was strong evidence for a negative association of depression with FA in bilateral internal capsule and disseminated supra- and infratentorial white matter tracts.

**RSN d25-2 (DMN):** Anxiety symptom load exhibited moderate evidence of increased coupling of right precuneus within the default mode network with significant decoupling of right dmPFC. We found no association for depressive symptom load.

**RSN d25-9 (SN):** Depressive symptom load exhibited strong evidence for increased coupling of left (and moderate evidence for contralateral) precuneus within the salience-like RSN d25-9 network. Moderate evidence was further found for decoupling with depression in the border region of left premotor and motor cortex (M1), as well as left cuneus.

**tfMRI zstat (shapes):** Anxiety exhibited strong evidence for decreased activation in response to neural shapes in right temporo-parietal junction, angular gyrus, dmPFC, dlPFC, right frontoparietal operculum, left anterior hippocampus, left fusiform cortex, left premotor/motor cortex, and bilateral cuneus directly posterior to parieto-occipital fissure. Depression was negatively associated (strong evidence) with blood-oxygenation-level-dependent (BOLD) response in right pre- and postcentral gyrus and superior parietal lobule; bilateral caudate nucleus, left putamen, and cerebellum with strong support for activation in left VIIIa being lower than for anxiety load.

Combined anxiety and depressive load exhibited additional strong evidence decreases in bilateral red nuclei and right substantia nigra and paraventricular thalamic region, bilateral insula, as well as more extensive striatal, cortical (more clearly involving, e.g., supplementary motor area (SMA) and ACC) and cerebellar deactivation.

**tfMRI zstat (faces):** Bold response to faces was similar than for shapes. Anxiety again exhibited strong evidence for decreased activity in right temporo-parietal junction, dm-/dlPFC, right frontoparietal operculum, and bilateral cuneus. Strong evidence was, moreover, seen for decreased activation in right precuneus and bilateral lingual gyrus and right LGN and pulvinar. Depressive symptom load was associated with strong evidence with decreased activation in right pre- and postcentral gyrus and right SMA; bilateral caudate nucleus and cerebellum. Strong support was seen for additional negative associations with combined depressive and anxiety load in left superior colliculus bordering on periaqueductal gray (PAG), paraventricular thalamic area, left red nucleus, bilateral insula, bilateral cingulate cortex and SMA, and again overall more extensive deactivation across cortex, striatum and cerebellum.

**tfMRI zstat (faces − shapes):** No moderate or strong evidence effects were found in the faces – shapes contrast. A significant decrease was seen for anxiety in right precuneus, which was also, together with small regions in right mPFC and supramarginal gyrus, significantly lower in comparison with depression.

### 3.3.3 Experiment 3: broad effects of nicotine, alcohol and coffee on brain structure and function

Strong evidence was found for substance-related brain differences across all 13 tested sub-modalities (Figs. 9.1–9.12), with both main effects and direct contrasts highlighting distinct spatial signatures of past tobacco use, alcohol intake frequency, and coffee consumption.

**VBM:**

**Smoking:** Strong evidence was found for positive association in bilateral dorsolateral pulvinar (peak left hemisphere; $-\log_{10}(p)$_mapFDR > 10). Bordering voxels in ventricles were also found to be significant, which may fit with a shift in gray matter boundaries. Further areas of strong evidence were found in left ventromedial and dorsomedial PFC, right dlPFC, corpus callosum (presumably related to white matter decrease), right hippocampus (mid-anterior), bilateral parahippocampal gyrus, left paracentral lobule, visual cortex (V1/V2) and cerebellum (I-IV). In contrasting against coffee, vm-/dmPFC volume stood out as being higher in smokers with strong evidence. There was further strong evidence for volume increase along calcarine sulcus (V1) for smoking in contrast to alcohol and coffee consumption.

Volume loss associated with smoking was extensive covering infra-/ and supratentorial gray matter and subcortex with robust evidence ($-\log_{10}(p)$_mapFDR > 15) found across bilateral cingulate cortex, striatum and basal forebrain.

**Coffee:** Strongest evidence ($-\log_{10}(p)$_mapFDR > 15) was found for increased volume in bilateral nucleus accumbens region, substantia innominata, BNST, hypothalamus, ventral tegmental area (VTA) and encompassing the complete PAG. We found further strong evidence for increased gray matter signal in centromedial amygdala and amygdalo-striatal transition area, corpus callosum, right cerebral peduncle bordering on lateral substantia nigra. Strong evidence was found for extensive cerebellar volume increase (I-VI, VIII, IX, X; vermis). Moderate evidence was found for increase bilateral anterior hippocampus volume.

Strong evidence for higher subcortical volumes (striatum, amygdala, thalamus, VTA, PAG) as well as cerebellum was found for coffee consumption contrasting both smoking and alcohol consumption. Higher volume was further found in ACC.

While far less extensive than for smoking, coffee consumption was associated with decreased volume across frontal and parieto-occipital lobe. Some areas of strongest evidence ($-\log_{10}(p)$_mapFDR > 5) were bilateral straight gyrus, right ventrolateral prefrontal cortex (vlPFC), left dlPFC, bilateral precentral gyrus, and lateral occipital gyrus.

**Alcohol:** Strong evidence associations were found for right dmPFC, right anterior insula and frontal operculum, corpus callosum and fornix (to be interpreted as white matter loss), right basolateral amygdala extending into uncus and entorhinal cortex, right anterior hippocampus, bilateral parahippocampal cortex, dorsal pulvinar, right parietal operculum, paracentral lobule and precuneus, and temporo-occipital fusiform cortices extending into neighboring cerebellum. Contrasting coffee consumption, strong evidence for higher volume was solely found in bilateral mPFC, bilateral dorsal thalamus / ventricle region and a small region in lingual gyrus. Contrasting against smoking highlighted higher volume in bilateral substantia innominata, and subcallosal area.

Similar to smoking, alcohol consumption revealed extensive strong evidence associations with volume loss across the brain. The pattern differed with most robust evidence ($-\log_{10}(p)$_mapFDR > 20) not only for striatum but also in bilateral precentral gyrus, lateral amygdala, hippocampus, hypothalamus and thalamus.

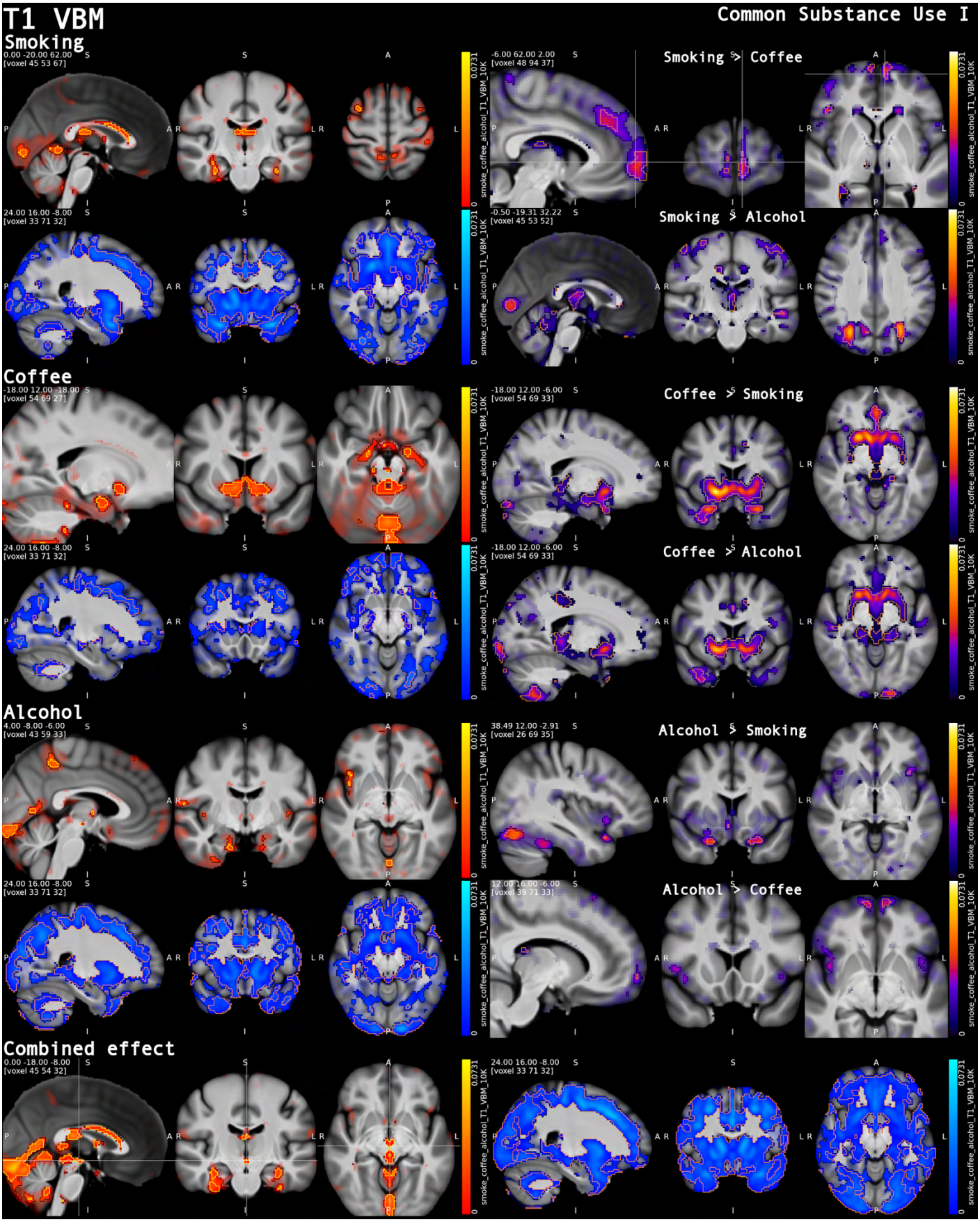


***Figure 9.1. Common substance use:*** *VBM. Extensive volume reductions were seen in association with alcohol, followed by smoking and to a lesser extent for coffee. Strong evidence was also found for localized and substance-dependent effects such as higher nucleus accumbens volume for coffee or anterior insula for alcohol. Common*

*visualization conventions (Figs. 9.1–9.12): β-maps thresholded at p_hFDR < 0.05 (black outline) overlaid on non-significant effects modulated by Z-statistic (surface views: non-significant effects shown by transparency, without Z-modulation), over the mean T1-weighted image. Positive associations are shown in red and negative associations in blue, contrast associations are displayed with a heatmap (NIH-fire); p_hFDR < 0.001 is outlined in yellow (positive and contrasts) or orange (negative), except on surface renderings, where p_hFDR < 0.001 is indicated in white. Group-mean resting-state network maps (Z-statistics) are thresholded at Z > 2.58 (approx. p < 0.01, two-tailed).*

**SWI QSM:**

**Smoking:** Evidence was most definitive in bilateral putamen ($-\log_{10}(p)$_mapFDR > 50), followed by caudate nuclei and the area in between substantia nigra, red nucleus and VTA (> 20). Further strong evidence associations were found in anterior hippocampi, entorhinal cortices, thalamus, habenulae, and supra- and infratentorial sulci, in particular, along cingulate sulcus.

In direct comparisons, QSM was higher for smoking than for coffee consumption in dorsal striatum and for coffee and alcohol consumption medial substantia nigra.

Strong evidence was found for decreases in QSM in white matter associated with smoking, in particular, in fronto-temporal lobes but with highest evidence in capsula interna and externa. A further area of very strong evidence for QSM increase was the bilateral centromedian nucleus (CN) of the thalamus.

Contrast analysis revealed the white matter QSM to be higher in smoking than coffee but not alcohol consumption.

**Coffee:** Similar to smoking but to a lesser extent coffee consumption showed strong evidence for increased QSM in the striatum with most robust evidence, however, for the caudate nucleus ($-\log_{10}(p)$_mapFDR > 20). and genu of capsula interna (consistent with myelin decrease), while peak evidence was found in the right habenula (> 35; > 20 for left habenula). Further areas of strong evidence included bilateral cingulate sulci, medial substantia nigra, left habenula, superior temporal sulcus, left Heschl's gyrus, and scatter parieto-occipital areas. Marked associations were further observed in bilateral cerebellum.

Negative associations were limited to internal capsule white matter and observed to a smaller degree than for smoking, which was also reflected in the direct contrast.

**Alcohol:** Alcohol exhibited a similar pattern of QSM increase across subcortex and sulci. Here most robust evidence was found for bilateral putamen ($-\log_{10}(p)$_mapFDR > 50), followed by caudate nucleus, and cerebellum, with further particularly significant areas (> 10) encompassing bilateral anterior hippocampi, superior temporal sulci, and lateral pulvinar nuclei. Similar to smoking, the area in between substantia nigra, VTA and red nucleus exhibited high QSM, consistent with increased myelinization.

Negative associations with QSM were similar to smoking and affected global white matter, in particular, internal and external capsulae and cerebellar as well as bilateral thalamic nuclei with highest evidence.

**SWI T2*:**

**Smoking:** T2* was positively associated with strong evidence in fronto-parietal white matter, aligning with dmPFC and pre- and postcentral gyri, occipital lobe white matter, as well as within anterior entorhinal cortices and white matter aligning with more posterior parts of entorhinal cortex.

Strongest evidence for T2* increase was, however, seen outside the brain, surrounding the frontal lobe ($-\log_{10}(p)$_mapFDR > 10). While this may be interpreted as a sign of frontal lobe atrophy, caution is warranted when interpreting extracranial signal changes.

In direct contrasts, T2* was higher for smoking with strong evidence in small clusters in pre- and postcentral cortex and left hippocampus (mid-anterior) than for coffee consumption. While contrasting against alcohol revealed higher signal in bilateral LGN (presumably related to negative association of alcohol below).

Congruent with evidence from QSM, strongest evidence for T2* decrease was seen in bilateral putamen. Other negatively associated areas with particularly high significance were seen in bilateral anterior commissure, caudate, along bilateral central sulcus of the insula, in cerebrospinal fluid (CSF) cranial to superior colliculi. We, moreover, found strong evidence for cortical T2* decrease across frontal operculum and cerebellum, as well as white matter associated decrease in mesencephalon.

**Coffee:** There were no voxels with strong evidence for T2* increase with coffee. Strongest evidence for T2* ($-\log_{10}(p)$_mapFDR > 10) decrease was seen in left anterior commissure, bilateral habenula and hypothalamus. Other strong evidence areas included bilateral striatum, pallidum, medial substantia nigra, superior colliculi and posterior horns of lateral ventricles.

**Alcohol:** Alcohol revealed the strongest evidence for associated T2* signal increase across the brain with most significant areas located in bilateral mPFC, middle temporal gyrus, right forceps major, as well as surrounding infra- and supratentorial brain, possibly atrophy-related. Further areas of strong evidence were found across frontal gray and white matter, temporal cortices, parieto-occipital gray and white matter, amygdalae, anterior hippocampi, anterior pons and medulla oblongata. Direct contrasting revealed the signal alterations to be stronger than for smoking and coffee in most regions.

Like for smoking, alcohol was most strongly associated with T2* decrease in striatum, with other very significant areas ($-\log_{10}(p)$_mapFDR > 10) found in bilateral LGN, bilateral fasciculus retroflexus, right habenula, bilateral pulvinar, white matter next to VTA, pons, and cerebellar white matter. Other areas of strong evidence included subthalamic nuclei, inferior temporal gyri, and cerebellar cortices.

**DTI MD:**

**Smoking:** Smoking exhibited strong evidence for globally increased MD across supra- and infratentorial white matter. Regions of strongest evidence ($-\log_{10}(p)$_mapFDR > 10) were seen in corpus callosum, bilateral corticospinal tract and superior thalamic radiations, aligned with right precentral gyrus, forceps major, and bilateral thalamus.

Direct contrasting showed MD to be higher than for coffee in most of the brain, while changes in corticospinal and thalamic tracts were higher than in alcohol.

**Coffee:** While lobar white matter appeared mostly unaffected, coffee consumption showed strong evidence for MD increase in the corpus callosum, aligning with cortical patches in dlPFC, pre- and postcentral cortices, in paraventricular thalamus, and in cerebellar white matter. There was no strong evidence of reductions in MD.

**Alcohol:** Similar to smoking, alcohol consumption was related to extensive increase of MD across the brain. The increase was, however, primarily located in frontal and occipital lobes and less spread out than for smoking. Particularly high evidence for MD increase was found in the corpus callosum and fornix ($-\log_{10}(p)$_mapFDR > 15), as well as along lateral ventricles (including temporal horns), third and fourth ventricles.

We further found strong evidence for decreased MD in bilateral cingulum, putamen, hypothalamus, right lateral amygdala, bilateral acoustic radiations and right Heschl's gyrus, anterior pulvinar, mesencephalon, pons, and cerebellar white matter.

**DTI FA:**

**Smoking:** Bilateral uncinate fascicle and putamen exhibited strongest evidence of increased FA for smoking ($-\log_{10}(p)$_mapFDR > 10). Other strong evidence areas included bilateral hypothalamus, red nucleus, left substantia nigra, bilateral precentral gyrus and postcentral gyrus, thalamus, and white matter aligned with left entorhinal cortex. Uncinate fascicle FA was higher for smoking than coffee or alcohol with strong evidence.

Reductions in FA were seen with strong evidence across all major white matter tracts, particularly

**Coffee:** Moderate evidence was seen for FA increase in mediodorsal thalamus (parvocellular part). While coffee consumption exhibited the least extensive reductions in FA, particularly strong evidence was found for reduction corpus callosum, bilateral fornix, and in between superior longitudinal fasciculi and cerebrospinal tracts.

**Alcohol:** Evidence was strongest ($-\log_{10}(p)$_mapFDR > 6) for alcohol-related FA increase along bilateral striatum, paraventricular thalamus, red nuclei, along cranial parts of PAG, left middle longitudinal fasciculus, parabrachial pons, and cerebellar white matter.

Complementary to MD findings, FA reduction exhibited strongest evidence for corpus callosum. Interestingly, this was also the case for the cingulum bundle, which was associated with decreased MD. Corpus callosum and cingulum exhibited strong evidence for FA reduction in direct comparison with coffee and smoking.

Further reductions were seen across major white matter tracts, albeit to a lesser extent than for smoking.

**DTI MO**

**Smoking:** Mode of anisotropy was positively related with smoking in internal capsule, bilateral uncinate fascicle, corticospinal tracts, superior longitudinal fasciculi, along pre- and postcentral cortices as well as bilateral dlPFC, and ventral posteromedial thalamus (VPM). Strongest evidence was found for genu of internal capsule and left uncinate fascicle ($-\log_{10}(p)$_mapFDR > 10).

Signal was decreased with strongest evidence (> 10) along dorsal superficial thalamic nucleus, bilateral putamen, cerebral pedunculus and right anterior commissure (temporal portion), and right claustrum. Further areas of strong evidence were found along cingulum bundles, corpus callosum, bilateral substantia innominata, and along internal surface of caudate and BNST.

**Coffee:** Strong evidence for positive association with DTI MO was found in anterior and posterior segments of corpus callosum, and bilateral mediodorsal thalamus. Strong negative evidence was also found in the corpus callosum as well as crus cerebri and posterior pons.

**Alcohol:** Areas with highest evidence for positive shift of anisotropy mode ($-\log_{10}(p)$_mapFDR > 10) were found in corpus callosum including forceps minor and major, internal capsule, frontal aslant tract, mediodorsal thalamus, lateral pulvinar, and cerebellar white matter. More regions with strong evidence were found in fiber tracts across the brain.

As for coffee, negative alteration in diffusion mode were also found for corpus callosum, here extending into cingulum bundles. Further areas with particularly strong evidence (> 10) were found in temporal portions of bilateral anterior commissure, right uncinate fascicle, and aligned with dorsal putamen and PAG. The negative association with the cingulum bundle was again shown to be specific to alcohol consumption in direct contrasts.

**NODDI ICVF:**

**Smoking:** Particularly strong evidence ($-\log_{10}(p)$_mapFDR > 10) was found for increased neurite density along putaminal surfaces, ventral BNST/substantia innominata area, bilateral subthalamic region and medial substantia nigra.

Negative association with ICVF was complimentary to findings in MD and FA with strong evidence for extensive reductions across supra- and tentorial white matter, exhibiting particularly robust evidence (> 10) in pre-, para- and postcentral white matter, cortico-spinal tract and internal capsule as well as bilateral thalamus. Most of these associations were stronger than for alcohol and coffee in direct comparison.

**Coffee:** Strongest evidence of neurite density increase ($-\log_{10}(p)$_mapFDR > 10) for coffee was found along left caudate, medial forebrain bundle, and in bilateral hypothalamus, followed by further areas of strong evidence in bilateral globus pallidus, along lateral amygdalae and amygdalo-striatal transition area, and in bilateral crus cerebri as well as cerebellar vermis. Strong evidence associations for decreased density were found in a left precentral cortex.

**Alcohol:** ICVF along putamen was increased with substantially strong evidence ($-\log_{10}(p)$_mapFDR > 10) across putamen, mid- and posterior corpus callosum, red nuclei, white matter adjacent to VTA, dorsal to locus coeruleus and in cerebellar white matter. Additional areas of strong evidence were found in bilateral pulvinar and anterior mediodorsal nuclei.

Negative associations with ICVF mirrored findings in FA and MD, with extensive regions of reduction in frontal and occipital lobes and particularly strong evidence for reductions in anterior corpus callosum and forceps minor but also along straight gyri and dmPFC.

**NODDI OD:**

**Smoking:** Evidence for increased orientation dispersion was highest ($-\log_{10}(p)$_mapFDR > 10) in bihemispheric substantia nigra, around bilateral striatum and aligned with substantia innominata. Other areas of strong evidence included orbitofrontal fibers, the crossing of bilateral frontal aslant tract with superior longitudinal fasciculus, left cingulum bundle, white matter lateral to bihemispheric LGN (possibly stria terminalis), and fibers along left dlPFC, and bilateral pre- and postcentral cortices. Evidence was, moreover, strong for higher signal than alcohol in bilateral substantia nigra, and higher than coffee in the left nucleus.

Consistent with findings from other diffusion metrics, robust evidence was found for decrease in orientation dispersion of bilateral uncinate fascicle ($-\log_{10}(p)$_mapFDR > 20), also in direct comparison with coffee and alcohol consumption. Further areas of strong evidence were temporal portion of anterior commissure, fibers along entorhinal cortices, corpus callosum, anterior and superior thalamic radiations, corticospinal tracts, internal capsules, bilateral thalamus, superior longitudinal fascicles, and in proximity of bilateral locus coeruleus.

**Coffee:** Coffee consumption was also associated most robustly with OD in a slightly more medial region of substantia nigra ($-\log_{10}(p)$_mapFDR > 8). Further regions of strong evidence included callosal fibers, fibers lateral of cingulum bundle, internal capsule bordering on nucleus accumbens, anterior commissure, bilateral fornix, fibers along pre- and postcentral cortices, and along bilateral longitudinal white matter tracts.

Strong evidence for OD decrease was found in bilateral thalamus (centromedian / mediodorsal).

**Alcohol:** OD increase with alcohol was most strongly supported ($-\log_{10}(p)$_mapFDR > 10) for bilateral internal capsule along caudate nucleus, corpus callosum, cingulum bundle, along lateral putaminal surfaces, fornix and anterior commissure, left pre- and postcentral cortex, in a longitudinal bundle crossing right corticospinal tract, right and mesencephalic white matter in between bilateral red nuclei and PAG. Further mostly longitudinal cerebral tracts as well as cerebellar white matter tracts were found to associate with alcohol with strong evidence.

Most robust evidence for OD decrease (> 10) was found in forceps minor and apical of forceps major, frontal aslant tract (FAT), paraventricular hypothalamus, amygdalo-striatal transition area, right superior PAG, posterior pons along locus coeruleus region, and cerebellar white matter. Further areas of strong evidence were mostly found along longitudinal association tracts but also in bilateral thalamus, left pallidum, and along entorhinal cortices.

**Warpfield Jacobian**:

**Smoking:** Strong evidence was found for local volume expansion in bilateral internal capsule surrounding and including lateral parts of caudate nucleus for smoking (note: higher values in warpfield Jacobian maps represent local contraction with respect to the MNI group template, i.e., the region was bigger before normalization), in between callosal sulci, bilateral dmPFC, parahippocampal gyrus, anterior insular cortex (bordering on central sulcus), left postcentral cortex, bilateral postcentral sulcus, right paracentral lobule,

posterior horns of lateral ventricles,  and cerebellum (VIII/IX and left I-IV). Insular expansion was also higher in direct comparison with alcohol and coffee.

Negative association analysis exhibited edge effects surrounding frontal and occipital lobes, which are probably atrophy related but should be interpreted with caution. However, clearly intracortical areas with volume contraction included bilateral vm-, dm-, and dlPFC  lateral orbitofrontal cortices, and parieto-occipital transition area. Further areas with strong evidence for contraction included corpus callosum (genu), basal forebrain area extending into anterior striatal regions and amygdalae, bilateral thalamus, mesencephalon, cerebellar peduncles and white matter, and medulla oblongata.

**Coffee:** Coffee consumption related with local expansion in fornix and anterior lateral ventricle region, right supplementary motor area (lateral part), transition from fornix to corpora mammillaria, left postcentral cortex and superior parietal lobule, bilateral region including posterior caudate and lateral ventricles, posterior horns of lateral ventricle, cerebellar peduncles and cerebellum (vermis, bilateral VIIIa, VIIb, X).

Coffee exhibited more restricted areas of contraction. These were limited to bilateral frontal and right fronto-parietal white matter, corpus callosum (genu) including ACC, bilateral pallidum extending into thalamus and posterior internal capsule, and right occipital white matter.

**Alcohol:** Alcohol exhibited strongest evidence ($-\log_{10}(p)$_mapFDR > 10) for expansion of anterior and posterior horns of lateral ventricles. The expanded region also included large parts of caudate nucleus. Further areas roughly corresponded to bilateral cingulate cortex and callosal sulcus, anterior hippocampus, entorhinal cortices, postcentral cortex, sulcus and superior parietal lobules, third ventricles, subarachnoid cisterns, and venous sinuses.

As for smoking, strongest evidence was found for edge effects, this time surrounding most of the brain, and likely atrophy-related. Cortical contraction was seen across frontal, parietal and occipital lobes, with temporal lobes being less affected, and in cerebellum. Furthermore, strong evidence was seen for contraction across subcortical areas, global white matter including corpus callosum, in mesencephalon and medulla oblongata.

Direct comparison revealed these global effects, to be stronger in alcohol than in smoking and evidently in comparison with coffee.

**RSN d25-2 (DMN):**

**Smoking / Coffee:** There were no strong evidence effects for smoking and coffee.

**Alcohol:** Evidence was strong for increased coupling of bilateral m-/ and dlPFC, orbitofrontal cortices, temporal poles, middle temporal gyri, left postcentral gyrus, right supramarginal gyrus, bilateral precuneus and superior parietal lobule; right mid-hippocampus, thalamus and cerebellum.

**RSN d25-6 (FPN-1):**

**Smoking:** No strong evidence alterations were found within the fronto-parietal component RSN d25-6.

**Coffee:** Strong evidence was found for decreased coupling in left temporo-parietal junction with RSN d25-6.

**Alcohol:** Strong evidence was found for increased coupling with alcohol in bilateral vlPFC, supramarginal gyri (and bordering on angular gyri), left middle temporal gyrus, bilateral precuneus and occipital gyri. Decreased coupling was strongly supported in left ACC, left mPFC, right vlPFC and frontal operculum, bilateral precuneus, and cerebellum.

**RSN d25-9 (SN):**

**Smoking:** Increased coupling of left precentral cortex within the salience-like RSN_d25_9 network was supported strongly for smoking.

**Coffee:** No strong evidence alterations were found.

**Alcohol:** Increased coupling of right precentral gyrus, SMA, parieto-frontal operculum, posterior section of bilateral middle temporal gyri, right superior parietal lobule and precuneus along parieto-occipital sulcus was strongly supported.

**RSN d25-11 (FPN-2):**

**Smoking:** Decreased coupling of left middle temporal gyrus was strongly supported in a second fronto-parietal network.

**Coffee:** No strong evidence alterations were found.

**Alcohol:** Coupling was increased most robustly in left dlPFC bordering on vlPFC ($-\log_{10}(p)$_mapFDR > 10). Other strong evidence areas included bilateral frontal pole, vl-/dlPFC, left vmPFC, bilateral anterior insula, right SMA, bilateral precuneus, left temporal cortices, bilateral angular gyrus, and occipital gyri; left putamen and bilateral cerebellum.

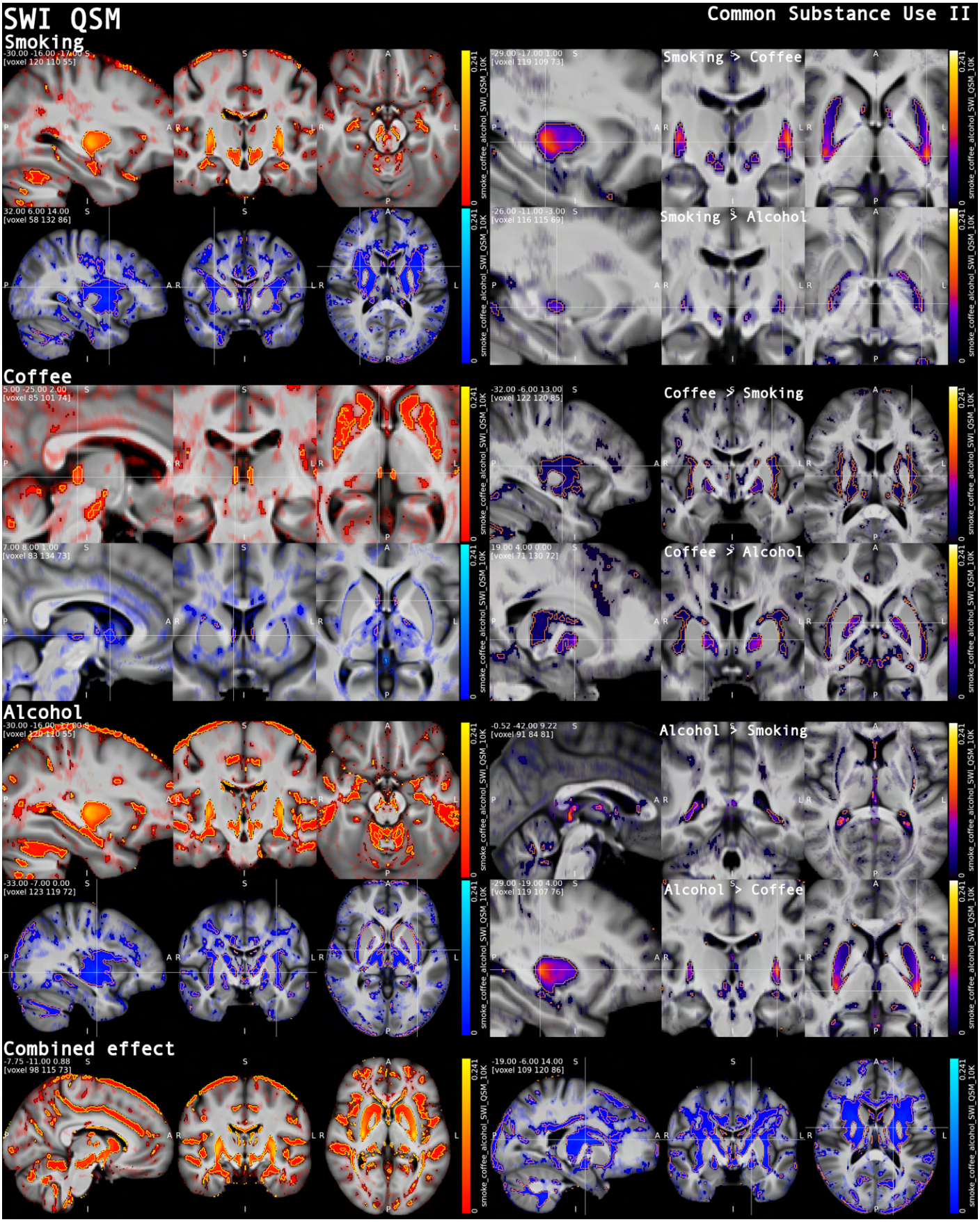


***Figure 9.2. Common substance use: QSM****. Smoking, alcohol and to a lesser extent coffee intake exhibited robust evidence for QSM signal increase in striatum and nigral pathways consistent with iron accumulation (peak for coffee in habenula). WM QSM, particularly, in internal and external capsule exhibited decrease. (Visualization see Fig. 9.1.)*

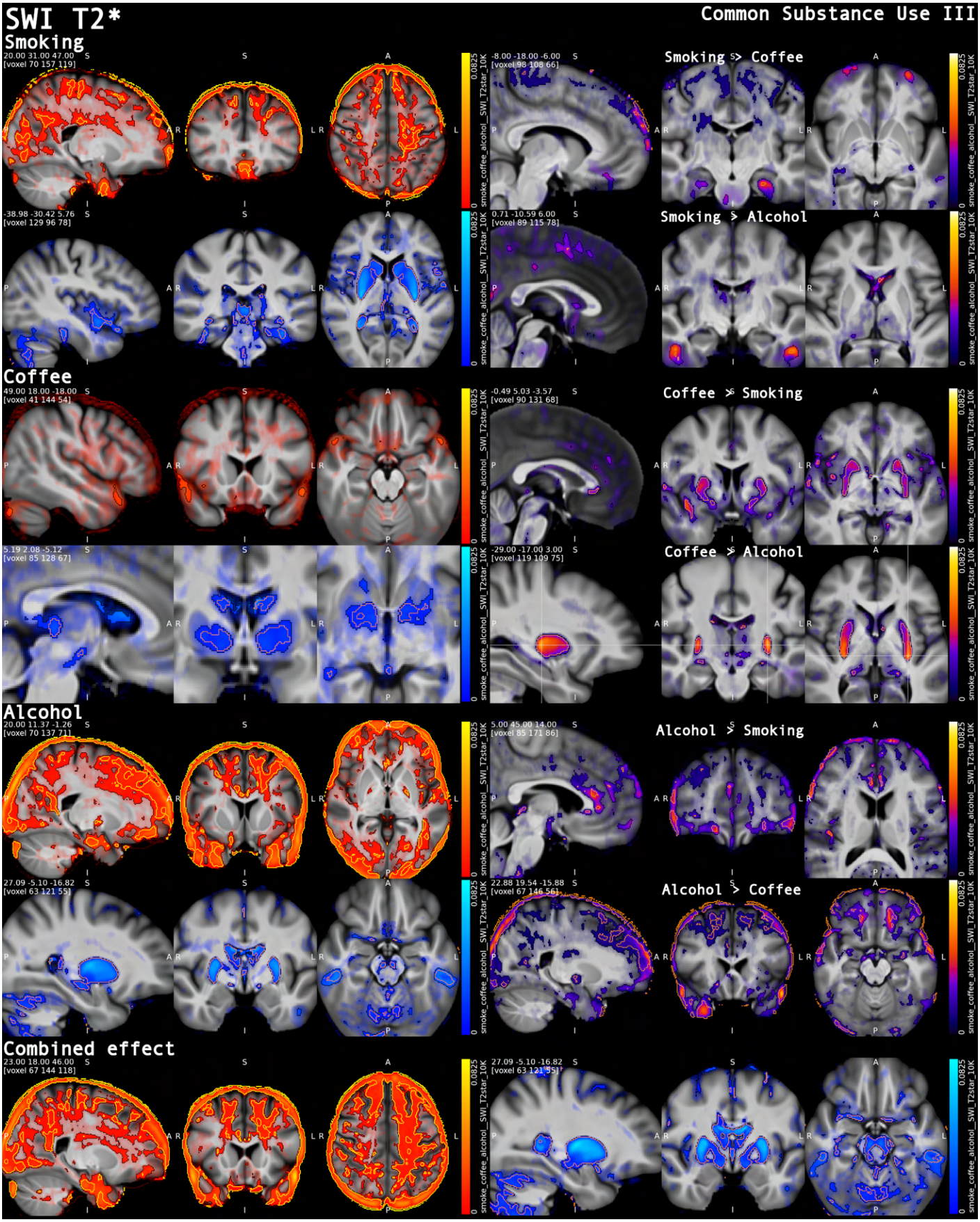


***Figure 9.3. Common substance use: T2****. Consistent with QSM and iron accumulation, T2* decreased with substance use in striatum. Alcohol and smoking showed global T2* elevations in WM and GM with distinct local propensities. As before, possibly atrophy-related edge effects should be interpreted with caution. (Vis. conv.: Fig. 9.1.)*

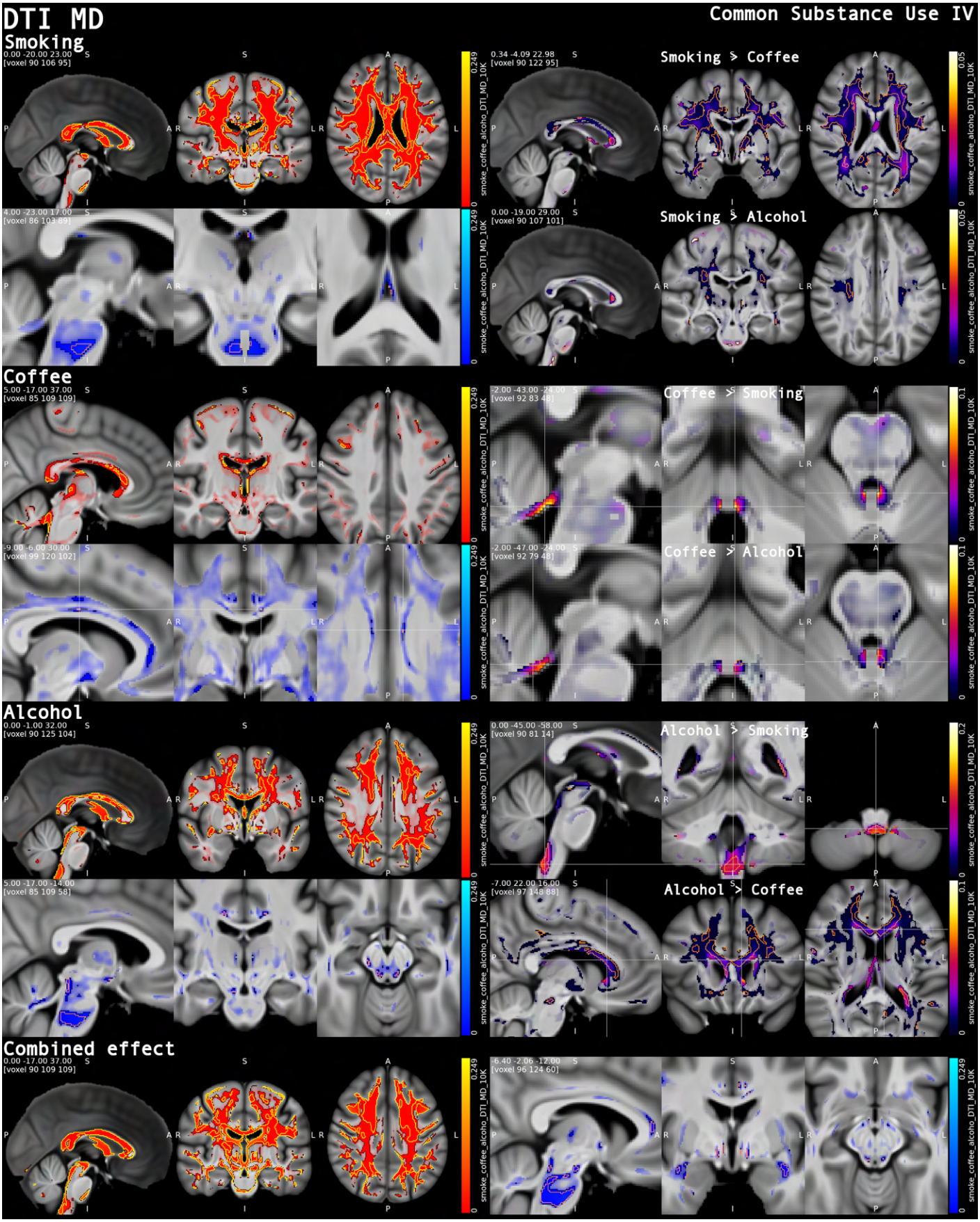


***Figure 9.4. Common substance use: DTI MD****. Global increase of mean diffusivity was seen for smoking, followed by alcohol. Effects for coffee were localized, e.g., in corpus callosum. Combined effect analysis highlighted decrease of MD in uncinate fascicles, adjacent to amygdalae, and periaqueductal gray (PAG). (Visualization convention: Fig. 9.1.)*

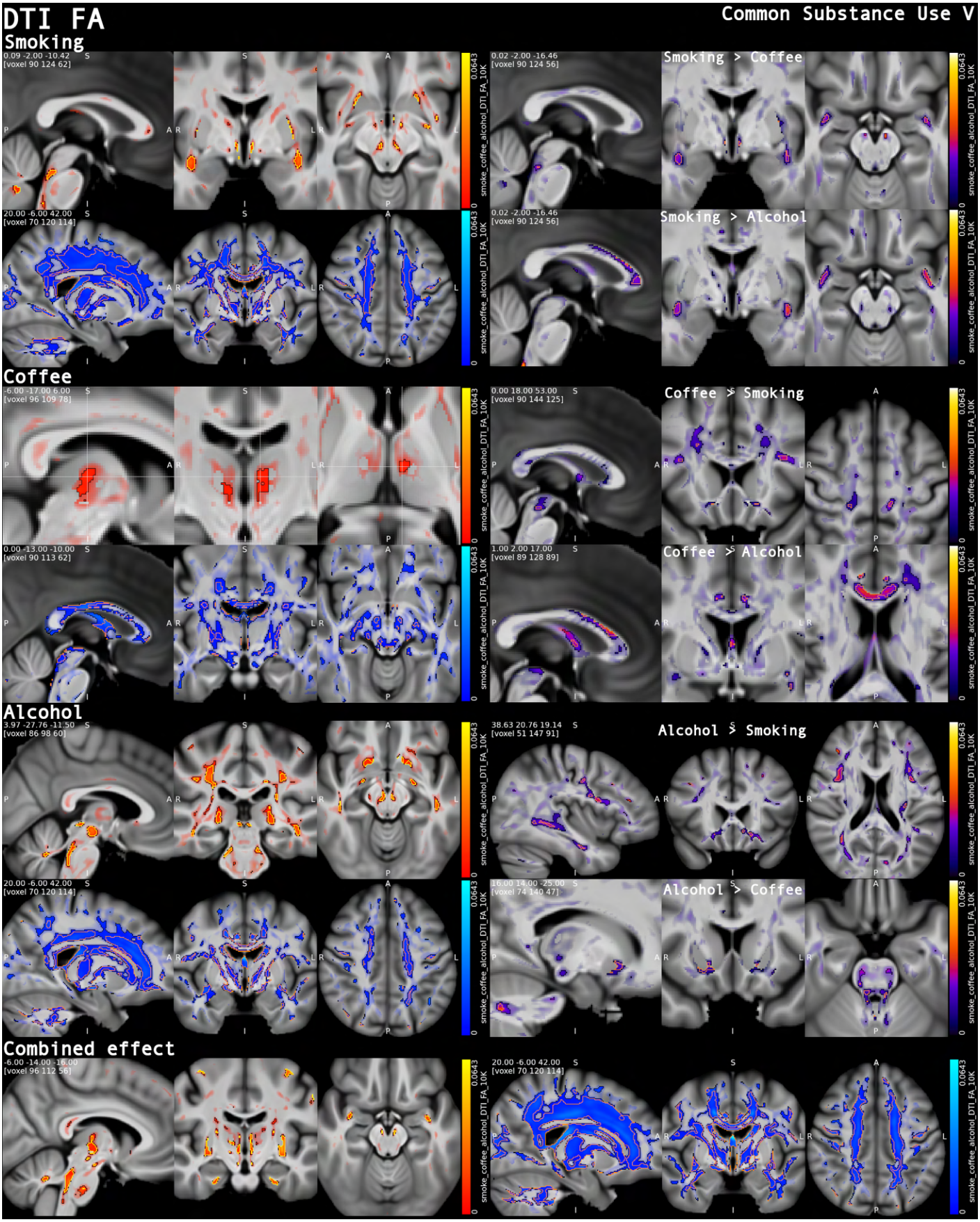


***Figure 9.5. Common substance use: DTI FA****. FA analysis confirmed widespread microstructural deterioration with nicotine and alcohol consumption, with again more limited effects for coffee. Uncinate fascicle FA was particularly increased for smoking as evidenced by direct contrast analyses. (Visualization convention: Fig. 9.1.)*

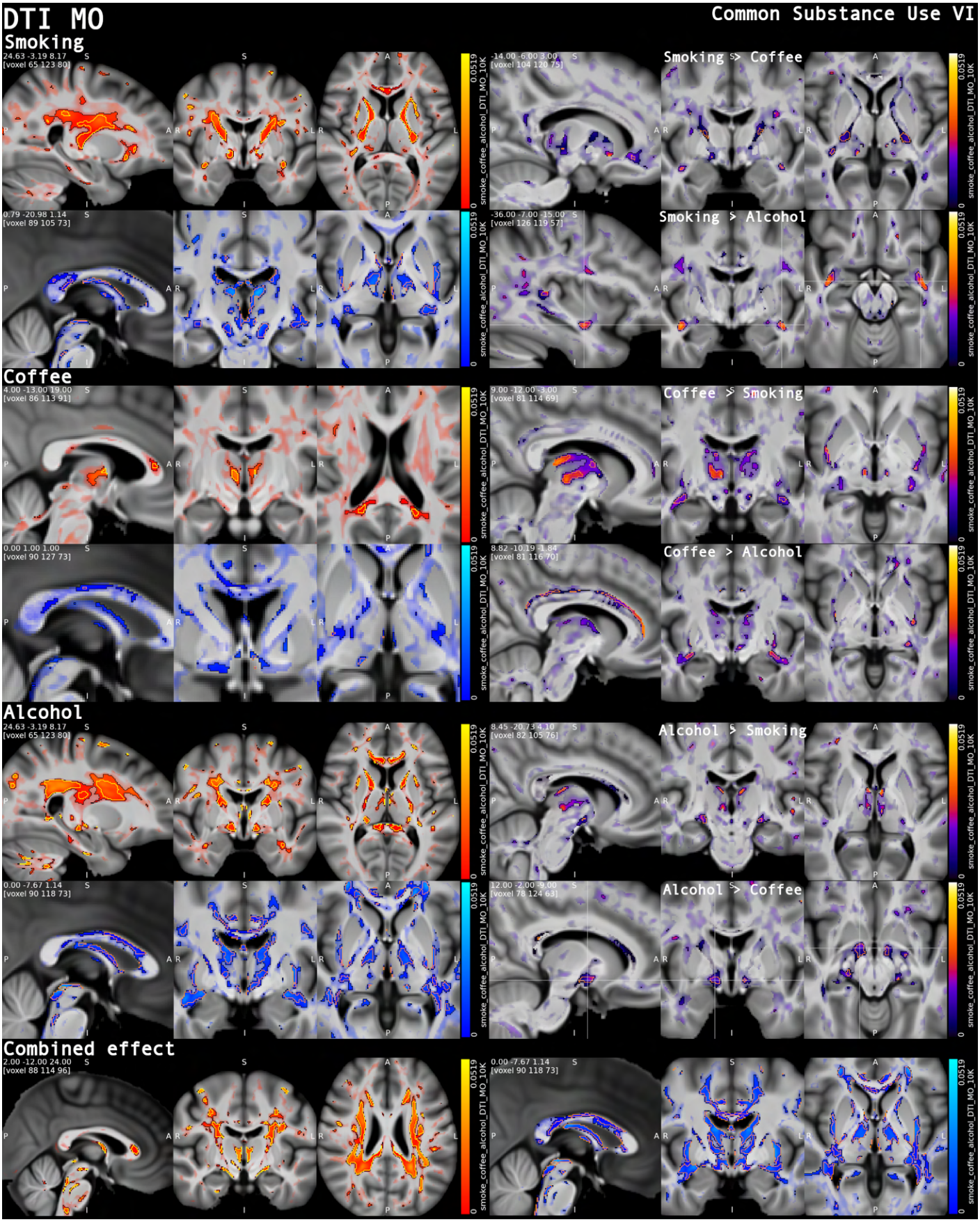


***Figure 9.6. Common substance use: DTI MO**. Alterations in mode of anisotropy (↑: prolate-shaped tensor, i.e., principal eigenvalue λ1 dominates over λ2 and λ3, ↓: oblate-shaped, λ1 ≈ λ2 ≫ λ3) were widespread for smoking and alcohol. Coffee was primarily related to changes in thalamus, callosum and anterior commissure. (Vis. conv.: Fig. 9.1.)*

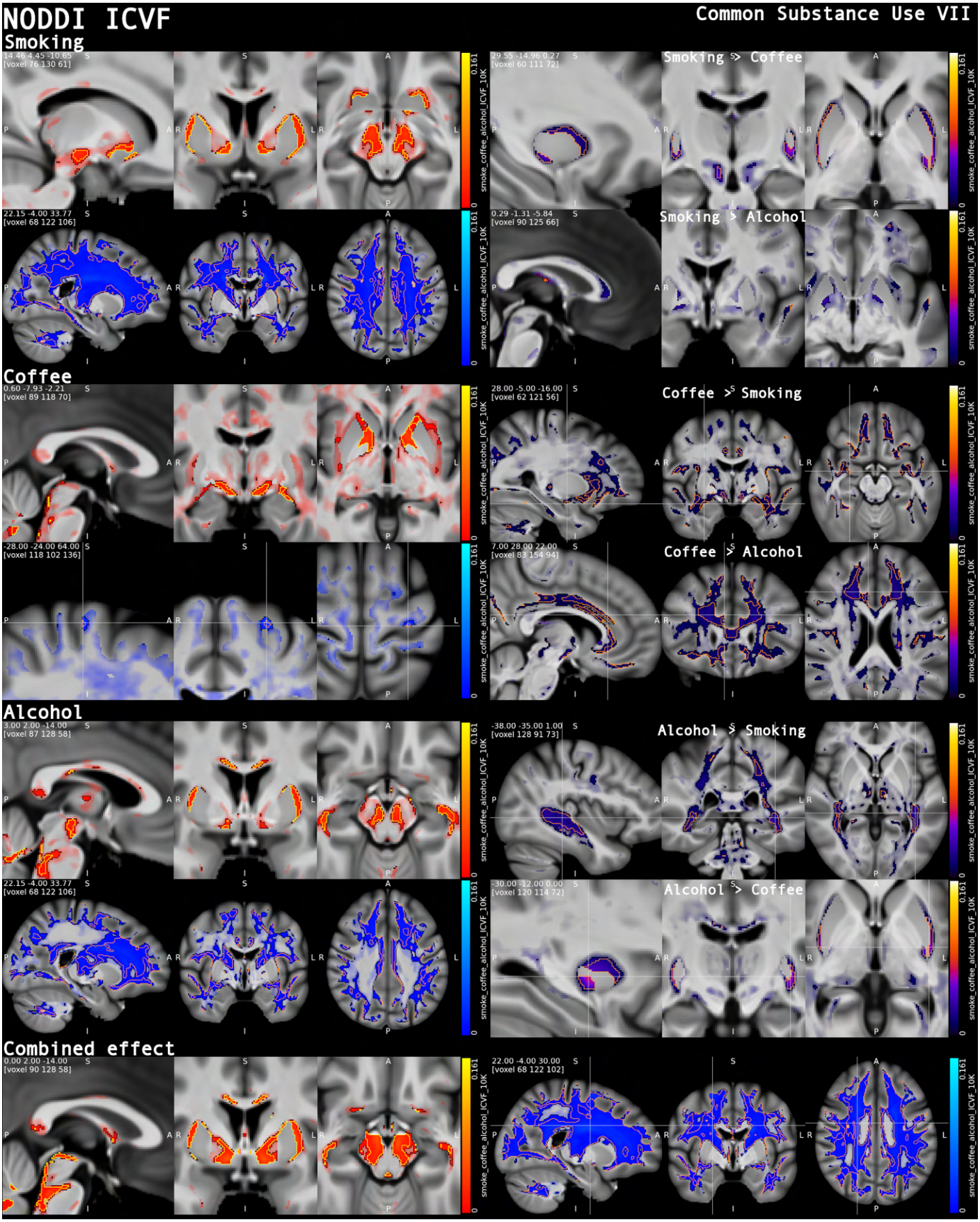


***Figure 9.7. Common substance use: NODDI ICVF****. Consistent with DTI findings, alcohol and smoking exhibited general patterns of reduced WM neurite density with associations with smoking being more extensive. Increases were primarily localized around putamen, in basal forebrain area and mesencephalon. (Visualization convention: Fig. 9.1.)*

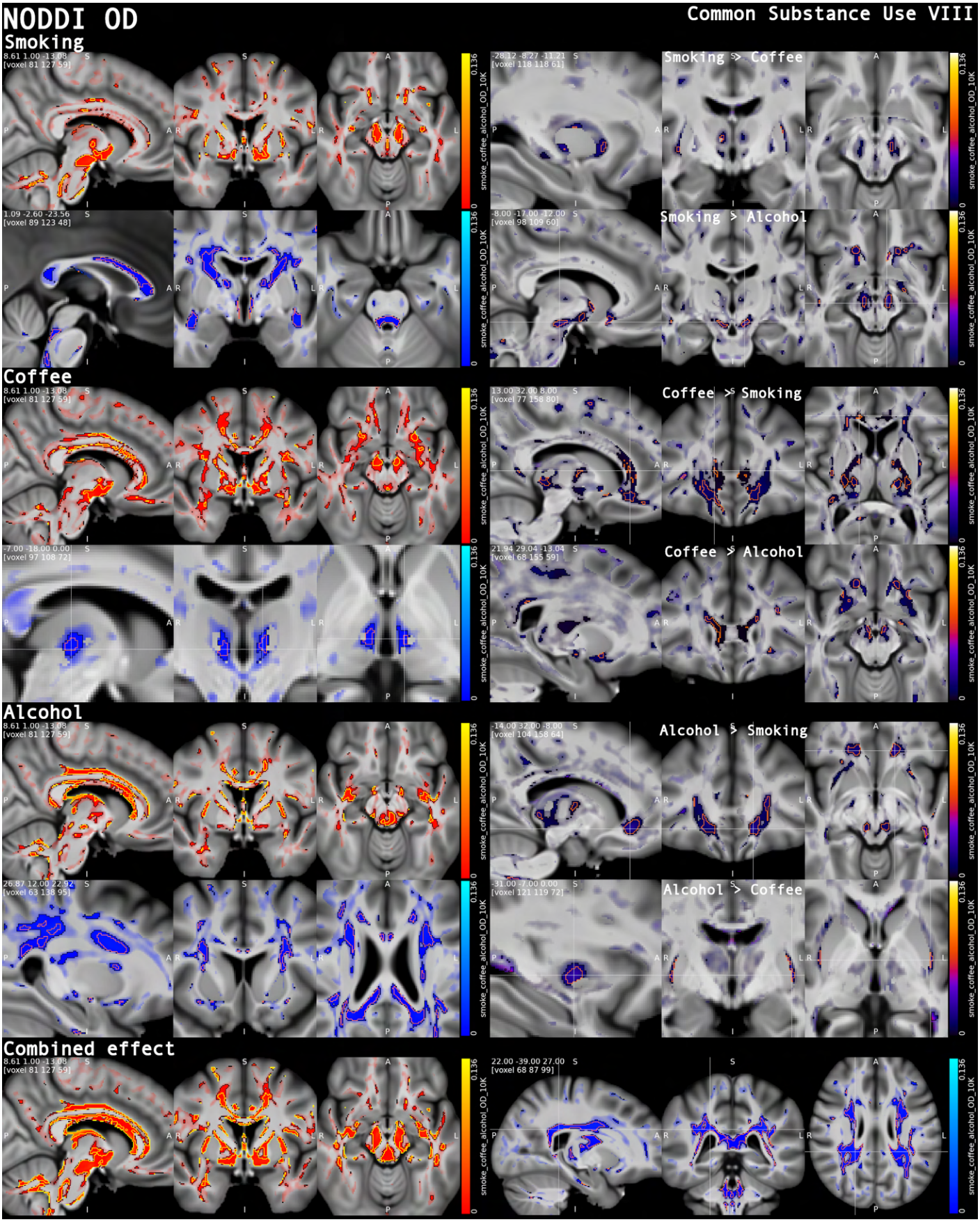


***Figure 9.8. Common substance use: NODDI OD***. *OD increases with were concentrated in nigrostriatal/basal-forebrain and major association pathways, whereas OD decreases were most consistent in uncinate fascicles (smoking) and in callosal/frontal and thalamic/brainstem regions (alcohol; thalamus for coffee). (Vis. conv.: Fig. 9.1.)*

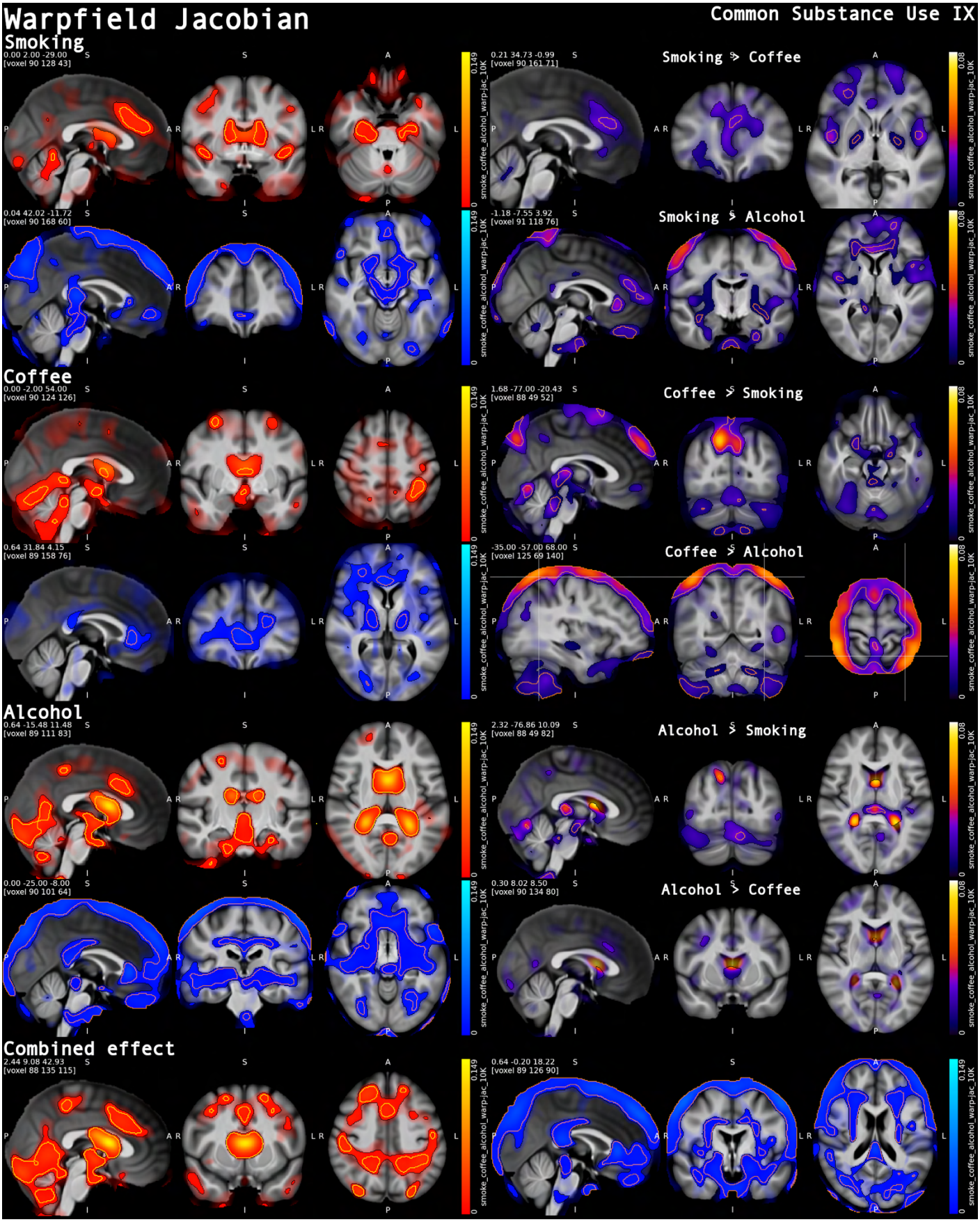


***Figure 9.9. Common substance use: warpfield Jacobian****. Smoking, alcohol and coffee were associated with distinct patterns of local volume expansion (+) and contraction (-). Alcohol, followed by smoking, related to extensive expansion of CSF space and contraction in WM and GM. Interpret edge effects with caution. (Vis. conv.: Fig. 9.1.)*

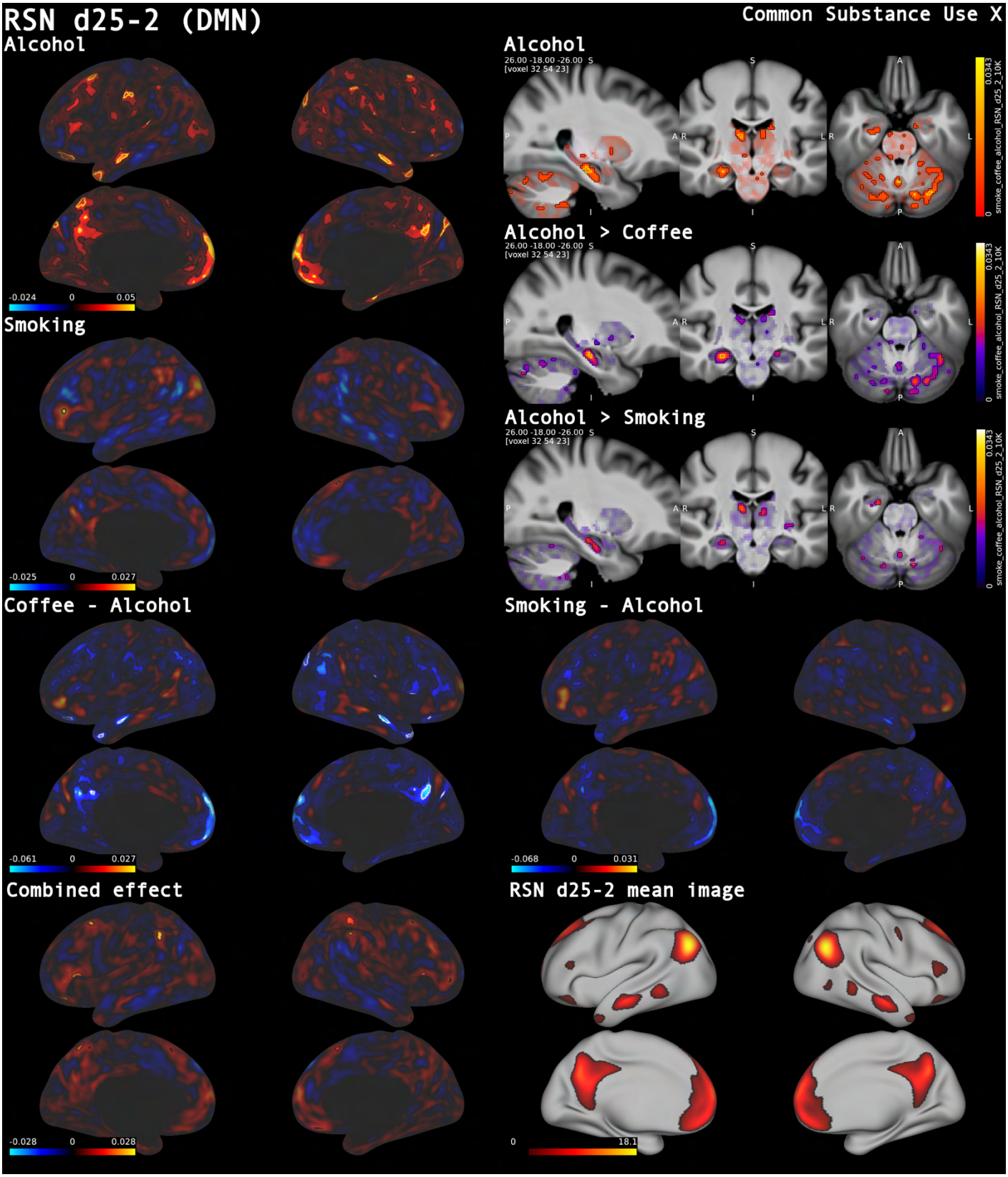


***Figure 9.10. Common substance use: RSN d25-2 (DMN).*** *Alcohol consumption was related to increased coupling in key regions of the default mode network but also in many distributed patches across cortex, consistent with dedifferentiation. Small regions in left dlPFC and right mPFC showed increases in smoking. Coffee intake did not alter connectivity in the default mode network. (Visualization convention: Fig. 9.1.)*

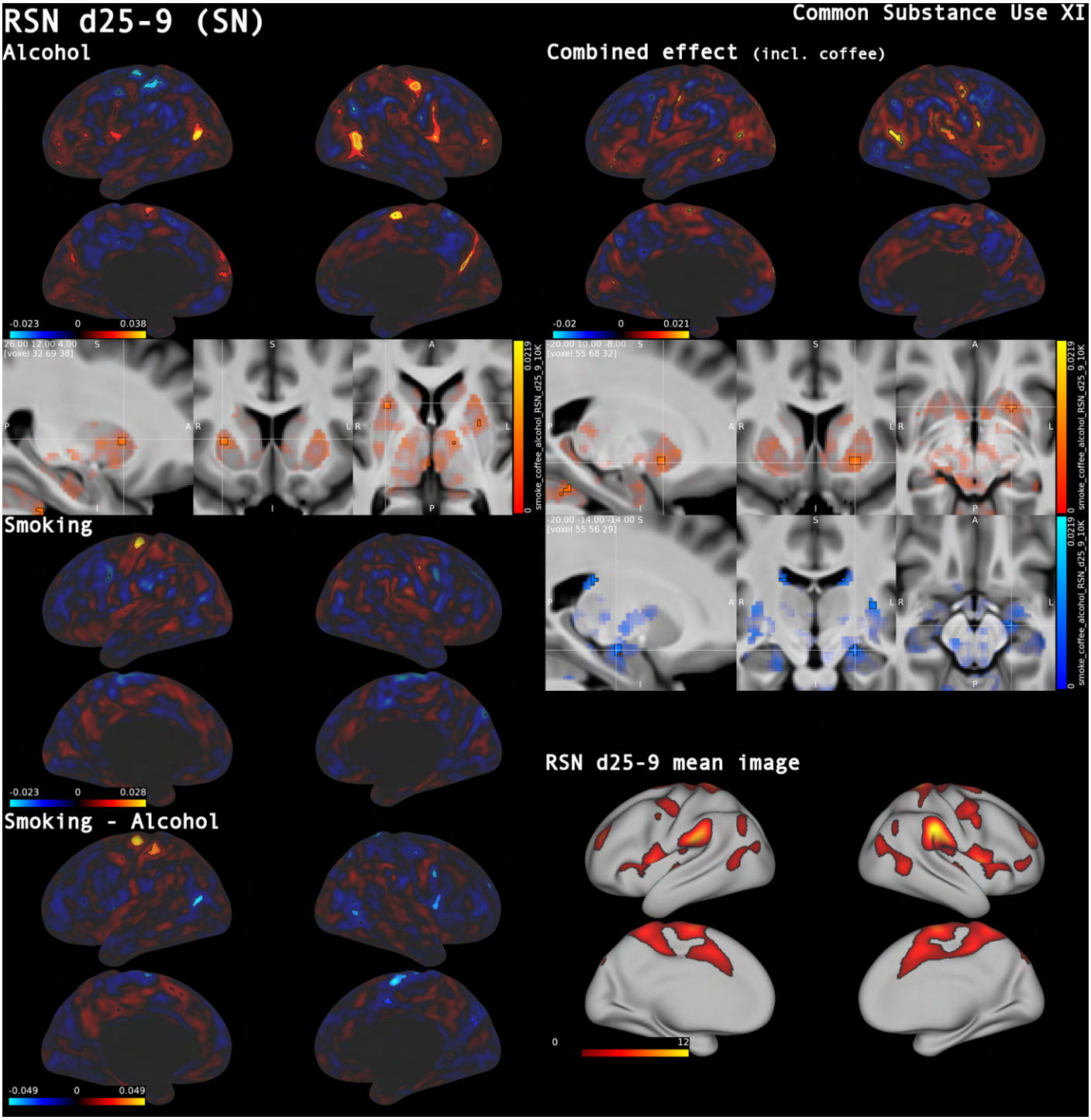


***Figure 9.11. Common substance use: RSN d25-9 (SN).*** *A salience-like network again exhibited more extensive alterations with alcohol including striatal recruitment (also seen as combined effect), while smoking was associated with increased coupling of left motor cortex. (Visualization convention: Fig. 9.1.)*

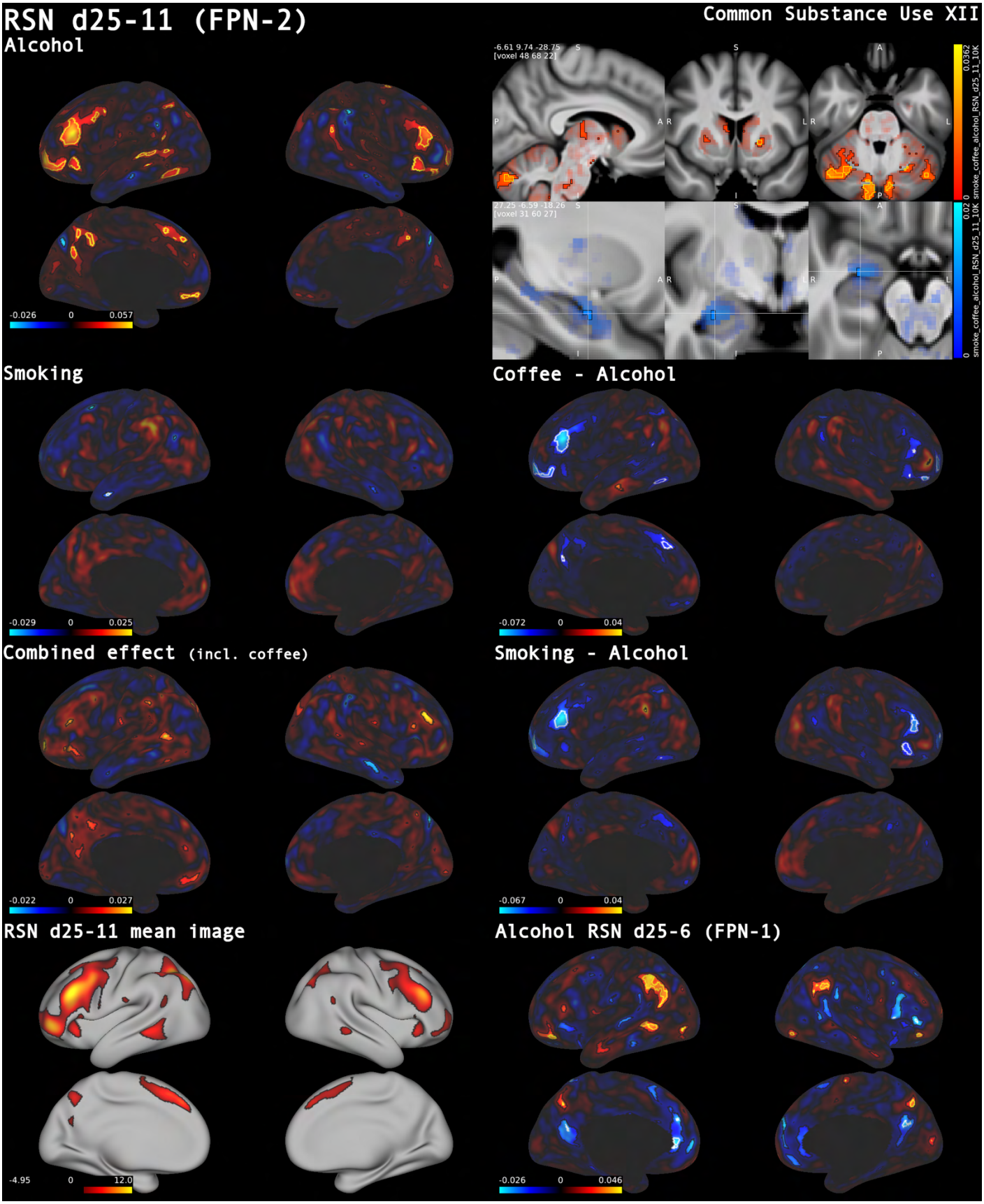


***Figure 9.12. Common substance use: RSN d25-11 (FPN-2).*** *Alcohol related with increased network coupling and added recruitment of cortical areas (e.g., vmPFC and superior temporal gyrus) and subcortex. A second fronto-parietal network (FPN-1) exhibited increased gain of positive and anti-correlated parts. (Vis. conv.: Fig. 9.1.)*

### 3.3.3 Experiment 4: *EPHA3* (rs987748)

Robust evidence was found for rs987748-associated effects across all tested sub-modalities (Figs. 10.1 – 10.5), showing distributed patterns across major white-matter pathways, alongside highly localized signals in the anterior commissure and further cortical/subcortical associations.

**VBM:**

The minor variant of rs987748 was most strongly associated with increased gray matter signal in midline anterior commissure and temporal anterior commissure / uncinate fascicle region. Volume increase was, moreover, seen with strong evidence across frontal, and most prominently parieto-occipital cortices. Areas with highest evidence were parietal operculum, left Heschl's gyrus (inferior limiting sulcus of insula), bilateral pulvinar, LGN, left cingulate sulcus, bilateral calcarine sulcus (V1), left angular gyrus, and occipital gyri. Other strong evidence areas included orbitofrontal cortices, anterior and posterior cingulate cortices, superior temporal cortices, bilateral LGN, supramarginal gyri, and cerebellum.

Volume decrease was seen most robustly for temporal lobes, specifically, in fusiform cortices and middle temporal gyri. Other strong evidence areas included bilateral anterior insula, amygdalo-striatal transition area, dorsal thalamus, right anterior hippocampus, PAG, bihemispheric lateral occipital cortex, and cerebellum (crus I/II, I-IV, VI).

**SWI QSM:**

QSM for the minor variant was most robustly increased in anterior commissure. Further areas with strong evidence for increase were found in left putaminal surface, bilateral superior temporal and fusiform cortices, right anterior hippocampus, right Heschl's gyrus, middle longitudinal fascicles, and occipital lobe white matter.

QSM decrease was seen with highest evidence in capsula interna (genu) and periventricular white matter, in between cingulum bundle and corticospinal tracts. Further areas of strong evidence included bilateral temporal pole, substantia innominata, centromedial amygdalae, bilateral putamen, dorsolateral thalamus, posterior corpus callosum, parieto-occipital and cerebellar white matter.

**SWI T2*:**

T2* exhibited strong evidence for positive relation with the minor variant in right pulvinar, bilateral middle longitudinal fascicle and straight sinus.

Strong evidence for T2* decrease was seen in right basal operculum, bilateral orbitofrontal cortices (medio-posterior), inferior temporal gyrus, fusiform gyrus with adjacent white matter, right middle temporal gyrus, amygdalo-striatal transition area, right posterior insula and Heschl's gyrus, bilateral optic radiation, lateral occipital gray and white matter.

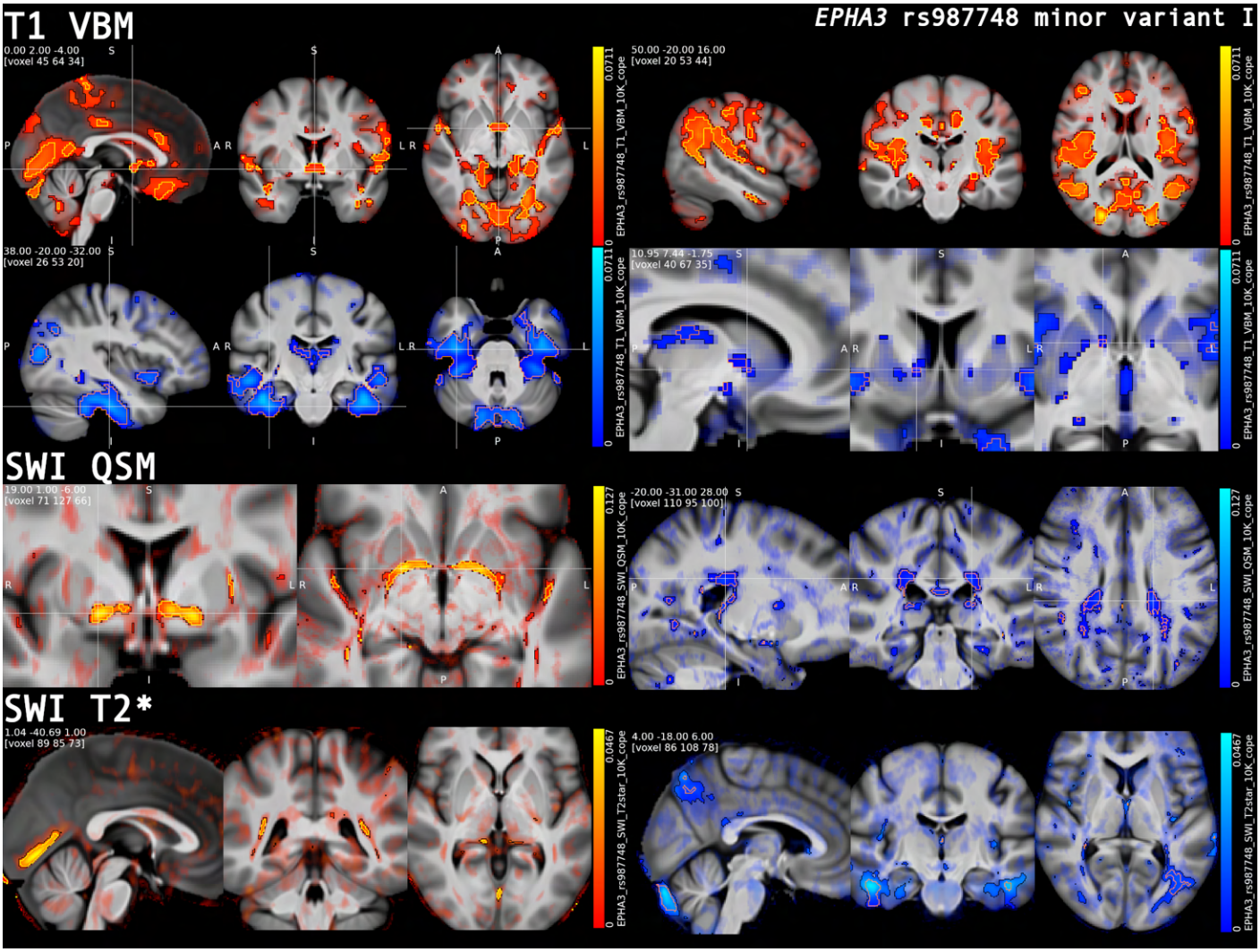


***Figure 10.1. EPHA3 rs987748: VBM and SWI.*** *The rs987748 minor allele showed a convergent signature across modalities centered on interhemispheric and temporal connectivity pathways. VBM revealed robust anterior commissure involvement alongside distributed fronto-parieto-occipital volume increases and temporally weighted volume decreases. SWI measures highlighted a particularly strong anterior commissure QSM (consistent, e.g., with decreased myelin signal) with additional cortical/subcortical susceptibility and T2* alterations extending into temporal and occipital cortices, consistent with widespread, pathway-anchored structural differences associated with this axon-guidance-related variant.* *Common visualization conventions (Figs. 10.1–10.5): β-maps thresholded at p_hFDR < 0.05 (black outline) overlaid on non-significant effects modulated by Z-statistic (surface views: non-significant effects shown by transparency, without Z-modulation), over the mean T1-weighted image. Positive associations are shown in red and negative associations in blue, contrast associations are displayed with a heatmap (NIH-fire); p_hFDR < 0.001 is outlined in yellow (positive and contrasts) or orange (negative), except on surface renderings, where p_hFDR < 0.001 is indicated in white. Group-mean resting-state network maps (Z-statistics) are thresholded at Z > 2.58 (approx. p < 0.01, two-tailed).*

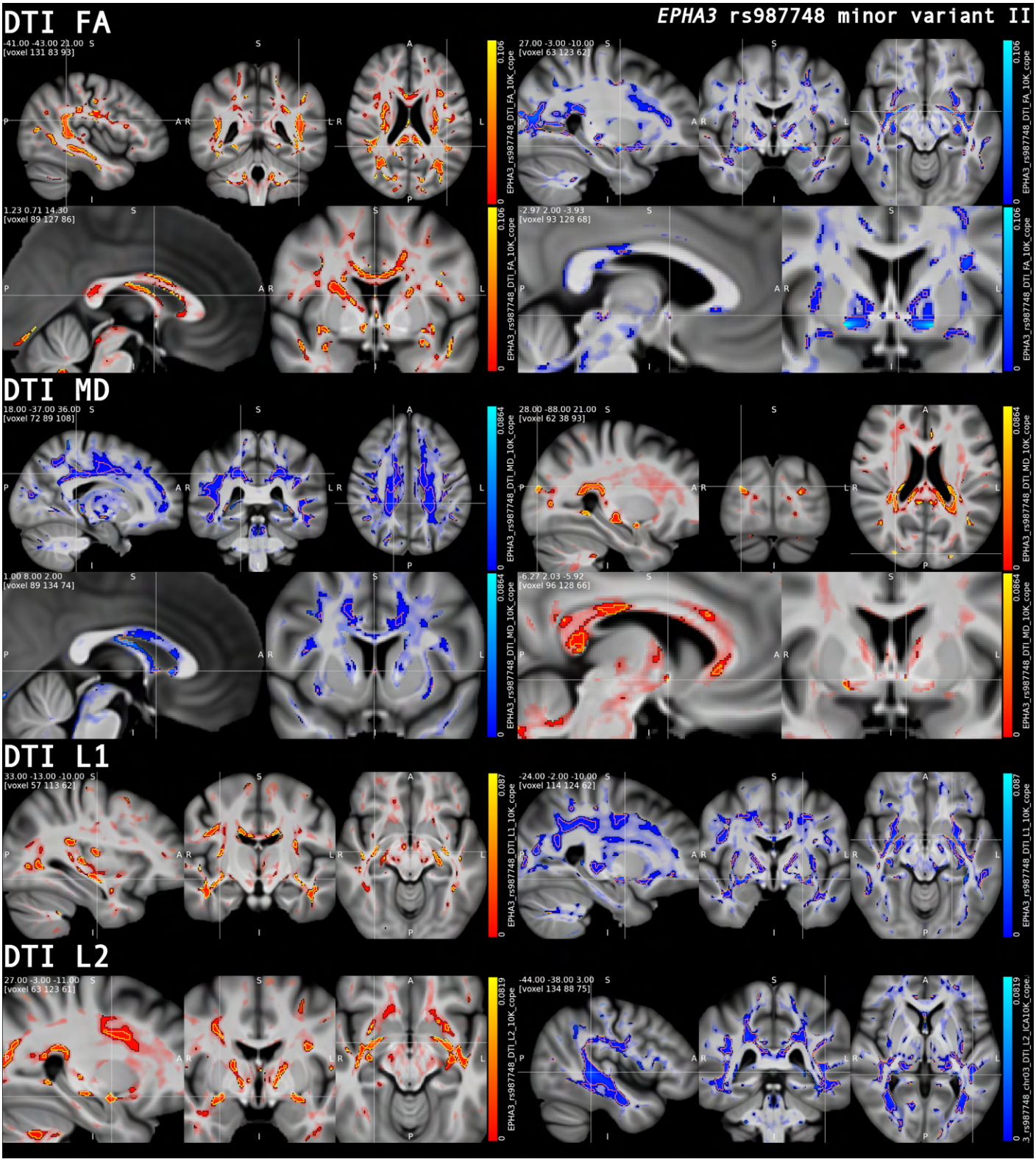


***Figure 10.2. EPHA3 rs987748: DTI.*** *Diffusion metrics showed anatomically structured rs987748 associations with prominent effects in the anterior commissure and distributed long-range pathways. Across DTI indices, significant clusters were reported in the temporal anterior commissure/uncinate region, posterior corpus callosum, arcuate and superior longitudinal fascicles, optic radiations, and occipital white matter. Notably, positive and negative associations frequently occurred in close spatial proximity (often adjacent along the same tract), consistent with fine-grained, boundary- and geometry-sensitive microstructural differences. (Visualization convention: Fig. 10.1.)*

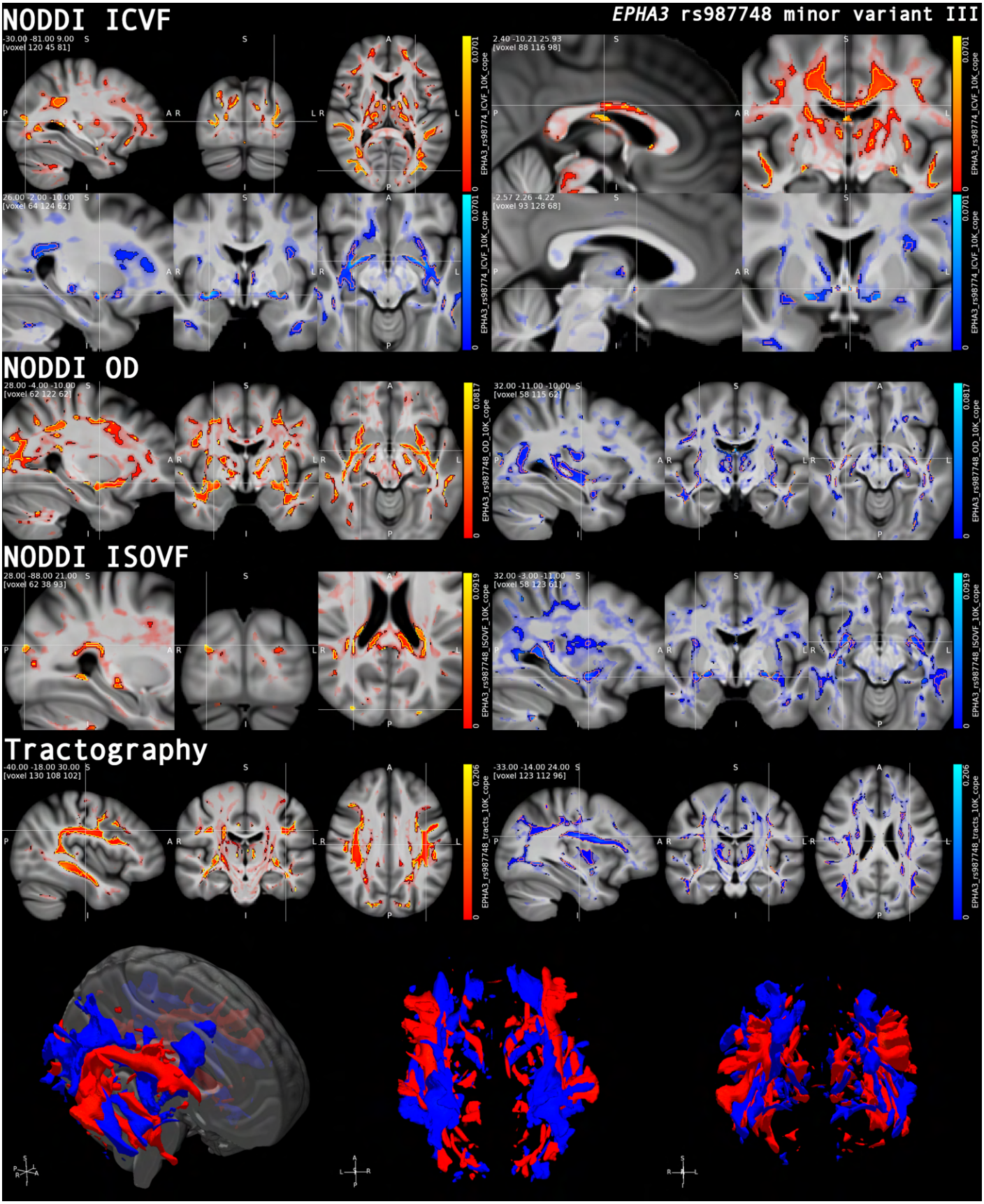


***Figure 10.3. EPHA3 rs987748: NODDI and tractography.*** *Robust rs987748 associations across commissural and distributed long-range pathways, with additional prominent effects in U-shaped fibers in temporal and occipital lobe. As for DTI, positive and negative associations were often directly adjacent along the same tract, suggesting fine-grained phenotypic variation (Visualization convention: Fig. 10.1.)*

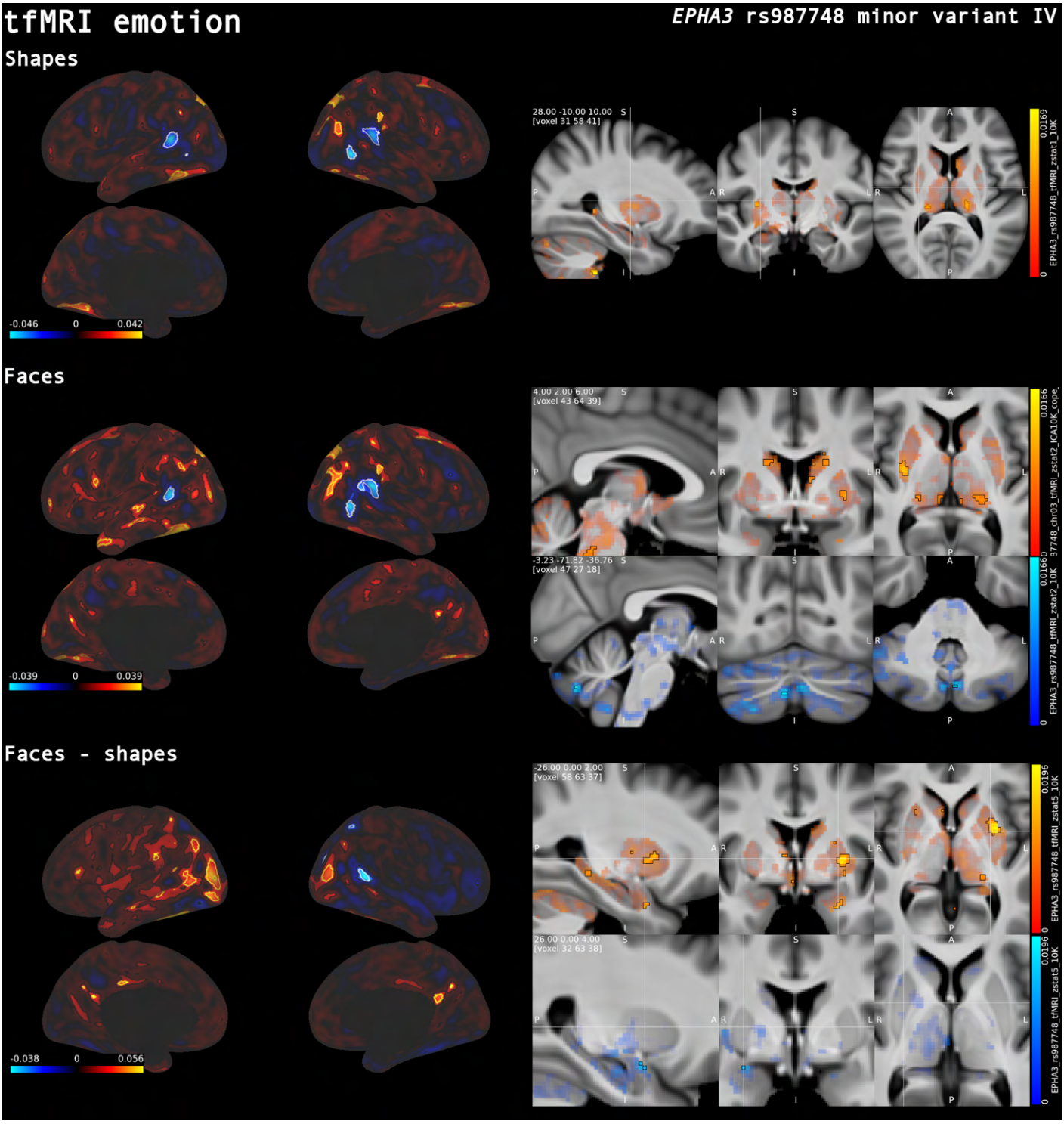


***Figure 10.4. EPHA3 rs987748: tfMRI emotion****. In the emotion task, rs987748 showed robust activation differences for shapes and faces, with consistent involvement of fusiform and inferior temporal cortex, supramarginal/angular gyri, and parieto-occipital transition areas, alongside frontal (dmPFC/vlPFC) and cingulate components. The faces − shapes contrast additionally highlighted occipito-temporal and posterior cingulate effects with subcortical involvement (left putamen). (Visualization convention: Fig. 10.1.)*

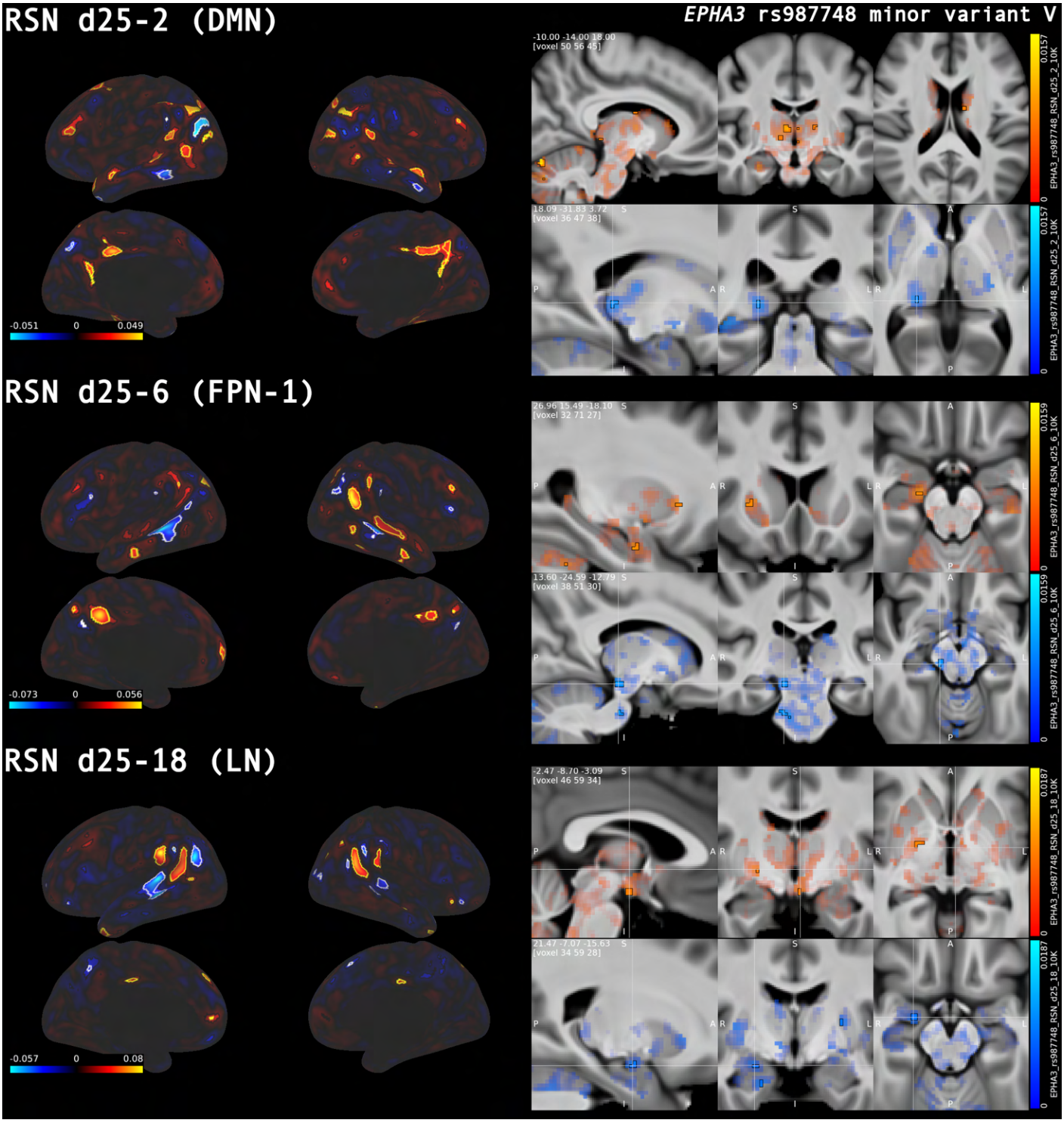


***Figure 10.5. EPHA3 rs987748: RSN.*** *Resting-state network analyses revealed rs987748-associated shifts in coupling across the DMN (RSN d25-2), a fronto-parietal network (RSN d25-6) and a language-like network (RSN d25-18). Effects were strongest in posterior midline and temporo-parietal hubs (e.g., posterior cingulate/precuneus, temporo-parietal junction, supramarginal/angular gyri) with additional involvement of prefrontal cortex and subcortical regions. Analogous to structural findings in diffusion imaging, coupling increases and decreases were often spatially adjacent within the same network, producing paired "up/down" patterns rather than uniformly signed shifts. (Visualization convention: Fig. 10.1.)*

**DTI MD:**

Diffusivity was increased for the minor variant with most robust evidence in temporal part of anterior commissure, bilateral LGN, and posterior callosum. Further increases with strong evidence included, left ACC (gray matter/white matter boundary), bilateral acoustic radiation, arcuate fascicle, and lateral occipital cortex / white matter.

MD decrease was related most robustly seen in bilateral amygdalo-striatal transition area posterior to anterior commissure, uncinate fascicles, superior temporal gyrus, pulvinar, in between posterior cingulum bundle and superior longitudinal fascicle, in arcuate fascicles, and occipital white matte. Further areas included radiation of corpus callosum, and small patches of frontal white matter.

**DTI FA:** Strongest evidence for increased FA was found in the paraventricular hypothalamic region, directly posterior to anterior commissure, adjacent to lateral amygdalae, in U-fibers connecting middle and superior temporal gyri, left uncinate fascicle, bilateral posterior putamen, mediodorsal thalamus, right Heschl's gyrus, right arcuate fascicle, bilateral optic radiation, and occipital short association fibers. Further strong evidence was found for FA increase in middle and posterior corpus callosum, bilateral FAT, and cerebellar white matter.

The minor variant exhibited most robust evidence for FA decrease in bilateral anterior commissure, inferior fronto-occipital fascicles (temporal part), bilateral LGN, arcuate fascicles, superior longitudinal fascicles, bilateral tapetum and stratum, and cerebellar white matter.

**NODDI ICVF:** Strongest evidence ($-\log_{10}(p)$ mapFDR > 10) for positive association of minor variant with neurite density was found for U-shaped fibers in between middle and superior temporal gyri, along right middle longitudinal fasciculus, bilateral arcuate fasciculi, bilateral amygdalo-striatal transition area, in callosal fibers lateral of bilateral cingulum bundles, in between superior longitudinal fasciculi 1 and 2, in posterior callosum, and in U-shaped fibers along occipital gyri. Further areas of strong evidence included thalamic radiations, right fornix, and left capsula externa.

Robust evidence for negative association with minor variant ($-\log_{10}(p)$ mapFDR > 60) was found for temporal parts of bilateral anterior commissure with further very strong evidence regions in bilateral LGN and tapetum (>10). Other strong evidence regions included fibers adjacent to sulcal fundi in perirhinal cortices, parahippocampal, fusiform and inferior frontal gyri as well as white matter deep in superior temporal gyri; bilateral arcuate fascicles, U-shaped and planar fibers along occipital gyri, and cerebellar white matter.

**NODDI isotropic volume fraction (ISOVF):** ISOVF increase was most evident ($-\log_{10}(p)$ mapFDR > 10) in posterior callosal fibers, with further strongly supported increases seen co-localized with U-shaped fibers seen for ICVF in between middle and superior temporal gyri, in right middle longitudinal fasciculus, adjacent to bilateral LGN, and in vertical occipital fasciculi.

ISOVF decrease was supported most strongly ($-\log_{10}(p)$ mapFDR > 15) in bilateral anterior commissure (lateral parts), further strong evidence regions included bilateral pulvinar, arcuate fascicles, inferior and middle longitudinal fascicles, bilateral optic radiations, planar white-matter patches along parietal and occipital cortices.

**NODDI OD:** Increase of orientation dispersion with the minor variant in lateral anterior commissure was one of the most statistically significant findings of the study with $-\log_{10}(p)$ mapFDR above 100. Further strong evidence was found in bilateral capsula interna and externa, bilateral cingulum bundle, fronto-basal white matter, inferior and middle longitudinal fasciculi, arcuate fasciculi, superior longitudinal fasciculi, vertical occipital fasciculi, and in mesencephalic and cerebellar white matter.

Evidence was strongest for decrease (>10) directly posterior to anterior commissure close to the midline, left FAT, in posterior callosum, bilateral optic radiations, arcuate fasciculi, U-shaped white matter between middle and superior temporal gyri, and amygdalo-striatal transition area. More strong evidence alterations were found in anterior callosum, thalamic radiations, hypothalamic region, superior longitudinal fasciculi, parieto-occipital white matter, between substantia nigra and red nuclei, and in cerebellar white matter.

**Tractography:** Robust evidence ($-\log_{10}(p)$ mapFDR > 60) was found for positive association of minor variant in the region of bilateral arcuate fascicle and superior longitudinal fascicle 3**.** Further regions of very strong evidence ($-\log_{10}(p)$ mapFDR >10) included bilateral uncinate fascicles, anterior commissure, FAT, inferior fronto-occipital fasciculi, U-shaped fibers between middle and superior temporal gyrus, bilateral optic radiations. Further regions of strong evidence included occipital and cerebellar white matter.

Decrease was most robustly supported with adjacent regions of left arcuate fascicle (>60) followed by right fascicle (>30), and U-shaped fibers between postcentral gyrus and supramarginal gyrus. Further regions of very strong evidence (>10) included anterior commissure and external capsule. Other regions of strong evidence included middle longitudinal fascicles, and right FAT.

**RSN d25-2 (DMN):** Evidence for increased coupling with minor variant was most robust in left posterior cingulate cortex ($-\log_{10}(p)$ mapFDR > 15). Further strong evidence increases included bilateral dlPFC, left dmPFC, temporal cortices, supramarginal and angular gyri, right precuneus, occipital gyri and left cerebellum. Coupling was decreased with strong evidence in adjacent regions in temporal cortex, left angular gyrus, and left precuneus.

**RSN d25-6 (FPN-1):** Coupling was increased with most robust evidence in left precuneus followed by right temporo-parietal junction ($-\log_{10}(p)$ mapFDR >15; >10). Further strong evidence regions were found in right precuneus, across temporal cortices, right dlPFC, left mPFC, bilateral supramarginal and angular gyri.

Evidence for decreased coupling was most robust in bilateral middle temporal gyrus ($-\log_{10}(p)$ mapFDR > 20). Other regions with strong evidence for decrease included bilateral vlPFC, bilateral precuneus, supramarginal gyri and right angular gyrus.

**RSN d25-18 (LN):** Coupling in the language-like network RSN_d25-18 was most robustly increased in left supramarginal gyrus and right temporo-parietal junction ($-\log_{10}(p)$ mapFDR > 20). Other strong evidence areas included bilateral temporal pole, right anterior insula, bilateral mid/posterior cingulate cortex.

Coupling was most robustly decreased in adjacent areas in left superior temporal cortex and angular gyrus ($-\log_{10}(p)$ mapFDR > 20; >15). Other strong evidence areas with decrease included bilateral middle temporal cortex, bilateral vlPFC, right dmPFC, left precuneus, and right occipital gyri.

**tfMRI zstat (shapes):** Increased activation was strongly supported for the minor variant in right dmPFC, bilateral fusiform cortices, inferior temporal gyri, right supramarginal and posterior angular gyrus and bilateral parieto-occipital transition area.

Strongest decrease ($-\log_{10}(p)$ mapFDR >10) was seen in bilateral supramarginal gyrus/superior temporal gyrus and posterior part of right middle temporal gyrus. Other strongly supported decreases were seen in left middle temporal gyrus

**tfMRI zstat (faces):** Minor variant exhibited strongly supported increased a more scattered pattern across frontal, temporal and parietal regions, again including fusiform cortices, parieto-occipital transition and supramarginal regions. Decrease was strongly supported in posterior parts of superior temporal gyri and right middle temporal gyrus.

**tfMRI zstat (faces − shapes):** Strongest support ($-\log_{10}(p)$ mapFDR >10) was found for increased BOLD response in left occipital cortex posterior to middle temporal gyrus. Further strong evidence regions were found in left vlPFC and dmPFC, bilateral fusiform cortices, left middle temporal gyrus, inferior temporal gyri, left mid- and posterior cingulate cortex, right posterior cingulate cortex, left supramarginal gyrus, bilateral angular gyrus, temporo-occipital area and left putamen. Strong evidence for decreased activation was found in right middle temporal gyrus, right superior parietal lobule, and bilateral occipital lobes.

### **3.3.3 Experiment 5:** Multimodal effects of separate polygenic scores derived from early- and late-diagnosis autism latent factor GWAS

Multimodal associations of the early- and late-diagnosis autism polygenic scores were found in 6 / 10 tested sub-modalities (Figs. 11.1–11.3), revealing dissociable white-matter signatures as well as convergent effects in amygdala.

**T1 VBM:**

Moderate evidence was found for decreased gray matter left cerebellum (VI / crus I) for early-ASD polygenic score (PS), while evidence supported decrease in contralateral side. The combination of early- and late-ASD PS was further associated with increased volume in left amygdala, right anterior insula, and bilateral cerebellum (crus I). Left angular gyrus exhibited greater volume for early-ASD than late-ASD PS. Left dlPFC exhibited greater volume for late-ASD than for early-ASD PS.

**SWI T2*:** T2* was not significantly associated with either early- or late-ASD PS using the 10K-supervoxels. Using the more sensitive 1K-supervoxels left mid/anterior hippocampus was associated with early-ASD PS (significant after hierarchical FDR correction within 1K analysis using same sub-modalities as for primary analysis), and to a lesser extent to the additive combination of both scores.

**SWI QSM:** Same as for T2*, no associations were found using 10K-supervoxel analysis. Using 1K-supervoxels, early-ASD PS was associated with moderate evidence with decrease in right posterior insula and supported increase in left posterior putamen (surface region). Late-ASD PS was associated with decreased QSM in anterior commissure and bilateral pallidum.

**NODDI ICVF:** Neurite density was increased with moderate evidence for late-ASD PS in frontal and fronto-basal white matter, as well as in between bilateral forceps major and cingulum bundle, while evidence supported further increases in temporo-parietal and occipital white matter. Early-ASD PS was associated with moderate evidence of decreased ICVF in a longitudinal segment of white matter in between right corticospinal tract and cingulum bundle as well as anterior callosum. Moderate evidence was further found in direct contrast with early-ASD PS for higher density in frontal lobe white matter, right inferior claustrum, left middle temporal gyrus, white matter in between left entorhinal and parahippocampal cortex, area between corticospinal tract and cingulum bundles, optic radiations, and occipital white matter.

Evidence supported decreased ICVF in bilateral pallidum for early-ASD and decreased signal for late-ASD PS in left anterior commissure, right frontal operculum and LGN, as well as bilateral fusiform cortex white matter.

**NODDI OD:** Moderate evidence was found for increased orientation dispersion for late-ASD PS in right uncinate fascicle and for higher signal in direct contrast with early-ASD PS. Evidence further supported decreased OD for right cerebellar white matter for early-ASD PS and combined early- and late-ASD PS. Right pallidal OD was higher for early-ASD PS than for late-ASD PS.

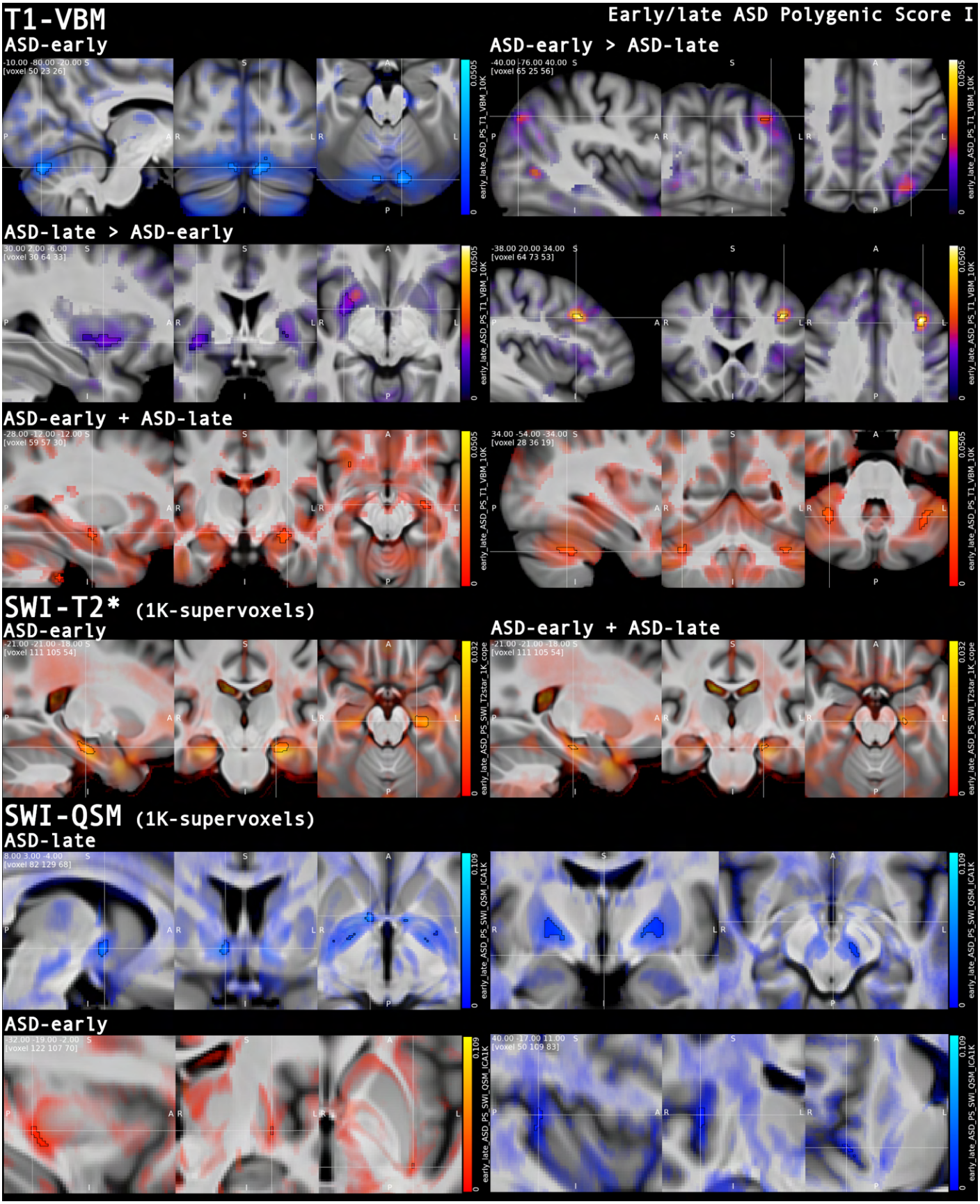


***Figure 11.1. Early/late-diagnosis ASD polygenic score: VBM and SWI.*** *VBM showed distinct and convergent effects of early- vs. late-ASD polygenic scores, including cerebellar reductions for early-ASD PS and combined-score increases in left amygdala, right anterior insula and bilateral cerebellum; contrasts highlighted greater angular gyrus volume for early-ASD PS and greater left dlPFC volume for late-ASD PS. No significant SWI (T2*/QSM) effects were*

*detected with 10K-supervoxels; in another illustration of its higher sensitivity, exploratory 1K-supervoxel analysis revealed focal SWI associations such as increased T2* in hippocampus for early- and combined ASD score and reduced QSM in anterior commissure for late-ASD score. Common visualization conventions (Figs. 11.1–11.3): β-maps thresholded at p_hFDR < 0.05 (black outline) overlaid on non-significant effects modulated by Z-statistic (surface views: non-significant effects shown by transparency, without Z-modulation), over the mean T1-weighted image. Positive associations are shown in red and negative associations in blue, contrast associations are displayed with a heatmap (NIH-fire).*

**DTI FA:** FA was not significantly increased for either early- or late-ASD PS, while combined scores were associated with increase in bilateral cerebellar white matter. Moderate evidence supported decreased FA adjacent to right claustrum, anterior callosum, left posterior cingulate bundle, and across bilateral corticospinal tract for early-ASD score. Evidence supported higher FA for late-ASD score than early-ASD along bilateral amygdala, posterior capsula externa, callosum and in longitudinally oriented patches across frontal, parietal and occipital white matter.

**DTI MD:** No moderate evidence associations were found for MD. Evidence supported higher MD for early-ASD PS localized in left FAT. Late-ASD PS was not significantly associated with MD. Direct contrasting between the two scores revealed widespread higher MD signal for early-ASD PS centered on frontal lobe and extending into parieto-occipital white matter.

**tfMRI zstat (shapes):** No significant associations were found for shapes using 10K analysis.

**tfMRI zstat (faces):** Moderate evidence was found for reduced coupling of right precuneus in response to negative faces for the combination of high early-ASD and late-ASD PS, while evidence supported decreased coupling in left precuneus also.

**tfMRI zstat (faces − shapes):** No significant associations were found for faces over shapes using 10K analysis. An exploratory analysis with the more sensitive 1K-supervoxels (across same sub-modalities) supported widespread cortical reductions in BOLD response.

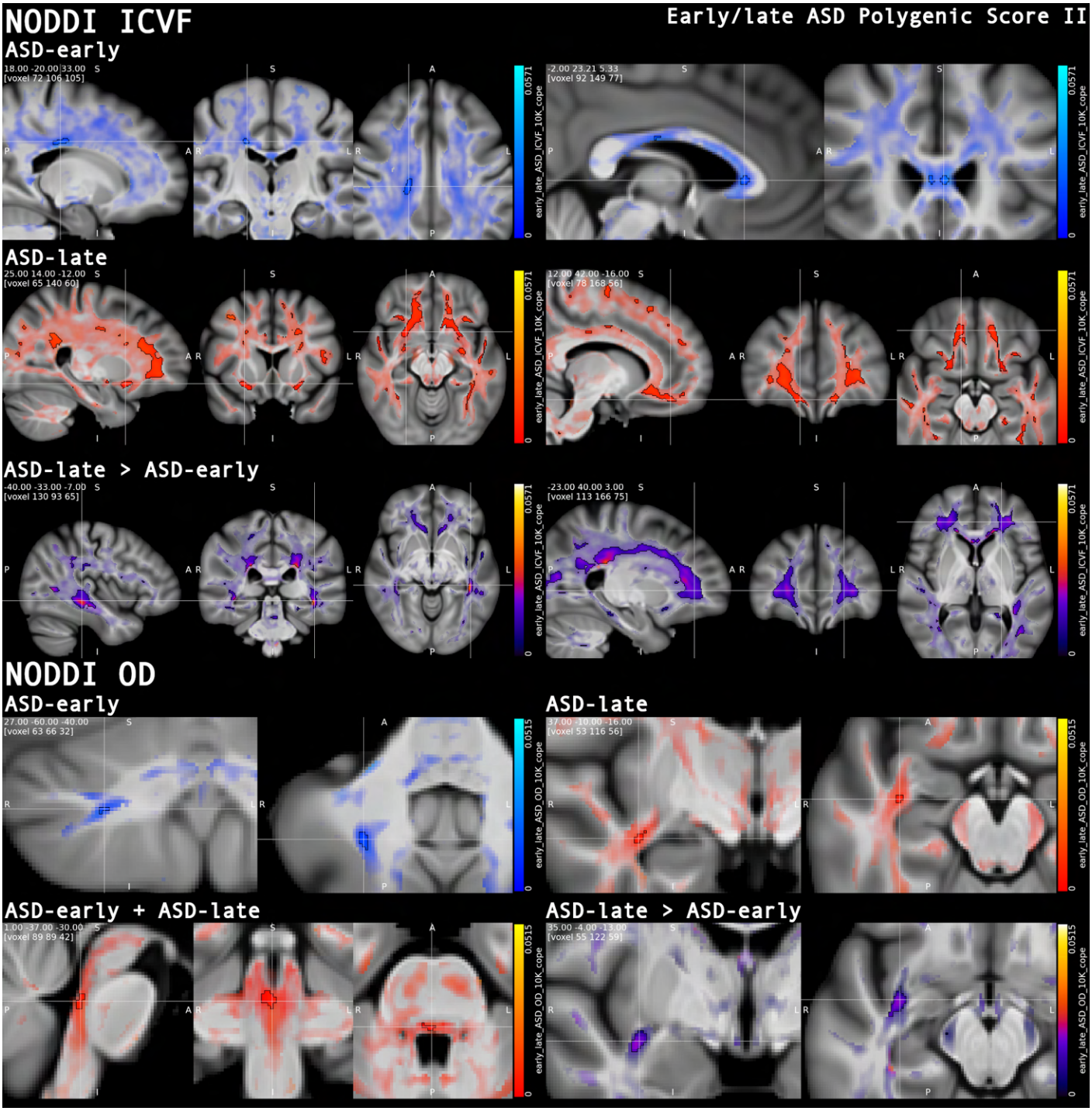


***Figure 11.2 Early/late-diagnosis ASD polygenic score: NODDI.*** *NODDI highlighted dissociable white-matter signatures, with late-ASD PS showing increases in neurite density (ICVF) concentrated in frontal white matter, whereas early-ASD PS showed ICVF reductions in anterior callosum and a longitudinal tract segment between corticospinal and cingulum pathways. Contrast maps further highlighted higher ICVF for late- than early-ASD PS across frontal, temporal and occipital pathways. Late-ASD PS further associated with increased OD in right uncinate fascicle. (Visualization convention: Fig. 11.1.)*

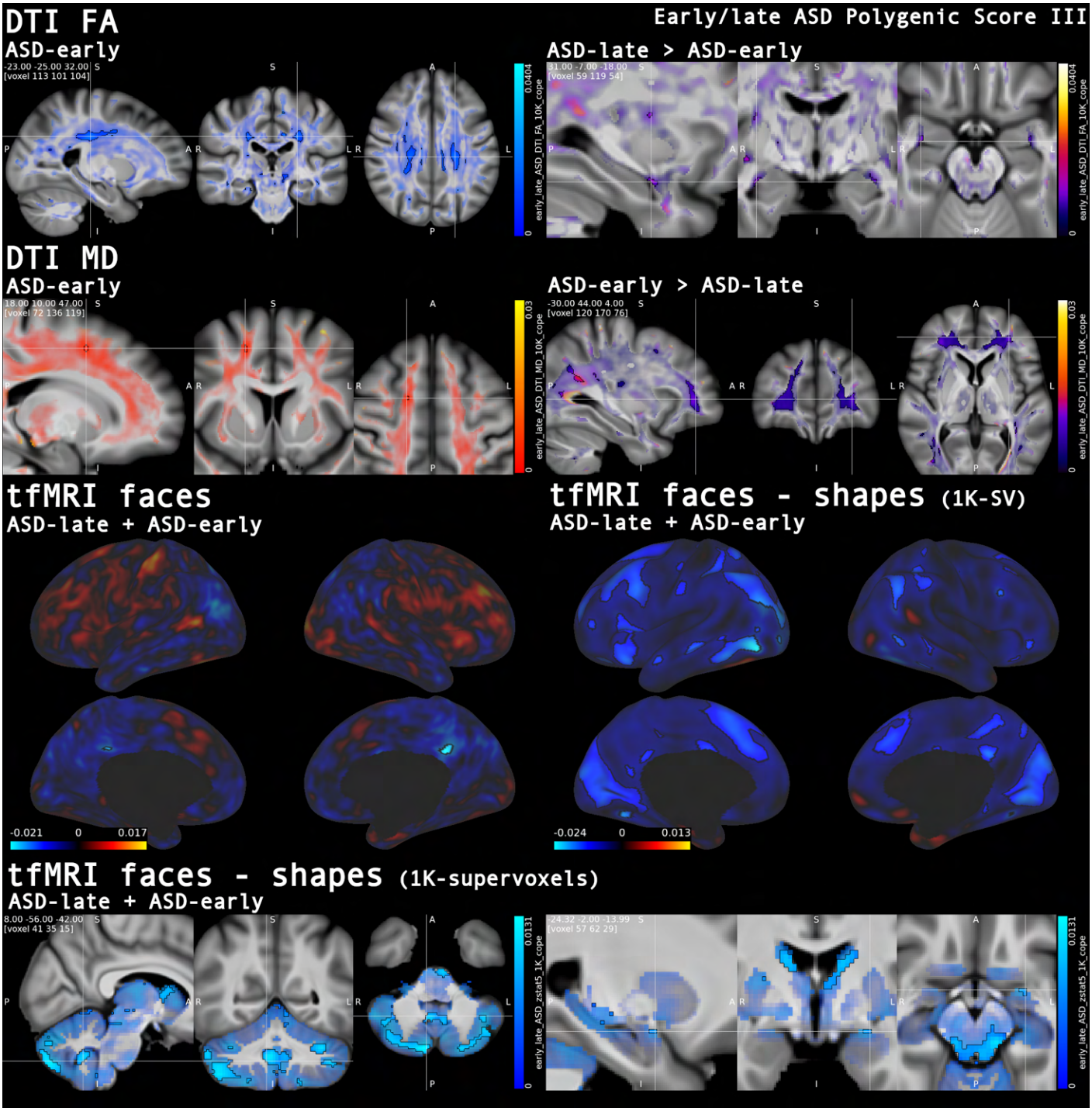


***Figure 11.3 Early/late-diagnosis ASD polygenic score: DTI and tfMRI emotion.*** *DTI showed dissociable microstructural associations for early- vs. late-ASD polygenic scores: early-ASD PS was linked to FA reductions (e.g., anterior callosum, posterior cingulum and corticospinal tracts), whereas late-ASD PS showed higher FA than early-ASD along amygdala-adjacent white matter. Frontal MD was further higher for early-ASD than for late-ASD scores. In tfMRI, the combined scores showed moderate-evidence reduced posterior cingulate cortex/precuneus responses to negative faces; exploratory 1K-supervoxel analysis suggested more widespread cortical and subcortical reductions in BOLD response to the faces – shapes contrast. (Visualization convention: Fig. 11.1)*

## 4. Discussion

With PANDORA, we provide a major resource and computationally efficient analysis framework for multimodal population neuroimaging. Alongside streamlined general and modality-specific processing and a convenient data layout, we have validated information retention in compressed versions of the MRI maps, which we term supervoxels. A core component is a new mathematical regression formulation that naturally bridges encoding to full-resolution space analysis, while leveraging memory and speed benefits of the supervoxels. Using quantitative and qualitative comparisons, we show that supervoxels offer a faster and more powerful alternative to full-resolution univariate analyses with distinct statistical and spatial properties emerging for 1K- and 10K-variants. The tool is implemented as an expansion of FSL's *fsl_glm* in C++, prioritizing speed.

Across five experiments, we demonstrate the real-world utility and potential of the resource, showing: widespread brain changes associated with cumulative trauma; disentangled effects of anxiety and depressive symptoms on the brain; differential alterations associated with smoking, coffee and alcohol; voxel-level mapping of changes associated with *EPHA3*; and the first brain mapping of the differential effects of two polygenic scores derived for early- and late-diagnosed autism. Key findings from these experiments are discussed below.

**Supervoxels and supervoxel GLM:** information retention, power and speed

Comparing full-resolution variance per sub-modality explained by 1K-/10K-supervoxels vs. multimodal IDPs (~5K) we found that supervoxels explain more variance than IDPs in every sub-modality. On average, 10K-supervoxels explained over 95%, 1K-supervoxels around 58%, and multimodal IDPs less than 20% of the variance. Importantly, variance explained does not account for different levels of noise in the data, where removal is appropriate. Inherently noisy sub-modalities such as SWI QSM or DTI MO (mode of anisotropy), for instance, exhibited among the lowest levels of explained variance.

We compared power for supervoxel and full-resolution GLM in all sub-modalities using the sum of squared z-statistics for the effect of smoking across voxels and grayordinates with uncorrected $p < 0.001$. 1K-supervoxels outperformed 10K-supervoxels in 95 of 98 sub-modalities and full-resolution in 93 of 98; 10K-supervoxels outperformed full-resolution analyses in 84 of 98 sub-modalities (Wilcoxon signed-rank). In noisy sub-modalities or when dealing with noise in the target phenotype, such an increase in power can result in exposure of otherwise hidden effects (Fig. 5A). Direct comparison revealed a high spatial overlap between 10K-supervoxels and full-resolution results, which was not completely matched by the 1K-variant. 1K-supervoxels may lack discriminative power for the most highly localized effects (Fig. 5AB).

Cloud storage and computing incur high costs on research projects and may impede full usage of valuable resources such as UK Biobank. Speed of analysis, which directly drives computing costs, can act as a separate factor of friction. Large datasets, moreover, increase memory requirements and often demand special computational strategies to run on even high-RAM instances. PANDORA addresses these problems in several ways. First, the new supervoxel data comes with a massive disk-space reduction of up to 98.7 and 87.2 % for 1K- and 10K-variants, respectively. Our supervoxel-regression method further capitalizes on this advantage by estimating its model in encoding space directly, which at the same time reduces the amount of computation and avoids building up the full-resolution matrix in memory. Benchmark analyses thus revealed a substantial speed-up for the 1K-supervoxels analyses across modalities of all sizes. As the SVD-step within the regression scales quadratically with the number of components, 10K-supervoxel analyses are faster than full-resolution analyses for 1mm-resolution whole-brain modalities

(~2x). A further necessary step for reducing the memory footprint of PANDORA analyses is online computation and chunking, which has been implemented for both supervoxel and full-resolution modes. To achieve fast read times, the data-layout along the stride-1 axis is important. While for full-resolution analyses, the entire data matrix has to be streamed, the supervoxel modes only stream the spatial maps, resulting in greatly reduced I/O times. In order to increase overall speed, all modes were fully parallelized using the C++ standard library. Lastly, we deliberately chose C++ over python for reasons of computational efficiency and explicit handling of memory and parallelization.

To demonstrate the utility of PANDORA across domains, we performed five GLM experiments. Here we discuss the key findings from these experiments:

**Experiment I:** Lifetime trauma load, nigrostriatal iron and multimodal structural-functional alterations in the general population

In a first multimodal, single-regressor experiment, we investigated the effects of cumulative traumatic experiences on the brain (Figs. 6.1 – 6.2).

Lifetime trauma was associated with increased QSM signal in the substantia nigra with strong evidence compatible with higher iron content. Strikingly, posttraumatic stress disorder (PTSD) has been shown to increase the risk of Parkinson's disease (PD) with reported hazard ratios between 1.48 and 3.46 (Barer et al., 2022; Chan et al., 2017). While chronic restraint stress has been shown to trigger dopaminergic loss in substantia nigra in rats (Sugama et al., 2016), to the best of our knowledge, a direct anatomical link in humans has not previously been reported. Bilateral putamen, a downstream region of pathology for PD, was a further area with strong evidence for QSM increase. A rat model of PTSD exhibited neuronal injury in the striatum caused by iron deposition (Zhao et al., 2016). Intriguingly, an association of trauma with decreased QSM signal (e.g., compatible with more myelin or less iron) was strongly supported in a cerebellar thalamic region (VLpv), which has been related to tremor in PD due to lack of inhibition via dopamine (Dirkx et al., 2017).

Strong evidence indicated global white matter signal shifts across diffusion sub-modalities and T2* with increasing trauma load, consistent with a degenerative process. Specifically, we observed infra- and supratentorial increases in MD, decreases in FA and neurite density (ICVF).

White matter changes have been reported in relation to PTSD and stress across many studies (Dennis et al., 2021; Li et al., 2016). A meta-analysis in adults and children with the disorder reported FA reductions in corpus callosum, cingulate and frontal regions but could not pinpoint any specific areas in a coordinate-based analysis (Siehl et al., 2018). In a multi-cohort study of 1426 individuals with PTSD and controls Dennis et al. (2021) report lower FA in the tapetum region of the corpus callosum. Interestingly, an early structural study in small sample of PTSD patients and controls reported generalized white matter atrophy (Villarreal et al., 2002), which would be consistent with our findings here.

Dysregulation of the hypothalamic-pituitary-adrenal (HPA) axis has been further implicated in PTSD (Raise-Abdullahi et al., 2023). We found strong evidence for microstructural alterations in hypothalamus with increased fiber orientation dispersion (OD) co-localized with decreased QSM signal, which can be a sign of increased myelination. Together these changes are consistent with remodeling of hypothalamic connectivity, which has shown to be predictive of prolonged stress (Jensen et al., 2024).

In our analysis of voxel-based morphometry (VBM) maps, we found strong evidence for volume reduction in bilateral amygdalo-hippocampal complex with peak evidence for the right posterior amygdala.

While hippocampal volume loss has been reported for PTSD across many studies (Logue et al., 2018), results regarding amygdala have been mixed (review: Ben-Zion et al., 2024). Amygdala volumes have, for instance, been reported to be enlarged in war-veterans with PTSD than without (Kuo et al., 2012). However, greater combat exposure was associated with smaller amygdala in the same study. A different study also conducted in veterans with and without PTSD from the same year found smaller amygdala volumes in PTSD and no association with trauma load (Morey et al., 2012). Notably, smaller amygdala volume has been associated with PTSD severity in veterans and traumatized youths (Homan et al., 2019; Ousdal et al., 2020).

A variety of methods have been used in measuring amygdala volume, which, together with the fact that amygdala consists of many subnuclei, may well contribute to these inconsistencies . Here, we observed peak evidence localized in the in right posterior parts of amygdala (Z = -7.110). Right amygdala IDP (UKB ID: 25889) for comparison showed much lower evidence (Z = -4.171).

In an emotion task, we found increased activation in anterior hippocampus and the default mode network (DMN) in response to fearful and angry faces (faces – shapes contrast) with higher traumatic experiences load.

In a previous experimental study, anterior hippocampal BOLD response was related to level of threat in an approach-avoidance task but better explained by avoidance behavior (Abivardi et al., 2020), a core symptom of PTSD (American Psychiatric Association, 2013; World Health Organization, 2022). Remarkably, fearful facial expression have been shown to provoke approach behavior in healthy subjects (Hammer & Marsh, 2015), while the default mode network has been found to deactivate in response to negative faces (Sreenivas et al., 2012).

We further found strong evidence of altered resting-state networks including reduced coupling of precuneus within DMN, which is consistent with finding in women with early-life trauma-related PTSD and veterans (Bluhm et al., 2009; Miller et al., 2017).

It should be noted that findings from clinical PTSD samples may not fully generalize to trauma-exposed individuals with subclinical symptoms or to the broader general population. Because our analyses focus on exposure rather than clinical symptomatology, the observed brain effects are also likely to capture mechanisms of resilience. In fact, peri- and posttraumatic ventromedial prefrontal cortex (vmPFC) volume, which has been reported to relate to resilience across several studies (Roeckner et al., 2021), as well as an anterior region in dorsolateral prefrontal cortex (dlPFC) identified to be expanded in trauma-exposed healthy controls vs. PTSD patients (Zilcha-Mano et al., 2022) both exhibited higher VBM signal here.

We further note that our cumulative trauma score does not differentiate between childhood and adult traumatic experiences.

**Experiment II:** Dissociable brain signatures of anxiety and depressive symptom dimensions

In a second experiment, we investigated differential effects of depressive and anxiety symptoms in the general population (Figs. 8.1 – 8.6). Specifically, we compared the first principal component of recent symptom load from depression- and anxiety-specific online follow-up questionnaires. Of note, we did not include sleep disturbances in the analysis, which are bidirectionally related to both anxiety and depression.

Strong evidence was found for association of depressive symptom load with increased putamen volume in the posterior aspect, while anxiety symptom load supported increased volume in anterior caudo-putamen.

These findings contrast reports for major depressive disorder where putamen has been generally found to be decreased (Lu et al., 2016; Sacchet et al., 2016), and may be related to the more subclinical view here.

Strong evidence linked depressive symptoms to volume loss in bilateral amygdalo-hippocampal complex with peak in right centromedial amygdala, whereas anxiety was associated with increased volume in anterior hippocampus. Directly contrasting anxiety – depressive symptom load further strongly supported larger left anterior hippocampus volume for anxiety.

Hippocampal volume loss has been consistently shown for major depressive disorder (Roddy et al., 2019; Wise et al., 2017), while results for amygdala involvement, similar to PTSD, have been mixed (Roddy et al., 2021). This finding resonates with a study by Rusch et al. (2001), which showed that hippocampal volumes were positively associated with trait anxiety in both healthy and depressed subjects.

A recent priority letter examining amygdala responses to negative faces in depression UKB found no association (Tamm et al., 2022). Specifically, the study investigated the relationship between current depressive symptoms median BOLD effect for faces – shapes contrast in a group-defined amygdala-activation mask (UKB ID: 25052) for 28,638 individuals. The summed depressive index (from the imaging date) included three questions related to core depressive symptoms, and one anxiety-related item.

We revisited the question of missing amygdala activation in the Hariri emotion task (Hariri et al., 2002), albeit with the anxiety and depressive symptom principal components, and across all three contrast z-statistic tfMRI sub-modalities.

Strikingly, we found increased amygdala reactivity for the first depressive symptom principal component in right amygdala to both shapes and faces, while the principal component for anxiety related negatively with task amygdala activation for both. Correspondingly, the contrast of depressive symptoms – anxiety symptoms was positively associated with bilateral basolateral amygdala activation to shapes, and bilateral centromedial amygdala. The combined effect of anxiety and depressive components on amygdala BOLD response was negative in response in both subtasks.

Not unexpectedly, as we found increased reactivity for both shapes and emotional faces in higher depressive symptom load, we did not find an association with the faces – shapes contrast. However, using the higher sensitivity 1K-supervoxel analysis, we were able to detect a positive association with higher left centromedial amygdala reactivity to faces over shapes with depressive over anxiety symptom load.

Diffusion-weighted analyses exhibited stronger signs of white matter deterioration associated with depressive symptoms than anxiety, with supra- and infratentorial decreases in ICVF and FA as well as accompanying increase in MD. Similar to the effect of cumulative trauma, depressive symptoms were also associated with increased orientation dispersion in hypothalamus. Interestingly, we found strong evidence for a highly localized reduction of neurite density (ICVF) in left motor cortex for anxiety. Incidentally, a recent study in mice has shown that motor cortex activation via treadmill exercise can reduce anxiety-like behaviors (Luo et al., 2025). Peak evidence for the combined positive effect of anxiety and depressive symptom load on orientation dispersion was seen in the right medial forebrain bundle, a known target of deep brain stimulation in treatment-resistant depression (Fenoy et al., 2022).

**Experiment III:** Brain-wide structural, iron and connectivity effects of smoking, coffee and alcohol

In a third experiment, we investigated the effects of the most commonly used neuromodulators in the population, i.e., smoking, coffee and alcohol (Figs. 9.1 – 9.12). We found widespread and varied results

across sub-modalities. Broadly speaking alcohol and nicotine were associated with more general, degenerative changes, while effects of coffee were less pronounced. Here, we will discuss a few findings of interest.

VBM analysis revealed widespread volume reductions across all substances, with direct comparisons in general suggesting that the effects of alcohol were the strongest overall, closely followed by nicotine, which specifically seemed to have the most deleterious effect on the striatum.

Smoking showed strong evidence for higher volume in bilateral parahippocampal cortices and moderate to strong evidence for increase in bilateral dlPFC. Interestingly, reduction of dlPFC coupling with parahippocampal gyrus using electrical stimulation reduces craving in smokers (Yang et al., 2017).

Relation of coffee intake with volume increase in bilateral nucleus accumbens, bed nucleus of stria terminalis (BNST), hypothalamus and (approx. basolateral) amygdala was strongly supported. Coffee consumption was further associated with volume reduction in vmPFC, which was also apparent contrasting the effect of smoking.

Strong evidence was found for volume increase in bilateral precuneus with higher alcohol consumption.

We found robust evidence for iron accumulation (QSM) in striatum, substantia nigra and to a lesser extent hippocampus for both smoking and alcohol consumption, while alcohol was further associated with substantially increased QSM in cortex, cerebellum and amygdala. While to lesser extent, coffee consumption also showed strong evidence for accumulation in the striatum. Peak evidences for QSM increase and T2* decrease with coffee consumption was interestingly found in the sleep-regulating habenula (Hikosaka, 2010).

Diffusion sub-modalities further reinforced evidence for degenerative changes with respect to smoking and alcohol consumption but not coffee, showing global MD increases, and FA/ICVF decreases for the former two. Coffee consumption was, however, associated with loss of integrity in corpus callosum, albeit to a lesser extent than alcohol. Moreover, analysis of the warpfield Jacobian exhibited signs of smaller callosal volume in its anterior and posterior aspect. Remarkably, a random allocation of caffeine or placebo for apnea in premature infants resulted in smaller corpus callosum at age 11 (Kelly et al., 2018).

Neurite density increase was found for coffee consumption in medial forebrain bundle, hypothalamus and bilateral uncinate fasciculus, while both smoking and alcohol exhibited strong evidence for higher density surrounding the putamen.

Coffee use has been reported to reduce PD risk linearly and be protective of Alzheimer's disease (Kolahdouzan & Hamadeh, 2017; Zhou & Zhang, 2021). In our analysis, coffee intake was, nevertheless, linked to increased QSM signal in striatum and medial part of substantia nigra. In PD, substantia nigra degeneration starts it its lateral compartment (Duke et al., 2007), which has been related to motor function, while medial substantia nigra co-activates with limbic regions (Zhang et al., 2017). For tobacco, amount smoked has been inversely related to PD risk (Mappin-Kasirer et al., 2020). Here, we observed strongest evidence for QSM increase in white matter between substantia nigra and red nucleus rather than substantia nigra.

Analyses of resting-state networks exhibited strong evidence for effects of alcohol on the default mode, a salience-like, and two frontoparietal networks. In the default mode network (RSN d25-2), alcohol intake was associated not only with increased coupling across core regions but also across numerous distributed cortical patches, consistent with reduced network specificity. This is consistent with reports of functional dedifferentiation after just one month chronic alcohol intake (Pérez-Ramírez et al., 2022), commonly seen

with aging (Malagurski et al., 2020). Alcohol similarly showed extensive coupling alterations including broader cortical recruitment in salience-like RSN d25-9 and two tested frontoparietal networks (RSN d25-6/11). Smoking and coffee, in contrast, related to limited effects with focal increased coupling of left somatosensory cortex within RSN d25-9, and reduced coupling of temporo-parietal junction in fronto-parietal network RSN d25-6, respectively.

**Experiment IV:** An *EPHA3* variant shaping interhemispheric and temporal connectivity

In a fourth and first of two genetic studies, we analyzed the effect of *EPHA3* SNP rs987748 (A:C) on the brain (Figs. 10.1 – 10.5). Ephrin signaling plays core roles in axon guidance, cell migration (Kania & Klein, 2016), and tissue patterning (Janis et al., 1999); *EPHA3* gene mutations have been implicated in glioblastoma (Day et al., 2013) and autism (Casey et al., 2012).

In a previous study, we found that the minor allele of rs987748 was associated with occipital lobe resting-state functional connectivity with the left hemisphere (ICA100 edge 383), as well as with rfMRI connectivity ICA-feature 3, a derived summary measure of whole-brain functional connectivity (Smith et al., 2021; see Supplementary Figure S18.3 for the spatial pattern of this component). A weaker association of the major allele with baseline fluid intelligence is reported in Schoeler et al. (2025; Supplementary Data 3).

Across diffusion modalities and QSM a common picture emerged with some of the most robust evidence. The minor allele was associated with decreased microstructural integrity of anterior commissure (e.g., peak evidence for increased fiber dispersion of $-\log_{10}(p)$_mapFDR > 100) and temporal lobe connectivity via anterior commissure/uncinate fascicle. On the other hand, we found increased integrity of the mid corpus callosum and of long-range temporo-parietal and parieto-occipital fiber tracts. We commonly saw positive and negative associations in the same tracts but with slightly shifted location, compatible with fine-grained control of tract geometry/positioning and local fiber architecture.

These microstructural effects were combined with strong evidence for volumetric differences associated with the minor variant, specifically, reduced temporal lobe and dorsal thalamus volumes, and increased volumes in fronto-parieto-occipital lobes. Functional analyses exhibited striking left-lateralization in face perception tasks across cortical and subcortical regions, while tests in resting state networks revealed distinct anatomical shifts in activity. Left-lateralization of face perception network has previously been described in left-handed men (Thome et al., 2022). A different SNP near the *EPHA3* gene has recently been related to hemispheric differences in language network connectivity in UKB (Amelink et al., 2024). Interestingly, high *EPHA3* expression has been found in the developing dorsal thalamus of rats (Mackarehtschian et al., 1999).

*EPHA3* is expressed in anterior commissure and corpus callosum of mice (Kudo et al., 2005). While *EPHA3* has been implicated in callosal axon segregation (Nishikimi et al., 2011) and *EPHA4* is required for anterior commissure formation (Dottori et al., 1998), evidence for a link between disrupted anterior commissure found in *Olig2* knockout mice and *EPHA3* have previously remained inconclusive (Gotoh et al., 2023).

**Experiment V:** Divergent frontal–callosal architecture and a converging amygdala signature of early and late autism risk

In a last experiment, we analyzed the effect of early- and late-diagnosis autism polygenic scores on the brain (Figs. 11.1 – 11.3).

Zhang et al. (2025) reported that genetic profiles in autism differ by age at diagnosis, with partially distinct polygenic architectures and only modest genetic correlation between early- and late-diagnosed groups. An early-diagnosis factor was associated with lower early social and communication abilities, whereas a late-diagnosis factor related to higher socioemotional problems and showed positive genetic correlations with ADHD and other psychiatric disorders. Using the age-of-diagnosis–stratified GWAS summary statistics, we constructed separate, scores in UKB and entered them jointly into a single GLM. In our sample, the scores were effectively uncorrelated and derived from non-overlapping SNP sets, allowing straightforward estimation of dissociable effects as well as their combined associations.

A first key finding from this analysis was increased neurite density (ICVF) in frontal white matter specific to the late-autism polygenic score (PS) and divergent from early-autism PS effect. Early autism PS, in contrast, revealed reductions of neurite density in corpus callosum. Alterations in local frontal lobe connectivity have been implicated in autism across numerous studies (Courchesne & Pierce, 2005; Kana et al., 2014). A mixed age (range 3-36 y) study of corpus callosum found increased variability for midsagittal callosal area in autism vs. neurotypical controls, while higher callosal area was correlated with higher intelligence and faster processing speed within autism (Prigge et al., 2013). Interestingly, complete agenesis of corpus callosum has also been associated with increased autistic symptoms and communication problems (Paul et al., 2014).

Early autism PS was further associated with decreased FA in superior longitudinal fasciculus (SLF), which connects frontal and parietal regions, and cingulum, while late autism PS was not. Late autism PS was associated with higher FA values than early PS in amygdalar anterior commissure, adjacent to uncinate fasciculus. A study limited to male autistic subjects with average/above-average IQ found increase in the SLF FA (Fitzgerald et al., 2018). A small study with average/below-average IQ found decreases in both (Jou et al., 2011). A longitudinal study of white matter development in 125 autistic children (age range 2.5 – 7.0) revealed slower development of fractional anisotropy in cingulum, SLF and corpus callosum in comparison to controls (Andrews et al., 2021). Interestingly, greater increases in uncinate fasciculus FA were associated with decreased symptom severity over time.

Orientation dispersion of right uncinate fasciculus was further increased with higher late-autism PS against baseline and contrasting against early-autism PS. Right uncinate fasciculus microstructure has been related to reduced facial emotion discrimination (Coad et al., 2020).

The amygdala has been a cornerstone of autism research for more than two decades (Baron-Cohen et al., 2000). Evidence of amygdala volume changes associated with ASD have in general reported overgrowth in early childhood (Mosconi et al., 2009; Sparks et al., 2002), and normal or reduced volumes in adolescent and adult individuals with ASD (Nacewicz et al., 2006; Schumann et al., 2004). Surprisingly, only the additive effect of early- and late-autism scores was related to increased left amygdala volume. A recent study comparing 72 autistic participants and controls using the Hariri paradigm (Hariri et al., 2002) was not able to detect any difference in mean amygdala activity during emotional face processing, specifically the faces – shapes contrast (Langenbach et al., 2024). This was also true for our 10K-supervoxel analysis. However, using the 1K-supervoxels, we did detect reduced activation in left (central) amygdala for combined early and late scores.

**PANDORA in practice:** recommendations and future directions

Overall, given their high spatial fidelity, reduced computational burden and increased statistical power in most cases, 10K-supervoxels can be used as replacement and arguably be given preference over full-resolution analyses. The case for 1K-supervoxel analyses is more complex. The clear advantage with respect to power can come at the cost of effect localization.

Plans for future releases include tuning supervoxel components per modality, creating cross-modal encodings, revisiting the intensity-normalization question for T1/T2, adding grey matter diffusion maps and expanding the PANDORA toolset to include machine-learning workflows.

**In summary,** PANDORA delivers a scalable, RAP-native framework that standardizes voxel/grayordinate access across 98 UKB sub-modalities, introduces information-preserving supervoxels, and implements a new supervoxel-regression that operates in encoding space while returning full-resolution statistics. Benchmarks show major I/O, memory, and runtime gains; 10K-supervoxels closely match and can be used as a drop-in replacement for full-voxel analyses, while 1K-supervoxels boost power for low-SNR effects. Across five experiments spanning exposure, neuropsychiatric, and genetic domains, we replicated known effects and uncovered new multimodal associations, demonstrating that supervoxel analyses accelerate discovery and maximize sensitivity.

## Data and Code Availability

- PANDORA modality folders can be accessed on the UKB RAP cloud platform using the procedure described here: https://open.oxcin.ox.ac.uk/pages/pandora/web/.
- Code for the PANDORA processing pipeline is available at: https://git.fmrib.ox.ac.uk/PANDORA/pandora_proc.
- The *fsl_glm* expansion source code is available within the MELODIC package: https://git.fmrib.ox.ac.uk/fsl/melodic.

## Author Contributions

Conceptualization: A.A., K.L.M, S.J., M.W.W., T.E.N., S.M.S.

Methodology: A.A., S.M.S, T.E.N., M.W., W.G., C.F.B., L.T.E.

Software: A.A. and M.W. (core implementation); F.A.-A., L.R., P.M., S.M.S.

Formal analysis: A.A., S.M.S.

Investigation: A.A., S.M.S.

Data curation: A.A., P.M., S.M.S.

Writing – original draft: A.A., T.E.N., S.M.S.

Writing – review & editing: A.A., M.W., P.C., F.A.-A., L.R., K.L.M., S.J., M.W.W., W.G., C.F.B., L.T.E., T.E.N., S.M.S.

Supervision: S.M.S.

## Funding

The Wellcome Centre for Integrative Neuroimaging (WIN FMRIB) is supported by core funding from the Wellcome Trust (203139/Z/16/Z). Wellcome Trust Collaborative Award 215573/Z/19/Z.

## Declaration of Competing Interests

SMS is co-founder and part-owner of SBGneuro. Other authors have no relevant financial or non-financial interests to disclose.

## Supplementary Material

Peak evidence tables for experiments I-V.

## References

Abivardi, A., Khemka, S., & Bach, D. R. (2020). Hippocampal Representation of Threat Features and Behavior in a Human Approach–Avoidance Conflict Anxiety Task. *The Journal of Neuroscience*, *40*(35), 6748. https://doi.org/10.1523/JNEUROSCI.2732-19.2020

Afzalian, N., & Rajimehr, R. (2021). Spatially Adjacent Regions in Posterior Cingulate Cortex Represent Familiar Faces at Different Levels of Complexity. *The Journal of Neuroscience*, *41*(47), 9807. https://doi.org/10.1523/JNEUROSCI.1580-20.2021

Alfaro-Almagro, F., Jenkinson, M., Bangerter, N. K., Andersson, J. L. R., Griffanti, L., Douaud, G., Sotiropoulos, S. N., Jbabdi, S., Hernandez-Fernandez, M., Vallee, E., Vidaurre, D., Webster, M., McCarthy, P., Rorden, C., Daducci, A., Alexander, D. C., Zhang, H., Dragonu, I., Matthews, P. M., . . . Smith, S. M. (2018). Image processing and Quality Control for the first 10,000 brain imaging datasets from UK Biobank. *Neuroimage*, *166*, 400-424. https://doi.org/10.1016/j.neuroimage.2017.10.034

Alfaro-Almagro, F., McCarthy, P., Afyouni, S., Andersson, J. L. R., Bastiani, M., Miller, K. L., Nichols, T. E., & Smith, S. M. (2021). Confound modelling in UK Biobank brain imaging. *Neuroimage*, *224*, 117002. https://doi.org/10.1016/j.neuroimage.2020.117002

Amelink, J. S., Postema, M. C., Kong, X.-Z., Schijven, D., Carrión-Castillo, A., Soheili-Nezhad, S., Sha, Z., Molz, B., Joliot, M., Fisher, S. E., & Francks, C. (2024). Imaging genetics of language network functional connectivity reveals links with language-related abilities, dyslexia and handedness. *Communications Biology*, *7*(1), 1209. https://doi.org/10.1038/s42003-024-06890-3

American Psychiatric Association (2013). *Diagnostic and statistical manual of mental disorders* (5th ed.). American Psychiatric Association. https://doi.org/10.1176/appi.books.9780890425596

Andrews, D. S., Lee, J. K., Harvey, D. J., Waizbard-Bartov, E., Solomon, M., Rogers, S. J., Nordahl, C. W., & Amaral, D. G. (2021). A Longitudinal Study of White Matter Development in Relation to Changes in Autism Severity Across Early Childhood. *Biological Psychiatry*, *89*(5), 424-432. https://doi.org/https://doi.org/10.1016/j.biopsych.2020.10.013

Barer, Y., Chodick, G., Glaser Chodick, N., & Gurevich, T. (2022). Risk of Parkinson Disease Among Adults With vs Without Posttraumatic Stress Disorder. *JAMA Network Open*, *5*(8), e2225445-e2225445. https://doi.org/10.1001/jamanetworkopen.2022.25445

Baron-Cohen, S., Ring, H. A., Bullmore, E. T., Wheelwright, S., Ashwin, C., & Williams, S. C. R. (2000). The amygdala theory of autism. *Neuroscience & Biobehavioral Reviews*, *24*(3), 355-364. https://doi.org/https://doi.org/10.1016/S0149-7634(00)00011-7

Ben-Zion, Z., Korem, N., Fine, N. B., Katz, S., Siddhanta, M., Funaro, M. C., Duek, O., Spiller, T. R., Danböck, S. K., Levy, I., & Harpaz-Rotem, I. (2024). Structural Neuroimaging of Hippocampus and Amygdala Subregions in Posttraumatic Stress Disorder: A Scoping Review. *Biological Psychiatry Global Open Science*, *4*(1), 120-134. https://doi.org/https://doi.org/10.1016/j.bpsgos.2023.07.001

Benjamini, Y., & Bogomolov, M. (2014). Selective Inference on Multiple Families of Hypotheses. *Journal of the Royal Statistical Society Series B: Statistical Methodology*, *76*(1), 297-318. https://doi.org/10.1111/rssb.12028

Benjamini, Y., & Hochberg, Y. (1995). Controlling the False Discovery Rate: A Practical and Powerful Approach to Multiple Testing. *Journal of the Royal Statistical Society. Series B (Methodological)*, *57*(1), 289-300. http://www.jstor.org/stable/2346101

Bluhm, R. L., Williamson, P. C., Osuch, E. A., Frewen, P. A., Stevens, T. K., Boksman, K., Neufeld, R. W. J., Théberge, J., & Lanius, R. A. (2009). Alterations in default network connectivity in posttraumatic stress disorder related to early-life trauma. *Journal of Psychiatry and Neuroscience*, *34*(3), 187-194. https://doi.org/10.1139/jpn.0925

Carlén, M. (2017). What constitutes the prefrontal cortex? *Science*, *358*(6362), 478-482. https://doi.org/doi:10.1126/science.aan8868

Casey, J. P., Magalhaes, T., Conroy, J. M., Regan, R., Shah, N., Anney, R., Shields, D. C., Abrahams, B. S., Almeida, J., Bacchelli, E., Bailey, A. J., Baird, G., Battaglia, A., Berney, T., Bolshakova, N., Bolton, P. F., Bourgeron, T., Brennan, S., Cali, P., . . . Ennis, S. (2012). A novel approach of homozygous haplotype sharing identifies candidate genes in autism spectrum disorder. *Human Genetics*, *131*(4), 565-579. https://doi.org/10.1007/s00439-011-1094-6

Chan, Y.-L. E., Bai, Y.-M., Hsu, J.-W., Huang, K.-L., Su, T.-P., Li, C.-T., Lin, W.-C., Pan, T.-L., Chen, T.-J., Tsai, S.-J., & Chen, M.-H. (2017). Post-traumatic Stress Disorder and Risk of Parkinson Disease: A Nationwide Longitudinal Study. *The American Journal of Geriatric Psychiatry*, *25*(8), 917-923. https://doi.org/https://doi.org/10.1016/j.jagp.2017.03.012

Choi, S. W., Mak, T. S.-H., & O'Reilly, P. F. (2020). Tutorial: a guide to performing polygenic risk score analyses. *Nature Protocols*, *15*(9), 2759-2772. https://doi.org/10.1038/s41596-020-0353-1

Coad, B. M., Postans, M., Hodgetts, C. J., Muhlert, N., Graham, K. S., & Lawrence, A. D. (2020). Structural connections support emotional connections: Uncinate Fasciculus microstructure is related to the ability to decode facial emotion expressions. *Neuropsychologia*, *145*, 106562. https://doi.org/https://doi.org/10.1016/j.neuropsychologia.2017.11.006

Courchesne, E., & Pierce, K. (2005). Why the frontal cortex in autism might be talking only to itself: local over-connectivity but long-distance disconnection. *Current Opinion in Neurobiology*, *15*(2), 225-230. https://doi.org/https://doi.org/10.1016/j.conb.2005.03.001

Day, Bryan W., Stringer, Brett W., Al-Ejeh, F., Ting, Michael J., Wilson, J., Ensbey, Kathleen S., Jamieson, Paul R., Bruce, Zara C., Lim, Yi C., Offenhäuser, C., Charmsaz, S., Cooper, Leanne T., Ellacott, Jennifer K., Harding, A., Leveque, L., Inglis, P., Allan, S., Walker, David G., Lackmann, M., . . . Boyd, Andrew W. (2013). EphA3 Maintains Tumorigenicity and Is a Therapeutic Target in Glioblastoma Multiforme. *Cancer Cell*, *23*(2), 238-248. https://doi.org/https://doi.org/10.1016/j.ccr.2013.01.007

Dennis, E. L., Disner, S. G., Fani, N., Salminen, L. E., Logue, M., Clarke, E. K., Haswell, C. C., Averill, C. L., Baugh, L. A., Bomyea, J., Bruce, S. E., Cha, J., Choi, K., Davenport, N. D., Densmore, M., du Plessis, S., Forster, G. L., Frijling, J. L., Gonenc, A., . . . Morey, R. A. (2021). Altered white matter microstructural organization in posttraumatic stress disorder across 3047 adults: results from the PGC-ENIGMA PTSD consortium. *Molecular Psychiatry*, *26*(8), 4315-4330. https://doi.org/10.1038/s41380-019-0631-x

Dirkx, M. F., den Ouden, H. E. M., Aarts, E., Timmer, M. H. M., Bloem, B. R., Toni, I., & Helmich, R. C. (2017). Dopamine controls Parkinson's tremor by inhibiting the cerebellar thalamus. *Brain*, *140*(3), 721-734. https://doi.org/10.1093/brain/aww331

Dottori, M., Hartley, L., Galea, M., Paxinos, G., Polizzotto, M., Kilpatrick, T., Bartlett, P. F., Murphy, M., Köntgen, F., & Boyd, A. W. (1998). EphA4 (Sek1) receptor tyrosine kinase is required for the development of the corticospinal tract. *Proceedings of the National Academy of Sciences*, *95*(22), 13248-13253. https://doi.org/10.1073/pnas.95.22.13248

Duke, D. C., Moran, L. B., Pearce, R. K. B., & Graeber, M. B. (2007). The medial and lateral substantia nigra in Parkinson's disease: mRNA profiles associated with higher brain tissue vulnerability. *Neurogenetics*, *8*(2), 83-94. https://doi.org/10.1007/s10048-006-0077-6

Fenoy, A. J., Quevedo, J., & Soares, J. C. (2022). Deep brain stimulation of the "medial forebrain bundle": a strategy to modulate the reward system and manage treatment-resistant depression. *Molecular Psychiatry*, *27*(1), 574-592. https://doi.org/10.1038/s41380-021-01100-6

Fitzgerald, J., Leemans, A., Kehoe, E., O'Hanlon, E., Gallagher, L., & McGrath, J. (2018). Abnormal fronto-parietal white matter organisation in the superior longitudinal fasciculus branches in autism spectrum disorders. *European Journal of Neuroscience*, *47*(6), 652-661. https://doi.org/https://doi.org/10.1111/ejn.13655

Folk, M., Heber, G., Koziol, Q., Pourmal, E., & Robinson, D. (2011). *An overview of the HDF5 technology suite and its applications* Proceedings of the EDBT/ICDT 2011 Workshop on Array Databases, Uppsala, Sweden. https://doi.org/10.1145/1966895.1966900

Gillis, G., Bhalerao, G., Blane, J., Mitchell, R., Pretorius, P. M., McCracken, C., Nichols, T. E., Smith, S. M., Miller, K. L., Alfaro-Almagro, F., Raymont, V., Martos, L., Mackay, C. E., & Griffanti, L. (2025). From Big Data to the Clinic: Methodological and Statistical Enhancements to Implement the UK Biobank Imaging Framework in a Memory Clinic. *Hum Brain Mapp*, *46*(3), e70151. https://doi.org/10.1002/hbm.70151

Glasser, M. F., Smith, S. M., Marcus, D. S., Andersson, J. L. R., Auerbach, E. J., Behrens, T. E. J., Coalson, T. S., Harms, M. P., Jenkinson, M., Moeller, S., Robinson, E. C., Sotiropoulos, S. N., Xu, J., Yacoub, E., Ugurbil, K., & Van Essen, D. C. (2016). The Human Connectome Project's neuroimaging approach. *Nature Neuroscience*, *19*(9), 1175-1187. https://doi.org/10.1038/nn.4361

Gotoh, H., Maruyama, K., Yoshii, K., Yamauchi, N., Nomura, T., Ohtsuka, S., Shirasaki, R., Takebayashi, H., & Ono, K. (2023). Disruption of the anterior commissure in Olig2 deficient mice. *European Journal of Neuroscience*, *57*(1), 5-16. https://doi.org/https://doi.org/10.1111/ejn.15861

Hammer, J. L., & Marsh, A. A. (2015). *Why do fearful facial expressions elicit behavioral approach? Evidence from a combined approach-avoidance implicit association test* [doi:10.1037/emo0000054].

Hariri, A. R., Tessitore, A., Mattay, V. S., Fera, F., & Weinberger, D. R. (2002). The Amygdala Response to Emotional Stimuli: A Comparison of Faces and Scenes. *Neuroimage*, *17*(1), 317-323. https://doi.org/https://doi.org/10.1006/nimg.2002.1179

Harris, C. R., Millman, K. J., van der Walt, S. J., Gommers, R., Virtanen, P., Cournapeau, D., Wieser, E., Taylor, J., Berg, S., Smith, N. J., Kern, R., Picus, M., Hoyer, S., van Kerkwijk, M. H., Brett, M.,

Haldane, A., del Río, J. F., Wiebe, M., Peterson, P., . . . Oliphant, T. E. (2020). Array programming with NumPy. *Nature*, *585*(7825), 357-362. https://doi.org/10.1038/s41586-020-2649-2

Hikosaka, O. (2010). The habenula: from stress evasion to value-based decision-making. *Nature Reviews Neuroscience*, *11*(7), 503-513. https://doi.org/10.1038/nrn2866

Homan, P., Levy, I., Feltham, E., Gordon, C., Hu, J., Li, J., Pietrzak, R. H., Southwick, S., Krystal, J. H., Harpaz-Rotem, I., & Schiller, D. (2019). Neural computations of threat in the aftermath of combat trauma. *Nature Neuroscience*, *22*(3), 470-476. https://doi.org/10.1038/s41593-018-0315-x

Hua, K., Zhang, J., Wakana, S., Jiang, H., Li, X., Reich, D. S., Calabresi, P. A., Pekar, J. J., van Zijl, P. C. M., & Mori, S. (2008). Tract probability maps in stereotaxic spaces: Analyses of white matter anatomy and tract-specific quantification. *Neuroimage*, *39*(1), 336-347. https://doi.org/https://doi.org/10.1016/j.neuroimage.2007.07.053

Hyvärinen, A., & Oja, E. (2000). Independent component analysis: algorithms and applications. *Neural Networks*, *13*(4), 411-430. https://doi.org/https://doi.org/10.1016/S0893-6080(00)00026-5

Jakab, A., Blanc, R., Berényi, E. L., & Székely, G. (2012). Generation of Individualized Thalamus Target Maps by Using Statistical Shape Models and Thalamocortical Tractography. *American Journal of Neuroradiology*, *33*(11), 2110. https://doi.org/10.3174/ajnr.A3140

Janis, L. S., Cassidy, R. M., & Kromer, L. F. (1999). Ephrin-A Binding and EphA Receptor Expression Delineate the Matrix Compartment of the Striatum. *The Journal of Neuroscience*, *19*(12), 4962. https://doi.org/10.1523/JNEUROSCI.19-12-04962.1999

Jenkinson, M., Beckmann, C. F., Behrens, T. E. J., Woolrich, M. W., & Smith, S. M. (2012). FSL. *Neuroimage*, *62*(2), 782-790. https://doi.org/https://doi.org/10.1016/j.neuroimage.2011.09.015

Jensen, D. E. A., Ebmeier, K. P., Suri, S., Rushworth, M. F. S., & Klein-Flügge, M. C. (2024). Nuclei-specific hypothalamus networks predict a dimensional marker of stress in humans. *Nature Communications*, *15*(1), 2426. https://doi.org/10.1038/s41467-024-46275-y

Jou, R. J., Jackowski, A. P., Papademetris, X., Rajeevan, N., Staib, L. H., & Volkmar, F. R. (2011). Diffusion Tensor Imaging in Autism Spectrum Disorders: Preliminary Evidence of Abnormal Neural Connectivity. *Australian & New Zealand Journal of Psychiatry*, *45*(2), 153-162. https://doi.org/10.3109/00048674.2010.534069

Kana, R. K., Uddin, L. Q., Kenet, T., Chugani, D., & Müller, R.-A. (2014). Brain connectivity in autism [Editorial]. *Frontiers in Human Neuroscience*, *Volume 8 - 2014*. https://doi.org/10.3389/fnhum.2014.00349

Kania, A., & Klein, R. (2016). Mechanisms of ephrin–Eph signalling in development, physiology and disease. *Nature Reviews Molecular Cell Biology*, *17*(4), 240-256. https://doi.org/10.1038/nrm.2015.16

Kelly, C. E., Ooi, W. L., Yang, J. Y.-M., Chen, J., Adamson, C., Lee, K. J., Cheong, J. L. Y., Anderson, P. J., Doyle, L. W., & Thompson, D. K. (2018). Caffeine for apnea of prematurity and brain development at 11 years of age. *Annals of Clinical and Translational Neurology*, *5*(9), 1112-1127. https://doi.org/https://doi.org/10.1002/acn3.628

Kolahdouzan, M., & Hamadeh, M. J. (2017). The neuroprotective effects of caffeine in neurodegenerative diseases. *CNS Neuroscience & Therapeutics*, *23*(4), 272-290. https://doi.org/https://doi.org/10.1111/cns.12684

Krauth, A., Blanc, R., Poveda, A., Jeanmonod, D., Morel, A., & Székely, G. (2010). A mean three-dimensional atlas of the human thalamus: Generation from multiple histological data. *Neuroimage*, *49*(3), 2053-2062. https://doi.org/https://doi.org/10.1016/j.neuroimage.2009.10.042

Kudo, C., Ajioka, I., Hirata, Y., & Nakajima, K. (2005). Expression profiles of EphA3 at both the RNA and protein level in the developing mammalian forebrain. *Journal of Comparative Neurology*, *487*(3), 255-269. https://doi.org/https://doi.org/10.1002/cne.20551

Kuo, J. R., Kaloupek, D. G., & Woodward, S. H. (2012). Amygdala Volume in Combat-Exposed Veterans With and Without Posttraumatic Stress Disorder: A Cross-sectional Study. *Archives of General Psychiatry*, *69*(10), 1080-1086. https://doi.org/10.1001/archgenpsychiatry.2012.73

Langenbach, B. P., Grotegerd, D., Mulders, P. C. R., Tendolkar, I., van Oort, J., Duyser, F., van Eijndhoven, P., Vrijsen, J. N., Dannlowski, U., Kampmann, Z., & Koelkebeck, K. (2024). Autistic and non-autistic individuals show the same amygdala activity during emotional face processing. *Molecular Autism*, *15*(1), 2. https://doi.org/10.1186/s13229-024-00582-9

Li, L., Lei, D., Li, L., Huang, X., Suo, X., Xiao, F., Kuang, W., Li, J., Bi, F., Lui, S., Kemp, G. J., Sweeney, J. A., & Gong, Q. (2016). White Matter Abnormalities in Post-traumatic Stress Disorder Following a Specific Traumatic Event. *EBioMedicine*, *4*, 176-183. https://doi.org/https://doi.org/10.1016/j.ebiom.2016.01.012

Logue, M. W., van Rooij, S. J. H., Dennis, E. L., Davis, S. L., Hayes, J. P., Stevens, J. S., Densmore, M., Haswell, C. C., Ipser, J., Koch, S. B. J., Korgaonkar, M., Lebois, L. A. M., Peverill, M., Baker, J. T., Boedhoe, P. S. W., Frijling, J. L., Gruber, S. A., Harpaz-Rotem, I., Jahanshad, N., . . . Morey, R. A. (2018). Smaller Hippocampal Volume in Posttraumatic Stress Disorder: A Multisite ENIGMA-PGC Study: Subcortical Volumetry Results From Posttraumatic Stress Disorder Consortia. *Biological Psychiatry*, *83*(3), 244-253. https://doi.org/https://doi.org/10.1016/j.biopsych.2017.09.006

Lu, Y., Liang, H., Han, D., Mo, Y., Li, Z., Cheng, Y., Xu, X., Shen, Z., Tan, C., Zhao, W., Zhu, Y., & Sun, X. (2016). The volumetric and shape changes of the putamen and thalamus in first episode, untreated major depressive disorder. *NeuroImage: Clinical*, *11*, 658-666. https://doi.org/https://doi.org/10.1016/j.nicl.2016.04.008

Luo, Z., Chen, J., Liu, Y., Dai, Y., Gao, H., Zhang, B., Ou, H., So, K.-F., Wei, J.-a., & Zhang, L. (2025). Treadmill exercise prevents stress-induced anxiety-like behaviors via enhancing the excitatory input from the primary motor cortex to the thalamocortical circuit. *Nature Communications*, *16*(1), 939. https://doi.org/10.1038/s41467-025-56258-2

Mackarehtschian, K., Lau, C. K., Caras, I., & McConnell, S. K. (1999). Regional Differences in the Developing Cerebral Cortex Revealed by Ephrin-A5 Expression. *Cerebral Cortex*, *9*(6), 601-610. https://doi.org/10.1093/cercor/9.6.601

Mai, J. K., Majtanik, M., & Paxinos, G. (2015). *Atlas of the human brain*. Academic press.

Malagurski, B., Liem, F., Oschwald, J., Mérillat, S., & Jäncke, L. (2020). Functional dedifferentiation of associative resting state networks in older adults – A longitudinal study. *Neuroimage*, *214*, 116680. https://doi.org/https://doi.org/10.1016/j.neuroimage.2020.116680

Mappin-Kasirer, B., Pan, H., Lewington, S., Kizza, J., Gray, R., Clarke, R., & Peto, R. (2020). Tobacco smoking and the risk of Parkinson disease. *Neurology*, *94*(20), e2132-e2138. https://doi.org/10.1212/WNL.0000000000009437

Miller, D. R., Hayes, S. M., Hayes, J. P., Spielberg, J. M., Lafleche, G., & Verfaellie, M. (2017). Default Mode Network Subsystems Are Differentially Disrupted in Posttraumatic Stress Disorder. *Biological Psychiatry: Cognitive Neuroscience and Neuroimaging*, *2*(4), 363-371. https://doi.org/https://doi.org/10.1016/j.bpsc.2016.12.006

Morel, A. (2007). *Stereotactic atlas of the human thalamus and basal ganglia*. CRC Press.

Morey, R. A., Gold, A. L., LaBar, K. S., Beall, S. K., Brown, V. M., Haswell, C. C., Nasser, J. D., Wagner, H. R., McCarthy, G., & Mid-Atlantic Mirecc Workgroup, f. t. (2012). Amygdala Volume Changes in Posttraumatic Stress Disorder in a Large Case-Controlled Veterans Group. *Archives of General Psychiatry*, *69*(11), 1169-1178. https://doi.org/10.1001/archgenpsychiatry.2012.50

Mosconi, M. W., Cody-Hazlett, H., Poe, M. D., Gerig, G., Gimpel-Smith, R., & Piven, J. (2009). Longitudinal Study of Amygdala Volume and Joint Attention in 2- to 4-Year-Old Children With Autism. *Archives of General Psychiatry*, *66*(5), 509-516. https://doi.org/10.1001/archgenpsychiatry.2009.19

Nacewicz, B. M., Dalton, K. M., Johnstone, T., Long, M. T., McAuliff, E. M., Oakes, T. R., Alexander, A. L., & Davidson, R. J. (2006). Amygdala Volume and Nonverbal Social Impairment in Adolescent and Adult Males With Autism. *Archives of General Psychiatry*, *63*(12), 1417-1428. https://doi.org/10.1001/archpsyc.63.12.1417

Nishikimi, M., Oishi, K., Tabata, H., Torii, K., & Nakajima, K. (2011). Segregation and Pathfinding of Callosal Axons through EphA3 Signaling. *The Journal of Neuroscience*, *31*(45), 16251. https://doi.org/10.1523/JNEUROSCI.3303-11.2011

Ousdal, O. T., Milde, A. M., Hafstad, G. S., Hodneland, E., Dyb, G., Craven, A. R., Melinder, A., Endestad, T., & Hugdahl, K. (2020). The association of PTSD symptom severity with amygdala nuclei volumes in traumatized youths. *Translational Psychiatry*, *10*(1), 288. https://doi.org/10.1038/s41398-020-00974-4

Paul, L. K., Corsello, C., Kennedy, D. P., & Adolphs, R. (2014). Agenesis of the corpus callosum and autism: a comprehensive comparison. *Brain*, *137*(6), 1813-1829. https://doi.org/10.1093/brain/awu070

Pedregosa, F., Varoquaux, G., Gramfort, A., Michel, V., Thirion, B., Grisel, O., Blondel, M., Prettenhofer, P., Weiss, R., & Dubourg, V. (2011). Scikit-learn: Machine learning in Python. *the Journal of machine Learning research*, *12*, 2825-2830.

Pérez-Ramírez, Ú., López-Madrona, V. J., Pérez-Segura, A., Pallarés, V., Moreno, A., Ciccocioppo, R., Hyytiä, P., Sommer, W. H., Moratal, D., & Canals, S. (2022). Brain Network Allostasis after Chronic Alcohol Drinking Is Characterized by Functional Dedifferentiation and Narrowing. *The Journal of Neuroscience*, *42*(21), 4401. https://doi.org/10.1523/JNEUROSCI.0389-21.2022

Prigge, M. B. D., Lange, N., Bigler, E. D., Merkley, T. L., Neeley, E. S., Abildskov, T. J., Froehlich, A. L., Nielsen, J. A., Cooperrider, J. R., Cariello, A. N., Ravichandran, C., Alexander, A. L., & Lainhart, J. E. (2013). Corpus callosum area in children and adults with autism. *Research in Autism Spectrum Disorders*, *7*(2), 221-234. https://doi.org/https://doi.org/10.1016/j.rasd.2012.09.007

Purcell, S., Neale, B., Todd-Brown, K., Thomas, L., Ferreira, M. A. R., Bender, D., Maller, J., Sklar, P., de Bakker, P. I. W., Daly, M. J., & Sham, P. C. (2007). PLINK: A Tool Set for Whole-Genome Association and Population-Based Linkage Analyses. *The American Journal of Human Genetics*, *81*(3), 559-575. https://doi.org/10.1086/519795

Raise-Abdullahi, P., Meamar, M., Abbas Ali, V., Alizadeh, M., Dadkhah, M., Shafia, S., Ghalandari-Shamami, M., Naderian, R., Seyed Afshin, S., & Rashidy-Pour, A. (2023). Hypothalamus and Post-Traumatic Stress Disorder: A Review. *Brain Sciences*, *13*(7), 1010. https://doi.org/https://doi.org/10.3390/brainsci13071010

Roddy, D., Kelly, J. R., Farrell, C., Doolin, K., Roman, E., Nasa, A., Frodl, T., Harkin, A., O'Mara, S., O'Hanlon, E., & O'Keane, V. (2021). Amygdala substructure volumes in Major Depressive Disorder. *NeuroImage: Clinical*, *31*, 102781. https://doi.org/https://doi.org/10.1016/j.nicl.2021.102781

Roddy, D. W., Farrell, C., Doolin, K., Roman, E., Tozzi, L., Frodl, T., O'Keane, V., & O'Hanlon, E. (2019). The Hippocampus in Depression: More Than the Sum of Its Parts? Advanced Hippocampal Substructure Segmentation in Depression. *Biological Psychiatry*, *85*(6), 487-497. https://doi.org/https://doi.org/10.1016/j.biopsych.2018.08.021

Roeckner, A. R., Oliver, K. I., Lebois, L. A. M., van Rooij, S. J. H., & Stevens, J. S. (2021). Neural contributors to trauma resilience: a review of longitudinal neuroimaging studies. *Translational Psychiatry*, *11*(1), 508. https://doi.org/10.1038/s41398-021-01633-y

Rusch, B. D., Abercrombie, H. C., Oakes, T. R., Schaefer, S. M., & Davidson, R. J. (2001). Hippocampal morphometry in depressed patients and control subjects: relations to anxiety symptoms. *Biological Psychiatry*, *50*(12), 960-964. https://doi.org/https://doi.org/10.1016/S0006-3223(01)01248-3

Sacchet, M. D., Camacho, M. C., Livermore, E. E., Thomas, E. A. C., & Gotlib, I. H. (2016). Accelerated aging of the putamen in patients with major depressive disorder. *Journal of Psychiatry and Neuroscience*, *42*(3), 164-171. https://doi.org/10.1503/jpn.160010

Schoeler, T., Pingault, J.-B., & Kutalik, Z. (2025). Combining cross-sectional and longitudinal genomic approaches to identify determinants of cognitive and physical decline. *Nature Communications*, *16*(1), 4524. https://doi.org/10.1038/s41467-025-59383-0

Schulz, M.-A., Yeo, B. T. T., Vogelstein, J. T., Mourao-Miranada, J., Kather, J. N., Kording, K., Richards, B., & Bzdok, D. (2020). Different scaling of linear models and deep learning in UKBiobank brain images versus machine-learning datasets. *Nature Communications*, *11*(1), 4238. https://doi.org/10.1038/s41467-020-18037-z

Schumann, C. M., Hamstra, J., Goodlin-Jones, B. L., Lotspeich, L. J., Kwon, H., Buonocore, M. H., Lammers, C. R., Reiss, A. L., & Amaral, D. G. (2004). The Amygdala Is Enlarged in Children But Not Adolescents with Autism; the Hippocampus Is Enlarged at All Ages. *The Journal of Neuroscience*, *24*(28), 6392. https://doi.org/10.1523/JNEUROSCI.1297-04.2004

Siehl, S., King, J. A., Burgess, N., Flor, H., & Nees, F. (2018). Structural white matter changes in adults and children with posttraumatic stress disorder: A systematic review and meta-analysis. *NeuroImage: Clinical*, *19*, 581-598. https://doi.org/https://doi.org/10.1016/j.nicl.2018.05.013

Smith, S. M., Douaud, G., Chen, W., Hanayik, T., Alfaro-Almagro, F., Sharp, K., & Elliott, L. T. (2021). An expanded set of genome-wide association studies of brain imaging phenotypes in UK Biobank. *Nature Neuroscience*, *24*(5), 737-745. https://doi.org/10.1038/s41593-021-00826-4

Sparks, B. F., Friedman, S. D., Shaw, D. W., Aylward, E. H., Echelard, D., Artru, A. A., Maravilla, K. R., Giedd, J. N., Munson, J., Dawson, G., & Dager, S. R. (2002). Brain structural abnormalities in young children with autism spectrum disorder. *Neurology*, *59*(2), 184-192. https://doi.org/10.1212/WNL.59.2.184

Sreenivas, S., Boehm, S. G., & Linden, D. E. J. (2012). Emotional faces and the default mode network. *Neuroscience Letters*, *506*(2), 229-234. https://doi.org/https://doi.org/10.1016/j.neulet.2011.11.012

Sugama, S., Sekiyama, K., Kodama, T., Takamatsu, Y., Takenouchi, T., Hashimoto, M., Bruno, C., & Kakinuma, Y. (2016). Chronic restraint stress triggers dopaminergic and noradrenergic neurodegeneration: Possible role of chronic stress in the onset of Parkinson's disease. *Brain, Behavior, and Immunity*, *51*, 39-46. https://doi.org/https://doi.org/10.1016/j.bbi.2015.08.015

Tamm, S., Harmer, C. J., Schiel, J., Holub, F., Rutter, M. K., Spiegelhalder, K., & Kyle, S. D. (2022). No Association Between Amygdala Responses to Negative Faces and Depressive Symptoms: Cross-Sectional Data from 28,638 Individuals in the UK Biobank Cohort. *American Journal of Psychiatry*, *179*(7), 509-513. https://doi.org/10.1176/appi.ajp.21050466

Thome, I., García Alanis, J. C., Volk, J., Vogelbacher, C., Steinsträter, O., & Jansen, A. (2022). Let's face it: The lateralization of the face perception network as measured with fMRI is not clearly right dominant. *Neuroimage*, *263*, 119587. https://doi.org/https://doi.org/10.1016/j.neuroimage.2022.119587

Villarreal, G., Hamilton, D. A., Petropoulos, H., Driscoll, I., Rowland, L. M., Griego, J. A., Kodituwakku, P. W., Hart, B. L., Escalona, R., & Brooks, W. M. (2002). Reduced hippocampal volume and total white matter volume in posttraumatic stress disorder. *Biological Psychiatry*, *52*(2), 119-125. https://doi.org/https://doi.org/10.1016/S0006-3223(02)01359-8

Warrington, S., Bryant, K. L., Khrapitchev, A. A., Sallet, J., Charquero-Ballester, M., Douaud, G., Jbabdi, S., Mars, R. B., & Sotiropoulos, S. N. (2020). XTRACT - Standardised protocols for automated tractography in the human and macaque brain. *Neuroimage*, *217*, 116923. https://doi.org/https://doi.org/10.1016/j.neuroimage.2020.116923

World Health Organization (2022). *International Classification of Diseases Eleventh Revision (ICD-11)*. World Health Organization. https://icd.who.int/browse11/l-m/en

https://icdcdn.who.int/icd11referenceguide/en/refguide.pdf

Wise, T., Radua, J., Via, E., Cardoner, N., Abe, O., Adams, T. M., Amico, F., Cheng, Y., Cole, J. H., de Azevedo Marques Périco, C., Dickstein, D. P., Farrow, T. F. D., Frodl, T., Wagner, G., Gotlib, I. H., Gruber, O., Ham, B. J., Job, D. E., Kempton, M. J., . . . Arnone, D. (2017). Common and distinct patterns of grey-matter volume alteration in major depression and bipolar disorder: evidence from voxel-based meta-analysis. *Molecular Psychiatry*, *22*(10), 1455-1463. https://doi.org/10.1038/mp.2016.72

Yang, L.-Z., Shi, B., Li, H., Zhang, W., Liu, Y., Wang, H., Zhou, Y., Wang, Y., Lv, W., Ji, X., Hudak, J., Zhou, Y., Fallgatter, A. J., & Zhang, X. (2017). Electrical stimulation reduces smokers' craving by modulating the coupling between dorsal lateral prefrontal cortex and parahippocampal gyrus. *Social Cognitive and Affective Neuroscience*, *12*(8), 1296-1302. https://doi.org/10.1093/scan/nsx055

Zhang, X., Grove, J., Gu, Y., Buus, C. K., Nielsen, L. K., Neufeld, S. A. S., Koko, M., Malawsky, D. S., Wade, E. M., Verhoef, E., Gui, A., Hegemann, L., Allison, C., Tsompanidis, A., Adhya, D., Holt, R., Al-Rubaie, O., Ghoddousi, R. A. M., Heazell, A. E. P., . . . Consortium, P.-P. (2025). Polygenic and developmental profiles of autism differ by age at diagnosis. *Nature*. https://doi.org/10.1038/s41586-025-09542-6

Zhang, Y., Larcher, K. M.-H., Misic, B., & Dagher, A. (2017). Anatomical and functional organization of the human substantia nigra and its connections. *Elife*, *6*, e26653. https://doi.org/10.7554/eLife.26653

Zhao, M., Yu, Z., Zhang, Y., Huang, X., Hou, J., Zhao, Y., Luo, W., Chen, L., Ou, L., Li, H., & Zhang, J. (2016). Iron-induced neuronal damage in a rat model of post-traumatic stress disorder. *Neuroscience*, *330*, 90-99. https://doi.org/https://doi.org/10.1016/j.neuroscience.2016.05.025

Zhou, X., & Zhang, L. (2021). The Neuroprotective Effects of Moderate and Regular Caffeine Consumption in Alzheimer's Disease. *Oxidative Medicine and Cellular Longevity*, *2021*(1), 5568011. https://doi.org/https://doi.org/10.1155/2021/5568011

Zilcha-Mano, S., Zhu, X., Lazarov, A., Suarez-Jimenez, B., Helpman, L., Kim, Y., Maitlin, C., Neria, Y., & Rutherford, B. R. (2022). Structural brain features signaling trauma, PTSD, or resilience? A systematic exploration. *Depression and Anxiety*, *39*(10-11), 695-705. https://doi.org/https://doi.org/10.1002/da.23275